

DISSERTATION

RELATIONSHIPS BETWEEN AEROSOL, CLOUD, AND PRECIPITATION AS OBSERVED FROM THE A-TRAIN CONSTELLATION OF SPACEBORNE SENSORS

Submitted by

Matthew David Lebsock

Department of Atmospheric Science

In partial fulfillment of the requirements

for the degree of Doctor of Philosophy

Colorado State University

Fort Collins, Colorado

Spring 2009

COLORADO STATE UNIVERSITY

June 04, 2009

WE HEREBY RECOMMEND THAT THE DISSERTATION PREPARED UNDER OUR SUPERVISION BY MATTHEW DAVID LEBSOCK ENTITLED RELATIONSHIPS BETWEEN AEROSOL, CLOUD, AND PRECIPITATION AS OBSERVED FROM THE A-TRAIN CONSTELLATION OF SPACEBORNE SENSORS BE ACCEPTED AS FULFILLING IN PART REQUIREMENTS FOR THE DEGREE OF DOCTOR OF PHILOSOPHY

Committee on Graduate Work

Christian Kummerow (Co-Advisor)

Graeme Stephens (Co-Advisor)

David Randall (Committee Member)

Steven Reising (Committee Member)

Richard Johnson (Department Head)

ABSTRACT OF DISSERTATION

RELATIONSHIPS BETWEEN AEROSOL, CLOUD, AND PRECIPITATION AS OBSERVED FROM THE A-TRAIN CONSTELLATION OF SPACEBORNE SENSORS

Data from several sensors flying in NASA's A-train constellation of satellites are analyzed to examine global relationships between aerosol, clouds and precipitation with particular emphasis placed on the Earth's radiation budget. The multi-sensor data are applied to two specific studies. The first addresses the response of cloud water path to atmospheric aerosol burden and the second quantifies relationships between tropical precipitation and radiation within the context of radiative-convective equilibrium.

The first focused study presents a global multi-sensor satellite examination of aerosol indirect effects on warm oceanic clouds. The study centers on the water path response of cloud to aerosol burden. It is demonstrated that high aerosol environments are associated with reduced liquid water path in nonprecipitating clouds and that the reduction in liquid water path reduces the albedo enhancement expected from decreasing effective radius. Furthermore the reduction in liquid water path is greater in thermodynamically unstable environments than in stable environments, suggesting a greater sensitivity of liquid water path to aerosol in cumulus clouds than stratus clouds. In sharp contrast with nonprecipitating clouds, the cloud liquid water path of transitional and precipitating clouds increases dramatically with aerosol, which may be indicative of an inhibited coalescence process. Following from these observations, the magnitude of the aerosol indirect albedo sensitivity (IAS) is calculated as the sum of distinct cloud regimes over the global oceans. Selection of the cloud regimes is guided by the observation that both thermodynamic stability and the presence of precipitation affect the sensitivity of cloud albedo to aerosol concentrations. The IAS,

defined as the change in warm cloud albedo for a fractional change in aerosol burden, is found to be $-0.42 \pm 0.38 \text{ Wm}^{-2}$ over the global oceans. Twenty five percent of the effect is due to precipitating clouds despite the fact that only eight percent of clouds are identified as precipitating. An additional assumption of the anthropogenic aerosol fraction provides an estimate of the indirect albedo forcing (IAF) of $-0.13 \pm 0.14 \text{ Wm}^{-2}$, which is significantly lower than the range provided by climate model estimates.

The second focused study presents an analysis of anomalous precipitation, cloud, thermodynamic, and radiation variables on the tropics-wide mean spatial scale. In particular, relationships between the mean tropical oceanic precipitation anomaly and radiative anomalies are examined. It is found that tropical mean precipitation is well correlated with cloud properties and radiative fields. In particular, the tropical mean precipitation anomaly is positively correlated with the top of the atmosphere reflected shortwave anomaly and negatively correlated with the emitted longwave anomaly. The tropical mean relationships are found to primarily result from a coherent oscillation of precipitation and the area of high-level cloudiness. The correlations manifest themselves radiatively as a modest cooling at the top of the atmosphere and a redistribution of energy from the surface to the atmosphere through reduced solar radiation to the surface and decreased longwave emission to space. The anomalous atmospheric column radiative heating is found to be about 10% of the magnitude of the anomalous latent heating. The temporal signature of the radiative heating is observed in the column mean temperature that indicates a coherent phase-lagged oscillation between atmospheric stability and convection. These relationships are identified as a radiative-convective cloud feedback that is observed on intra-seasonal timescales associated with the Madden-Julian oscillation in the tropical atmosphere. A composite analysis showing the spatial patterns of the anomalies provides evidence that the feedback mechanism works through a modulation of the strength of the large-scale

tropical overturning circulations.

Matthew David Lebsock
Department of Atmospheric Science
Colorado State University
Fort Collins, CO 80523
Summer 2009

Contents

1	Introduction	1
2	Multi-Sensor Satellite Observations of Aerosol Effects on Warm Clouds	5
2.1	Introduction	6
2.2	Data	10
2.3	Results	13
2.3.1	Non-Precipitating Clouds	13
2.3.2	Precipitating Clouds	21
2.4	Conclusions	26
3	Estimating the Global Oceanic Aerosol Indirect Albedo Sensitivity	29
3.1	Introduction	30
3.2	Data and Methodology	33
3.2.1	Data	33
3.2.2	Calculating the indirect albedo sensitivity	33
3.2.3	Calculating the cloud parameter sensitivities	37
3.3	Results	41
3.3.1	Cloud parameter sensitivities	41
3.3.2	Magnitude of the indirect albedo sensitivity	44
3.4	Summary	45

4	An Observed Tropical Oceanic Radiative-Convective Cloud Feed-	
	back	51
4.1	Introduction	52
4.2	Data	55
4.3	Methodology	56
4.3.1	Cluster analysis	56
4.3.2	Constructing the tropical mean anomaly time series:	58
4.4	Results and Discussion	60
4.4.1	Radiation budget	60
4.4.2	Relationship of tropical mean radiation budget to precipitation	63
4.4.3	Time dependent behavior (A demonstration of the feedback) .	67
4.4.4	Relationship to the Madden-Julian oscillation	73
4.4.5	Spatial patterns of the anomalies	74
4.4.6	Extension of the feedback to a perturbed climate	77
4.4.7	Model comparison	79
4.5	Summary	82
5	Summary of Dissertation	85
5.1	Aerosol indirect effects	85
5.2	Tropical precipitation and radiation	88

List of Tables

2.1	Observations used in the analysis along with their source and spatial resolution.	11
2.2	Slope of linear fit between various non-precipitating cloud parameters and $\log_{10}(\text{AI})$	14
2.3	Slope of linear fits between cloud parameters and $\log_{10}(\text{AI})$. Comparison of non-precipitating, transitional and precipitating clouds.	24
4.1	The daily mean tropical oceanic energy budget [Wm^{-2}] for the various cloud clusters. The top of the atmosphere (TOA) is defined positive up, the surface (SFC) is defined positive down, and the atmospheric column (ATM) is defined positive in. F_o is the incoming solar flux. Latent heating (LH) is derived from the AMSR-E precipitation rates.	61
4.2	The daily mean top of the atmosphere (TOA) radiative sensitivity to precipitation. Also shown is the sensitivity of cloud fraction (CF), cloud optical depth (τ_{cloud}), and cloud top temperature (CTT). The sensitivity is defined as the linear fit between the radiative anomaly with the precipitation anomaly. The anomaly time series have been created by removing the seasonal cycle, removing the linear effects of the El Niño Southern Oscillation (ENSO), and high pass filtering the data. Trends that are insignificant at the 99% level are italicized.	64

4.3 Trends of the tropical average radiation anomalies with the tropical average precipitation rate $[(\text{Wm}^{-2})/(\text{mmd}^{-1})]$ from the CERES/AMSR-E observations and several selected climate models from the climate of the twentieth century model runs. Note that the TOA shortwave radiation parameters are not archived on the daily timescale for these model runs. 80

List of Figures

2.1	Global relationships between AI and non-precipitating cloud parameters. Circles represent the mean values and error bars show the standard deviation.	15
2.2	Global relationships between LTSS and the MODIS cloud fraction and the MODIS channel 1 (0.645 μm) reflectance variability. Cloud fraction is from a 3x3 pixel estimate taken from the CloudSat GEOPROF product. The standard deviation of the reflectance is calculated from an 11x11 pixel subset of the MODIS data surrounding the CloudSat footprint.	17
2.3	Cloud albedo derived from the two stream approximation. Circles(triangles) represent the mean r_e and LWP for a clean(dirty) state. The delineation between clean and dirty is given by AI = 0.1.	18
2.4	Comparison of the CERES TOA albedo with the cloud top albedo derived from the MODIS cloud products using a two stream radiative transfer model.	19
2.5	Trends of the (A) CERES cloudy sky albedo and (B) MODIS r_e with the AMSR-E LWP. The delineation between clean and dirty is given by AI = 0.1. The stable curve represents all LTSS between 18 and 21 K. The unstable curve represents all LTSS between 12 and 15 K. . . .	21

2.6	Global relationships between AI and non-precipitating, transitional, and precipitating cloud parameters. Circles represent the mean values and Error bars show the standard deviation. The LWP estimate is for the cloud component only from AMSR-E. The reflectivity is the CPR vertical cloud mean reflectivity factor.	23
2.7	The global conditional probability of warm cloud precipitation as a function of AI for various column water vapor regimes. The units for CWV are kg/m ²	26
2.8	Trends of the conditional probability of warm cloud precipitation with LWP. The delineation between clean and dirty is given by AI = 0.1. The stable regime represents all LTSS between 18 and 21 K. The unstable regime represents all LTSS between 12 and 15 K.	27
3.1	The annual mean spatial distributions of the three stability regimes .	35
3.2	The annual mean spatial distribution of the probability of precipitation of warm clouds	36
3.3	Probability distribution function (PDF) of the global distribution of the ECMWF derived lower tropospheric static stability (LTSS). . . .	37
3.4	The annual average and the seasonal mean distribution of the top of the atmosphere solar insolation as a function of latitude.	38
3.5	The seasonal mean spatial distribution of the warm cloud fraction as observed by MODIS	39
3.6	The CERES cloudy sky albedo as a function of the aerosol index for each of the six cloud regimes. Error bars show the standard deviation of the albedo within each AI bin.	40
3.7	Probability distribution function (PDF) of the global distribution of the MODIS derived aerosol index (AI).	41

3.8	The sensitivities of the cloud parameters for each of the six cloud regimes. (A) shows the non-precipitating cloud sensitivities and (B) shows the Precipitating clouds. The σ values are the associated uncertainties that are described in Section 3.2.3	42
3.9	Regional distribution of the IAS as described in Section 3.2.2. Results are divided into precipitating and non-precipitating clouds.	48
3.10	The global IAS as described in Section 3.2.2. Results are divided into precipitating and non-precipitating clouds. The cloud component is additionally broken down into the three stability regimes.	49
4.1	The six tropical oceanic cloud clusters. The cloud fraction (CF) and the relative frequency of occurrence (RFO) are provided in percent.	58
4.2	Mean geographical distribution of the frequency of occurrence of each of the six tropical oceanic cloud clusters. Note that the color scale differs for the mostly clear regime.	59
4.3	An example of the filtering process for the specific case of the tropical oceanic column mean temperature (T_{ATM}). The filtering process is described in the text.	60
4.4	Relationships between tropical ocean mean precipitation (P') and radiative (F') anomalies. Results are broken down into shortwave (SW) and longwave (LW) components. The summary statistic (s) is the slope of the linear fit while (r) is the correlation coefficient.	65
4.5	Graphical depiction of the radiative-convective cloud feedback. Perturbations to the atmospheric column radiative heating rate are approximately balanced by perturbations of the atmospheric latent heat release through precipitation. The precipitation perturbation is associated with cloudiness perturbations that act to counter the atmospheric cooling rate perturbation thus establishing the negative feedback loop.	66

4.6	Lag-sensitivities of the tropical oceanic mean shortwave (SW) and long-wave (LW) top of the atmosphere (TOA) radiative anomalies with the precipitation anomalies (gray lines). Also shown for reference is the auto-correlation of the precipitation anomaly time series (black lines). The dotted lines represent the thresholds for statistically significant autocorrelations at the 95% level. A seven-day running mean has been applied to the anomaly time series.	68
4.7	As in Figure 4.6 but for lag-sensitivities of the tropical oceanic mean net top of the atmosphere (TOA) atmospheric column (ATM) and surface (SFC) radiative anomalies with the precipitation anomalies (gray lines).	69
4.8	As in Figure 4.6 but for lag-sensitivities of the anomalous cluster frequency of occurrence with the precipitation anomalies (gray lines). . .	70
4.9	As in Figure 4.6 but for lag-sensitivities of the cloud fraction (CF), cloud optical depth (τ_{cloud}), and cloud top temperature (CTT) anomalies (gray lines).	71
4.10	As in Figure 4.7 but for lag-sensitivities of the tropical oceanic mean net atmospheric column mean heating rate with the precipitation anomalies (gray lines). The solid/dashed gray lines represent the microwave/infrared AIRS algorithms.	71
4.11	As in Figure 4.7 but for lag-sensitivities of the tropical oceanic mean net temperature anomaly with the precipitation anomalies (gray lines). The solid/dashed gray lines represent the microwave/infrared AIRS algorithms. Low is defined as the surface to 650 hPa, middle is defined as 650 hPa to 350 hPa, and high is defined as higher than 350 hPa. . .	72

4.12 The power spectra (Φ) of (A) Precipitation (B) TOA shortwave (C) TOA longwave (D) RMM1 and (E) RMM2. Φ is plotted as a function of frequency (ω) in cycles per day (CPD). The area under the curve has been normalized to unity. A 21 point tapered running mean has been applied to all spectra to increase the number of degrees of freedom for significance testing. The solid gray line is the red-noise spectrum computed from the e-folding auto-correlation timescale of each time series while the dashed gray line represents the level of spectral power that is needed to reach the 95% confidence level for significance. The vertical dashed lines show periods from 10-60 days. 75

4.13 The Co-Spectra of RMM1 (A-C) and RMM2 (D-F) with the anomalous precipitation (P) TOA shortwave ($F_{SW,TOA}$), and TOA longwave ($F_{LW,TOA}$). As in Figure 4.12, a 21 point tapered running mean has been applied to the spectra. Coherence squared (Coh^2) values that exceed the threshold drawn by the horizontal dashed (0.283) line exceed the 95% confidence level for significance. The vertical dashed lines show periods from 10-60 days. Note that only frequencies bands in which both the power spectra (Φ) (shown in Figure 4.12) and the Coh^2 are statistically significant should be considered significant. This occurs for all parameters near 30 and 50 day periods. 76

4.14 Geographical distribution of the precipitation, radiation, and cloud parameters for the positive rainfall composite days (defined as days when anomalous rainfall exceeds one standard deviation of the mean). The spatial correlation coefficient (r) of each composite map with the precipitation composite is provided. 77

4.15	The multi-model mean precipitation sensitivity of the IPCC AR4 models for the 1% to 2xCO ₂ runs. This sensitivity is defined as the percentage change in precipitation rate for a 1 Kelvin change in global mean surface temperature. The mean over the tropical (30S-30N) oceans is 1.94 %/K.	78
4.16	Comparison of the IPCC 20C3M daily model output with the observed relationships. Note that the TOA shortwave output is not available from the models on the daily time scale.	81

Chapter 1

Introduction

Radiation is the sole source of energy to the Earth's climate system and radiative transfer is a primary physical mechanism through which energy is distributed throughout the Earth-atmosphere system. Moreover, the distribution of radiant energy within the atmosphere explains to a large extent the patterns of the atmospheric circulation and thus the Earth's weather and climate. Substantial scientific focus has been dedicated toward understanding the Earth's radiation budget (ERB) at the top of the atmosphere (TOA). For example, pioneering observations of the ERB were made by *Vonder Haar and Suomi* [1969] and have been incrementally improved since then [*Ramanathan et al.*, 1989; *Harrison et al.*, 1990]. Focus on the TOA radiation field has identified regions of net heating and cooling of the Earth-Atmosphere system [*Vonder Haar and Suomi*, 1971] as well as deduced the latitudinal transport of energy within the system [*Carissimo et al.*, 1985]. Only recently have comprehensive estimates of the atmospheric and surface radiative budget become widely available. Examples of global-scale satellite based estimates of the surface and atmospheric distribution of radiative fluxes are data from the CERES (Clouds and Earth's Radiant Energy System) instrument [*Wielicki et al.*, 1996], the HERB (Hydrology and Earth's Radiation Budget) algorithm [*L'Ecuyer and Stephens*, 2003], and the ISCPP (International Satellite Cloud Climatology Project) dataset [*Zhang et al.*, 1995; *Rossow and Zhang*, 1995]. A synthesis of satellite data and model output has permitted descrip-

tions of the global energy balance including radiative, latent, and sensible heat fluxes [Kiehl and Trenberth, 1997; Trenberth and Fasullo, 2009]. While substantial error remains in the surface and atmospheric terms of these budgets, the gross magnitudes of the fluxes are now known. Nevertheless, the range of uncertainty in the ERB is roughly an order of magnitude larger than that of the expected value of anthropogenic forcing to the ERB, thus motivating a significant effort toward refinement of these values.

In the context of anthropogenic climate change, quantifying forcings to the Earth's radiation budget represents a key challenge. A critical component of the Intergovernmental Panel on Climate Change (IPCC) report regards the anthropogenic forcing of the radiation budget at the top of the atmosphere. In this context, a radiative forcing is defined as the transient perturbation to the tropopause radiation budget due to a particular change to the geophysical system. Certain elements of this forcing (for example the component due to anthropogenic CO₂ and other long-lived greenhouse gas emissions) are well understood and quantified. Other aspects of the anthropogenic radiative forcing remain less well understood. In particular, the largest single source of uncertainty in the radiative forcing is the magnitude of the indirect effects of anthropogenic aerosols on cloud properties and thus Earth's albedo. These are commonly referred to as aerosol indirect effects, and according to the IPCC Fourth Assessment Report (FAR), may range from -0.22 to -1.85 Wm⁻² [Forester *et al.*, 2007] for the first indirect effect, which is the modification of cloud albedo by anthropogenic aerosol at a fixed cloud water path [Twomey, 1977]. This range is large relative to the estimated total present day radiative forcing of approximately 1.6 Wm⁻² offered in the FAR [Forester *et al.*, 2007].

An additional critical uncertainty in climate change scenarios related to the Earth's radiation budget is that of cloud radiative feedbacks. A feedback process represents a change in the TOA ERB due to a change in a geophysical parameter that itself re-

sulted from a forcing acting on the ERB. Quantification of cloud feedbacks has proved elusive for many years [*Schneider, 1972; Cess et al., 1990; Stephens et al., 2005; Bony et al., 2006*]. Estimates of cloud feedbacks from the climate models included in the FAR range from 0 to 1.25 Wm^{-2} , and the standard deviation of the model feedbacks is 0.37 Wm^{-2} , which is roughly four times larger than either the humidity-lapse rate or albedo feedbacks [*Soden and Held, 2006*]. Uncertainty in these feedback estimates derives from the various cloud parameterizations employed in the different models [*Wyant, 2006*]. Furthermore, observation of cloud feedbacks is made difficult because by definition they are defined as partial derivatives that are not readily computed from available observations. Resolving the magnitude of cloud feedbacks is critical because it is commonly assumed that they account in large part for the uncertainty in the global climate sensitivity parameter (defined as the ratio of radiative forcing to global mean surface temperature). While observation of feedback processes may be difficult, observations of relationships within the global water and energy cycle in the current climate system represent a key component of advancing understanding of feedback process as argued by *Stephens [2005]* and *Bony et al. [2006]*. In particular, assuming that the perturbation response of the system is linear, it follows that identification of short time-scale feedbacks in the present climate may be applicable to a perturbed climate as well.

NASA's A-train constellation of sensors provides a suite of state of the art spaceborne sensors that offer unique opportunities for multi-sensor analysis of the aforementioned climatically relevant and highly uncertain processes. The A-train consists of five satellites (Aqua, CloudSat, Calipso, Parasol, and Aura) flying in a sun-synchronous polar orbiting formation with a 1:30 p.m. equator crossing time. A myriad assortment of radiometric sensors fly aboard these satellites to probe the Earth's atmosphere and surface. The synthesis of the vast quantities of data collected by these sensors is an immense task of significant importance. To this end,

in this work a multi-sensor approach is taken to atmospheric observation by combining measurements from MODIS (Moderate Resolution Imaging Spectroradiometer), AMSR-E (Advanced Microwave Scanning Radiometer), CERES (Clouds and Earth's Radiant Energy System), AIRS (Atmospheric Infrared Sounder), and the CloudSat CPR (Cloud Profiling Radar). Together, this unique suite of instruments provides a comprehensive view of the the radiative, thermodynamic and hydrological structure of the atmosphere. This observation set offers a unique view of both aerosol-cloud-precipitation interactions as well as cloud feedbacks in the climate system. Importantly, the inclusion of CERES observations provides a direct link between this dataset and the ERB.

This dissertation contributes to the two aspects of critical uncertainty concerning climate change scenarios outlined above. Chapter 2 identifies global relationships between aerosol, cloud and precipitation parameters in shallow clouds. In particular, this section of the dissertation focuses on the poorly understood relationships between ambient aerosol concentration and the liquid water path of clouds while simultaneously controlling for atmospheric thermodynamics and the presence of precipitation. Chapter 3 extends the results of Chapter 2 in outlining a novel method to compute the aerosol indirect albedo forcing as a weighted combination of various cloud regimes. The dissertation switches gears in Chapter 4, focusing on radiative-convective cloud feedbacks in the tropical atmosphere. This aspect of the dissertation is presented in the context of the current climate, however its application to possible future climate scenarios is discussed as well. Finally, Chapter 5 provides a brief overview of the key findings of the dissertation.

Chapter 2

Multi-Sensor Satellite Observations of Aerosol Effects on Warm Clouds

Abstract

A global multisensor satellite examination of aerosol indirect effects on warm oceanic clouds is presented. The study centers on the water path response of cloud to aerosol burden. A unique element of the study is a rigorous rain screening methodology that is utilized to separate the responses of nonraining and raining clouds. It is demonstrated that high aerosol environments are associated with reduced liquid water path in nonprecipitating clouds and that the reduction in liquid water path reduces the albedo enhancement expected from decreasing effective radius. Furthermore the reduction in liquid water path is greater in thermodynamically unstable environments than in stable environments suggesting a greater sensitivity of liquid water path to aerosol in cumulus clouds than in stratiform clouds. In sharp contrast with nonprecipitating clouds, the cloud liquid water path of transitional and precipitating clouds increases dramatically with aerosol, which may be indicative of an inhibited coalescence process. The evidence further indicates that increasing aerosol requires greater amounts of cloud condensate before the onset of precipitation. Additional

support for this hypothesis is found in a reduction of the probability of precipitation by as much as 10% depending on the thermodynamical state of the environment. Independent estimates of the broadband cloudy-sky albedo are used to confirm that the cloud albedo responds to the trends that are identified in the liquid water path. In particular, it is found that the water path effect dominates the cloud albedo response for precipitating and transitional clouds.

2.1 Introduction

It has been proposed that anthropogenic aerosols may indirectly affect the Earth's radiation budget through their action as cloud condensation nuclei (CCN). The theories follow from the observation that cloud droplet number concentrations are related to aerosol number concentrations, therein providing a pathway through which aerosol may affect cloud microphysical properties. Two indirect effects have been identified. The first indirect effect proposed by *Twomey* [1977] may be understood through the relationship for the visible optical depth [*Stephens*, 1978] given by,

$$\tau = \frac{3\text{LWP}}{2\rho_l r_e}, \quad (2.1)$$

where τ is the cloud optical depth, LWP is the cloud liquid water path, ρ_l is the density of water and the effective radius is defined as,

$$r_e = \frac{\int r^3 n(r) dr}{\int r^2 n(r) dr}, \quad (2.2)$$

where $n(r)$ is the cloud droplet size distribution as a function of radius (r). The theory posits that for a constant liquid water path, an increase in CCN concentration will result in a decrease in the cloud droplet effective radius resulting in a corresponding increase in cloud optical depth. Furthermore, cloud albedo (α_{cl}) is primarily a

function of τ , which through Equation 2.1 is a function of r_e and LWP,

$$\alpha_{cl} \approx F(\tau) = F(r_e, \text{LWP}). \quad (2.3)$$

It follows that for a given LWP, increased CCN concentrations should be associated with brighter clouds, resulting in a negative radiative forcing that would oppose the positive forcing of anthropogenic greenhouse gasses. In addition to this first indirect effect, anthropogenic aerosol may affect the onset of precipitation [Albrecht, 1989] by modifying droplet size distributions and inhibiting the coalescence process. This, in turn, may extend cloud lifetime, enhance cloud water contents and increase cloud fraction thus providing an additional negative radiative forcing.

To date, global satellite surveys of the first indirect or Twomey effect have used data from visible and infrared imagers. This approach logically follows from the capability of these instruments to observe both aerosol properties in clear skies along with cloud microphysical properties. The relevant observables from these sensors include the cloud optical depth and effective radius along with an aerosol index (AI). The aerosol index is given by $\text{AI} = \tau_a \alpha_a$, where τ_a is the aerosol optical depth and α_a is the Angstrom exponent. Under some assumptions, AI is representative of the column CCN concentration [Nakajima *et al.*, 2001]. As an example of this approach, Nakajima *et al.* [2001] use the Advanced Very High Resolution Spectro-Radiometer (AVHRR) to demonstrate a negative correlation between the column CCN concentration and the effective radius and a positive correlation with τ over the ocean. Bréon *et al.* [2002] use the unique aerosol sensing capabilities of the POLarization and Directionality of the Earth's Reflectance (POLDER) instrument to expand on this analysis, demonstrating that negative r_e correlations exist over both land and ocean.

Because the chain of events relating aerosol to increased cloud lifetime involves

poorly understood microphysical and dynamical processes, it has been difficult to demonstrate causal relationships between aerosol and albedo resulting from precipitation suppression. On local scales, remote sensing [*Rosenfeld, 2000*] and in-situ observations [*Ferek et al., 2000*] indicate that enhanced aerosol concentrations can indeed suppress precipitation. The expected effects on cloud lifetime are more difficult to observe with current remote sensing observations, however it is commonly assumed that cloud fraction and cloud lifetime are related. Therefore, analysis of the second indirect effect tends to focus on modification of the cloud fraction by enhanced aerosol concentration. For example, *Sekiguchi et al.* [2003] show a correlation between AI and cloud fraction on the global scale, which is suggestive of widespread precipitation suppression. In contrast to this evidence, modeling studies [*Jiang et al., 2006*] suggest that CCN concentrations may not significantly affect cloud lifetime or the cloud fraction. In an attempt to understand the intermediary relationships involved in second indirect effects, *Matsui et al.* [2004] show a negative correlation between AI and a column integrated effective radius that is more indicative of precipitation than the cloud top r_e . They further show that this relationship is independent of the lower tropospheric static stability (LTSS).

Whereas the global scale direct microphysical response of clouds to increased aerosol burden appears to be well established, the liquid water path response of clouds is less well established. For example the *Sekiguchi et al.* [2003] study shows a positive correlation between the AVHRR water path and the column CCN on the global scale whereas *Matsui et al.* [2006] show a negative correlation. *Han et al.* [2002] identify that the correlation between these parameters may be positive or negative and varies regionally, while the results of *Kaufman et al.* [2005] suggest that the sign of the response may depend on aerosol type. Even within a given region or cloud type, evidence from both remote sensing [*Coakley and Walsh, 2000*] and in situ [*Ackerman et al., 2000*] analyses indicates that the liquid water response of individual clouds

may be either positive or negative. Furthermore, modeling studies [*Ackerman et al.*, 2004], [*Wang et al.*, 2003] frequently demonstrate decreases in cloud water path resulting from increased entrainment of sub-saturated air leading to increased droplet evaporation. On the other hand, the second indirect effect predicts increases in cloud water path with increased aerosol burden, and both observations [*Taylor et al.*, 2000] and modeling studies [*Xue and Feingold*, 2006] support this hypothesis as well. In short, two primary competing effects have been identified that govern the response of cloud liquid water path to aerosol. The first effect is that of enhanced entrainment rates and evaporation that acts to reduce liquid water path and the second is that of inhibition of coalescence rates that acts to suppress precipitation and enhance liquid water path.

Reviewing Equation 2.3, it is seen that cloud albedo is a function of both the effective radius and the liquid water path. It follows that quantification of aerosol indirect effects requires understanding the complicated dependence of LWP on aerosol burden. Whereas previous research has primarily focused on understanding the relationships between r_e (first indirect effect) and cloud fraction (second indirect effect) and aerosol, the focus of this work is on the liquid water path response of clouds to aerosol. To address the outstanding ambiguity in the water path response of clouds, aerosol indirect effects are examined in the context of the liquid water budget of clouds. For example, a concerted effort is made to distinguish between the responses of precipitating and non-precipitating clouds. This distinction allows for the identification of the very different LWP responses of these cloud types to aerosol. Additionally, the distinction between raining and non-raining clouds, along with the use of two independent estimates of LWP, permits a critical assessment of the constant liquid water path assumption for non-precipitating clouds, which is often invoked in examination of the first indirect effect. Furthermore, the water path response of non-precipitating clouds is analyzed in conjunction with a measure of the thermodynamic stability in

order to indicate the environmental conditions that modulate the susceptibility of these clouds to entrainment/evaporation effects. Throughout the work, an independent estimate of the cloud albedo is utilized to emphasize the importance of careful consideration of the liquid water budget of clouds to aerosol when analyzing indirect effects.

2.2 Data

Sixteen months of collocated observations from July 2006 through October 2007 from four sensors in NASA’s A-Train [*Stephens et al.*, 2002] constellation of satellites are utilized. Observations from the CloudSat cloud profiling radar (CPR) are collocated with those from collection 5 of the Moderate Resolution Imaging Spectroradiometer (MODIS) [*Platnick et al.*, 2003], the Advanced Microwave Scanning Radiometer (AMSR-E) [*Wentz and Spencer*, 1998] and pixel scale data from the Clouds and Earth’s Radiant Energy System (CERES) [*Wielicki et al.*, 1996] sensor. This combination of the various sensors provides a comprehensive view of the microphysical and radiative properties along with a unique view of the water budget of warm clouds. The data products used in the analysis along with the sensor from which they are derived and the spatial resolutions of each observation are outlined in Table 2.1. It must be noted that the analysis that follows does not account for the spatial resolution differences between the various sensors. The CPR provides a unique rain discrimination flag. The precipitation screening centers on the particular sensitivity of the CPR to precipitation-sized drops. This sensitivity is used in the implementation of a simple rain screen [*Haynes et al.*, 2009]. The MODIS instrument offers cloud liquid water path and microphysical information along with an estimate of the aerosol burden. The AMSR-E provides an independent estimate of liquid water path along with the column water vapor (CWV). The cloudy sky albedo is derived from

Table 2.1: Observations used in the analysis along with their source and spatial resolution.

Geophysical Parameter	Sensor	Spatial Resolution
Rain Flag	CloudSat	1.4x2.5 km
Cloud Reflectivity Factor	CloudSat	1.4x2.5 km
Lower Tropospheric Static Stability	CloudSat (ECMWF-AUX)	1.4x2.5 km
Aerosol Index	MODIS	1 ^o
10.8 μm Tb	MODIS	1 km
0.645 μm Reflectance	MODIS	1 km
Cloud Optical Depth	MODIS	1 km
Cloud Effective Radius	MODIS	1 km
Cloud Liquid Water Path	MODIS	1 km
Cloud Liquid Water Path	AMSR-E	13 km
Column Water Vapor	AMSR-E	21 km
Cloudy Sky Albedo	CERES	20 km

CERES observations of the shortwave reflected flux.

Particular care is taken to discriminate between raining and non-raining clouds. From the CloudSat rain flag product three cloud regimes are defined: non-precipitating, transitional, and precipitating. The transitional clouds may or may not have precipitation reaching the surface, however, with a path integrated attenuation greater than 2 dB and cloud base reflectivity greater than -15 dBZ they certainly contain drops large enough to precipitate [*Haynes and Stephens, 2007*]. Depending on their cloud lifetime they may be clouds that are on the way to the precipitation stage or are clouds that are in a dissipation stage. It should be noted that a significant fraction of low level liquid clouds is undetected by the CPR due to surface contamination of very shallow clouds or cloud reflectivity below the radar’s minimum detectable signal of -30 dBZ. CloudSat pixels in which the CPR does not identify cloud but MODIS does identify cloud are retained in the analysis as non-raining clouds. From this analysis, 82% of analyzed warm clouds are determined to be non-precipitating, 11.5% are defined as transitional, and 6.5% are certainly precipitating.

Several retrieval products are utilized to eliminate ice or mixed phase clouds from the analysis. First, the CPR echo top characterization in the level 2B-GEOPROF CloudSat product is used to screen out clouds with a cloud top higher than 500 hPa or a cloud top temperature less than 270 K based on the European Center for Medium range Weather Forecast-AUXiliary analysis (ECMWF-AUX). Additionally, the MODIS cloud flags in the MOD35 [Platnick *et al.*, 2003] product are used to screen out any pixels that may contain ice contamination. Finally the 10.8 micron MODIS brightness temperature (Tb) is used to eliminate pixels with Tb's less than 270 K. After this thorough screening 9,082,936 cloudy pixels remain for analysis.

The level 3 MODIS (collection 5) 0.55 μm aerosol optical depth and the 0.55 μm and 0.867 μm Angstrom exponent [Remer *et al.*, 2005] are used to derive the one-degree gridded aerosol index. The AI is adopted in this study as a measure of the column CCN. Using the large scale AI eliminates many of the problems of artificially high remotely sensed aerosol burdens near cloud boundaries. The mean AI is found to be 0.10 and the range from 0.01 to 1 that is adopted in this study is found to contain 96.7% of the data. While CCN concentrations may affect cloud microphysics, it is expected that cloud properties are primarily a function of the thermodynamic and dynamic environment in which the cloud exists. Therefore an effort must be made to control for these effects when exploring the effects of aerosol. Matsui *et al.* [2004] found that cloud properties varied in roughly equal magnitude with both the AI and the LTSS given by the potential difference between 700 hPa and the surface ($\text{LTSS} = \Theta_{700} - \Theta_{\text{surface}}$). Following the general methodology presented in that work, results were stratified by LTSS to control for variations in the atmospheric thermodynamic state. The average LTSS was found to be 17.4 K and four LTSS bins that encompass 90.5% of the data are defined from 12-24 K. The LTSS was derived from the ECMWF-AUX products that are available from the CloudSat data processing center and have been linearly interpolated in space and time to the CPR

radar bins.

2.3 Results

2.3.1 Non-Precipitating Clouds

Figure 2.1 shows the global trends of non-precipitating liquid cloud properties as a function of the aerosol index. This plot demonstrates a non-linear relationship between AI and the various cloud parameters, with two distinct regimes, one below $AI = 0.1$ and another above $AI = 0.2$. The high AI regime is typical of coastal regions particularly off the east coast of the Northern hemisphere continents and the west coast of equatorial Africa, whereas the low AI regime is typical of the pristine tropical and southern hemisphere ocean areas. Table 2.2 shows the magnitude of the linear fit between the various cloud properties and $\log_{10}(AI)$. Interpretation of the linear slopes must be qualitative in nature given the persistent non-linearities in the relationships between the cloud parameters and AI.

Figure 2.1a illustrates the relationships between the cloud droplet effective radius and the aerosol index. As expected, r_e tends to decrease with increasing AI and Table 2.2 confirms that the slope of the decrease is relatively independent of stability. A widely reported parameter is the slope of a linear fit of $\log_{10}(r_e)$ with $\log_{10}(AI)$. Averaged over the entire range of LTSS, this slope is found to be -0.07, in good agreement with the slopes found by *Matsui et al.* [2004] of -0.069 and *Bréon et al.* [2002] of -0.085. This parameter, while indicative of a direct aerosol effect on cloud microphysics, is not sufficient to identify an aerosol indirect effect on cloud albedo as it neglects the critical assumption of a constant liquid water path. Through the relationship in Equation 2.1 it would be predicted that if the effective radius decreases and the liquid water path remains constant then the optical depth must increase. Figure 2.1b demonstrates that τ does increase with increasing AI, however Table 2.2

Table 2.2: Slope of linear fit between various non-precipitating cloud parameters and $\log_{10}(\text{AI})$.

Parameter	Units	LTSS 12-15	LTSS 15-18	LTSS 18-21	LTSS 21-24	All LTSS
r_e	μm	-1.90	-2.23	-2.52	-1.88	-2.25
τ	none	0.55	0.98	1.24	1.40	0.91
LWP (MODIS)	g/m^2	-4.93	-1.58	0.77	4.35	-2.22
Cloudy Sky Albedo	none	0.001	0.014	0.018	0.023	0.007

highlights the fact that high LTSS environments show greater increases in τ that are inconsistent with the observed decreases in r_e .

The inconsistency between the slopes for r_e and τ imply variations in the water path response of clouds that depend on the thermodynamic stability. Therefore, it is critical to test the fundamental assumption of the Twomey effect, that is, that the liquid water path is independent of CCN concentration. MODIS cloud liquid water path is derived directly from τ and r_e using Equation 2.1. In addition, an independent estimate of cloud water from AMSR-E is used to verify results found using the optical method of MODIS. The two retrievals are based on entirely different physical principles, e.g. *Stephens and Kummerow* [2007], the optical method being based on reflection of solar radiation and the microwave retrieval being based on emission. Of additional interest, the microwave method is independent of the cloud microphysics for the non-raining clouds considered here, so the microphysical response of clouds to aerosol should have no bearing on results gleaned from this technique.

The trends of the liquid water path with aerosol index are shown in Figures 2.1c and 2.1d. Despite the relative bias, both instruments show similar trends, lending credence to the validity of this result. Both estimates show a hinge point near $\text{AI} = 0.15$, above which a modest but radiatively significant decrease in liquid water path is observed for all stability regimes. It is further seen in Table 2.2 that the strength of the relationship between LWP and AI is a function of the stability regime. The re-

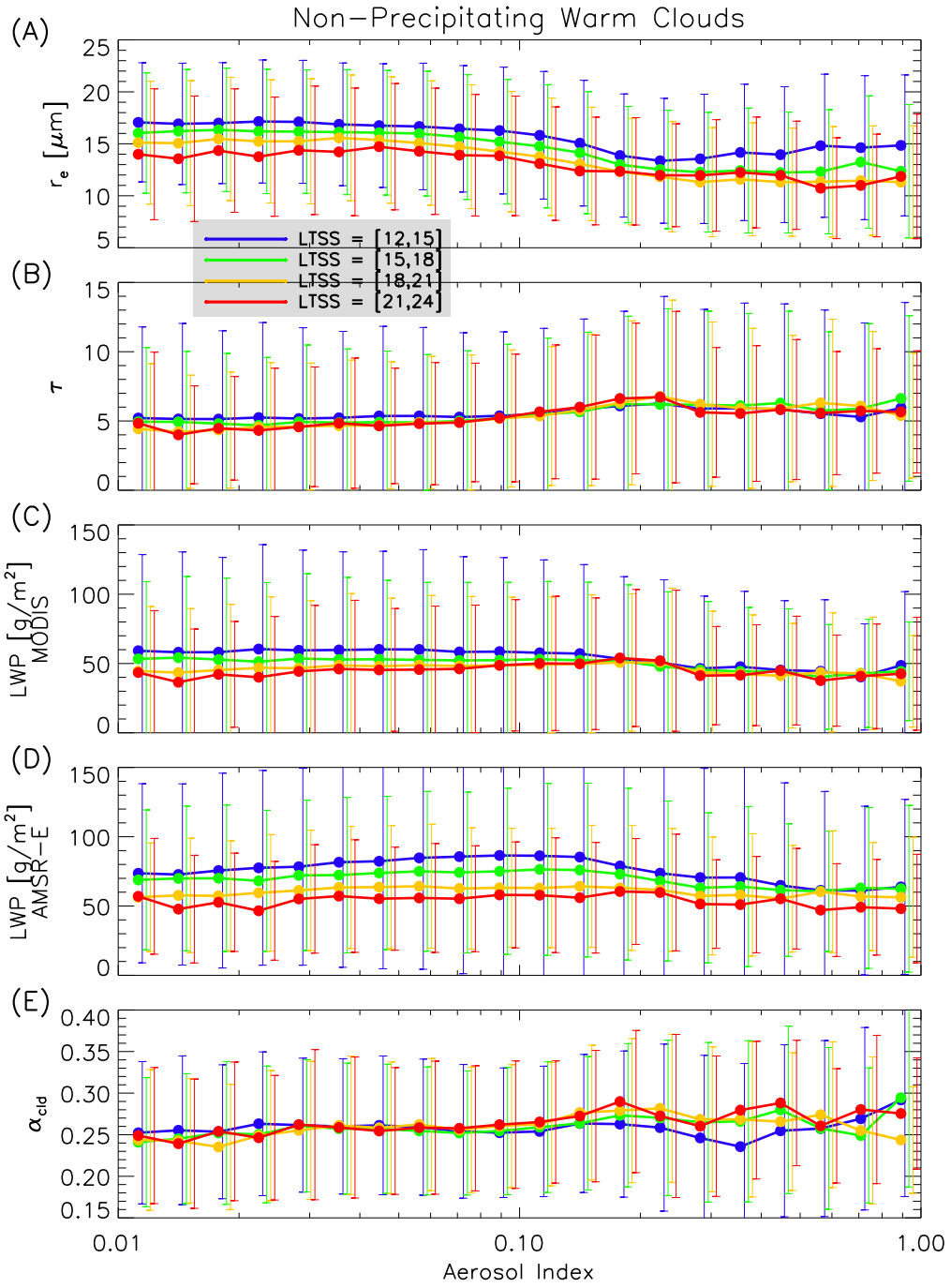


Figure 2.1: Global relationships between AI and non-precipitating cloud parameters. Circles represent the mean values and error bars show the standard deviation.

sults suggest that clouds in unstable environments suffer greater reduction in cloud liquid water path with increasing AI than those in more stable regimes. It should be noted that the magnitude of the relationships given in Table 2.2 are moderately sensitive to regional binning of the data, however, the LTSS dependence appears to be robust. This result could indicate that clouds that are more cumulus in nature are more susceptible to the entrainment and evaporation effects than are stratiform boundary layer clouds. This result is also consistent with that of *Han et al.* [2002] who demonstrated that the water path response is more strongly negative in warmer environments where decoupling of clouds from the boundary layer is more common. These results may also lend credence to the analytical mixed layer model results of *Wood* [2007], that indicate that clouds with higher cloud bases in unstable environments are susceptible to aerosol induced thinning whereas clouds with lower cloud bases in stable environments are not. Evidence that the tendency of the cloud type trends from cumulus to stratus with increasing LTSS is presented in Figure 2.2. This plot demonstrates that as LTSS increases the variability of the MODIS channel 1 reflectance decreases and the cloud fraction increases, indicative of a transition from more variable cumulus clouds to homogeneous stratus clouds. This global result fits well with the previous findings of *Klein and Hartmann* [1993] who found a robust correlation between LTSS and cloud fraction in several active stratocumulus regions. Therefore it is reasonable to conclude that LTSS may be utilized as an indicator of the dominant cloud type.

Any decrease in the liquid water path acts as a limit on the magnitude of the first indirect effect because the cloud albedo is a function of both r_e and LWP. This effect is illustrated in Figure 2.3, which shows the cloud albedo, derived from the two stream approximation [*Stephens et al.*, 2001], as a function of r_e and LWP. Overlain on these contours are the mean non-precipitating cloud r_e and LWP for a 'clean' and a 'dirty' state where the delineation between clean and dirty is somewhat arbitrarily

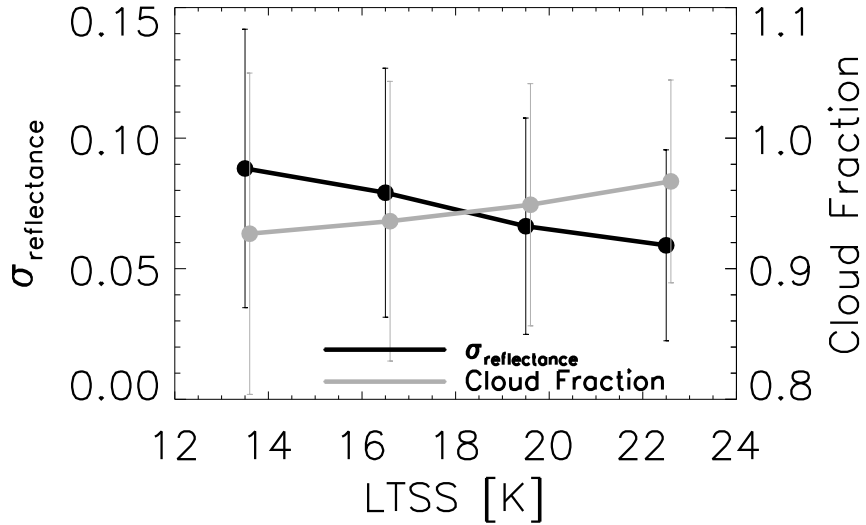


Figure 2.2: Global relationships between LTSS and the MODIS cloud fraction and the MODIS channel 1 ($0.645 \mu\text{m}$) reflectance variability. Cloud fraction is from a 3×3 pixel estimate taken from the CloudSat GEOPROF product. The standard deviation of the reflectance is calculated from an 11×11 pixel subset of the MODIS data surrounding the CloudSat footprint.

prescribed as $\text{AI} = 0.1$. The line connecting these points shows the approximate albedo trajectory of a cloud with increasing aerosol burden. The first indirect effect as proposed by *Twomey* [1977] would show a horizontal trajectory indicating a constant LWP with decreasing r_e . The mean decrease in LWP observed in the data acts to decrease the rate at which these trajectories cross the albedo contours with the decrease most evident in unstable environments. These results highlight the fact that it is necessary to consider changes in both r_e and LWP when examining the first aerosol indirect effect. It is also emphasized that clouds in unstable environments that tend to be more cumulus in nature are more susceptible to LWP decreases than are clouds in stable environments.

Increased CCN concentrations are proposed to have an indirect effect on the cloud albedo via their direct effect on cloud droplet size. Therefore observation of the indirect effect requires an independent estimate of the cloud albedo in addition to

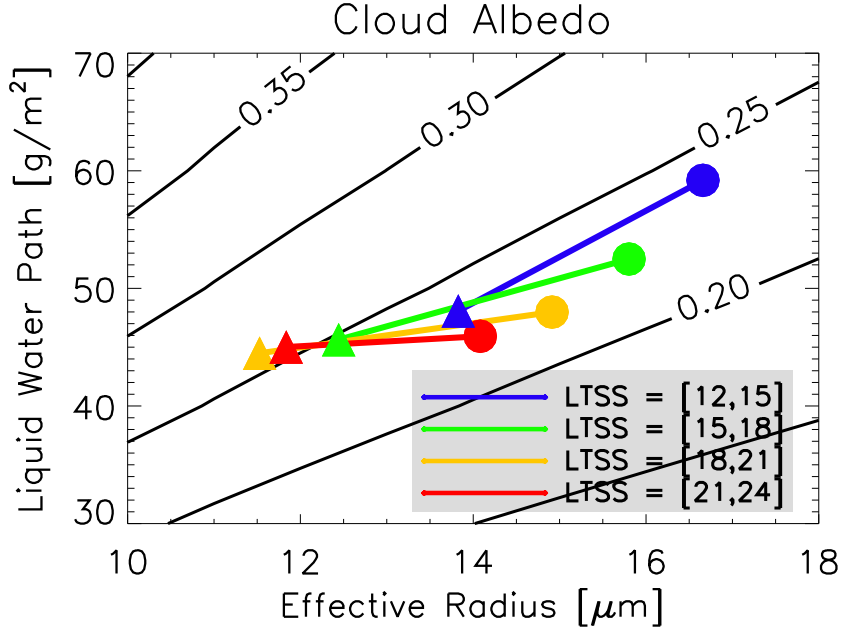


Figure 2.3: Cloud albedo derived from the two stream approximation. Circles(triangles) represent the mean r_e and LWP for a clean(dirty) state. The delineation between clean and dirty is given by $AI = 0.1$.

observation of r_e . This independent estimate is derived from the CERES top of the atmosphere (TOA) shortwave flux measurements. It must be acknowledged that the CERES instrument has a larger footprint than the MODIS cloud properties and the CloudSat rain flag and may contain some clear sky. In fact, on average, the CERES pixels used in this analysis contain 19.2% clear sky. To account for this fact and to eliminate any relationship between cloud fraction and AI the cloudy sky albedo is derived from the TOA flux. First dividing the observed upwelling TOA flux by the calculated incident TOA flux derives the all sky albedo. Second, the clear sky component of the flux is removed using the CERES estimate of clear sky area within the CERES field of view via,

$$\alpha_{cld} = \frac{\alpha_{all} - (1 - f)\alpha_{clr}}{f}, \quad (2.4)$$

Where f is the MODIS cloud fraction within the CERES footprint and α is the albedo.

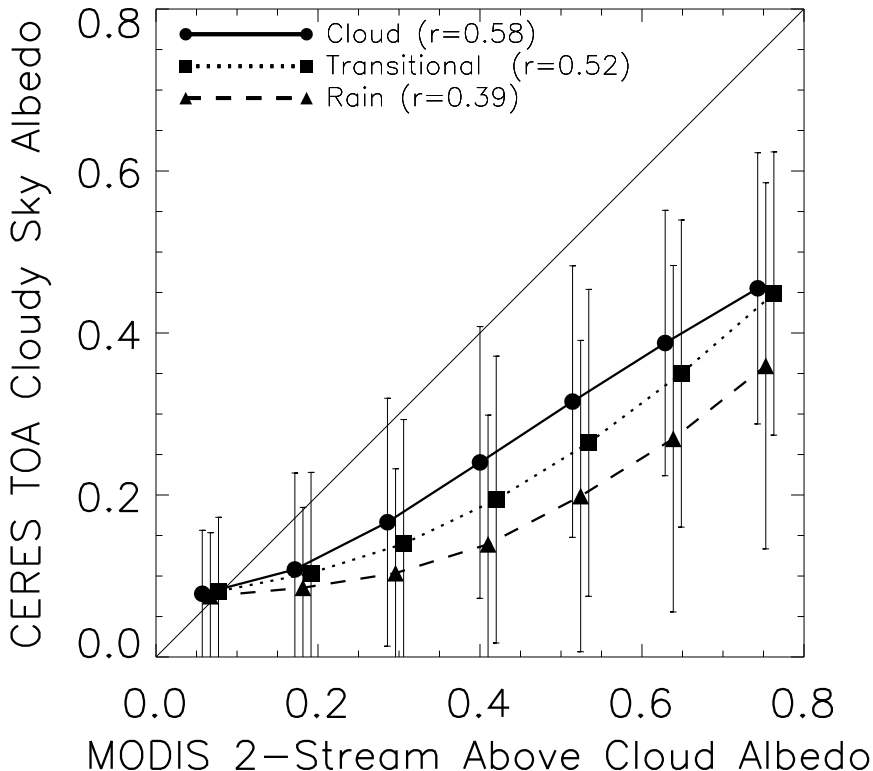


Figure 2.4: Comparison of the CERES TOA albedo with the cloud top albedo derived from the MODIS cloud products using a two stream radiative transfer model.

The trend of the CERES cloudy sky albedo with AI is given in Figure 2.1e, and again the magnitude of the trends are shown in Table 2.2. These independent estimates of albedo agree well with the previous results, indicating that the albedo enhancement is indeed diminished in the lower static stability regime presumably because the LWP decrease is larger in these environments than in the high stability regime. This independent result adds credence to the observations that clouds in unstable environments tend to suffer decreases in LWP not observed in stable environments. The analysis has been performed with both the CERES TOA cloudy

sky albedo and a cloud top albedo derived using the MODIS cloud products (τ, r_e) and the two stream approximation. Both estimates of cloud albedo lead to the same conclusions, therefore the following results show the CERES albedo because it provides an independent estimate of this quantity. Figure 2.4 demonstrates that the two products are well correlated. The high bias of the MODIS estimate results from the sensor resolution differences and the fact that MODIS is a cloud top estimate as opposed to the TOA estimate of CERES.

Although the previous results suggest that the constant liquid water path approximation is not valid on the global scale, it is still of interest to examine the constant liquid water path case. To do this cloud properties are examined as a function of LWP. For example, the CERES cloud albedo is plotted against LWP for four stability and aerosol regimes in Figure 2.5a. This plot demonstrates that for a constant LWP the increase in albedo is greater for high LWP clouds than it is for low LWP clouds. This result might be slightly counter-intuitive, as one would expect a saturation of the cloud albedo for high LWP. An explanation for this phenomenon can be found in Figure 2.5b, which shows r_e as a function of LWP for the same stability and aerosol regimes as in Figure 2.5a. The sensitivity of the effective radius to AI increases with LWP and this in turn results in an increased sensitivity of the optical depth to AI. It can be predicted that the sensitivity of r_e to aerosol should increase with increasing LWP by considering the LWP of a vertically homogenous cloud with a mean volume radius \bar{r}_v , number concentration N , and thickness H ,

$$\text{LWP} = \frac{4}{3}\pi\rho_l\bar{r}_v^3NH. \quad (2.5)$$

Invoking the common relationship $\bar{r}_v^3 = kr_e^3$ [Martin et al., 1994], [Brenquier et al.,

2000], solving for r_e and differentiating with respect to N yields,

$$\Delta r_e = -\frac{1}{3} \left(\frac{3}{k4\pi\rho_l} \right)^{1/3} \frac{\text{LWP}^{1/3}}{H^{1/3}N^{4/3}} \Delta N. \quad (2.6)$$

Here it is apparent that for a given aerosol perturbation, the sensitivity of the effective radius should increase proportionally to $\text{LWP}^{1/3}$. The data indicate that the increased sensitivity of cloud microphysical properties to AI at high LWP overcomes the decreased sensitivity of cloud albedo to optical depth at high LWP.

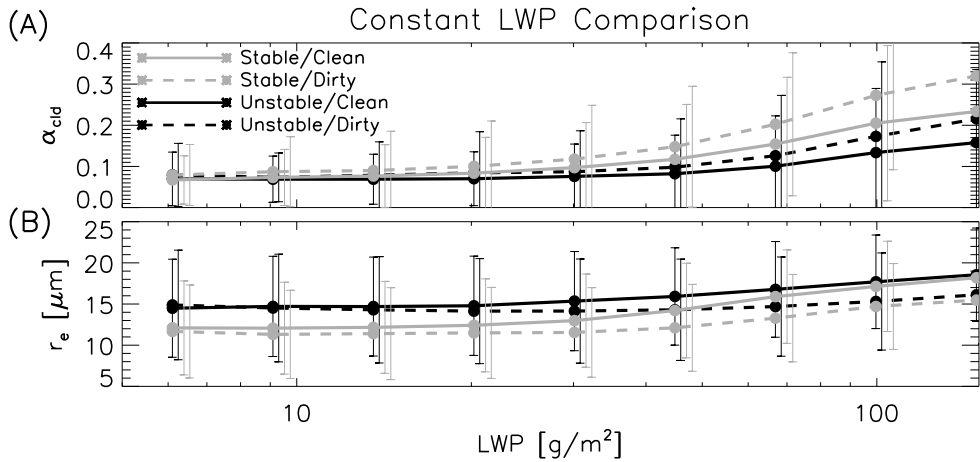


Figure 2.5: Trends of the (A) CERES cloudy sky albedo and (B) MODIS r_e with the AMSR-E LWP. The delineation between clean and dirty is given by $\text{AI} = 0.1$. The stable curve represents all LTSS between 18 and 21 K. The unstable curve represents all LTSS between 12 and 15 K.

2.3.2 Precipitating Clouds

The previous results apply to non-precipitating clouds only, and it is expected that the response of clouds undergoing a vigorous coalescence process will be different from that of non-precipitating clouds. In this section, the differing responses of non-precipitating, transitional, and precipitating clouds are examined. Here, it is reiterated that the transitional clouds may or may not have rain reaching the surface, but they certainly contain large drops indicative of a vigorous coalescence process.

Figure 2.6 illustrates the global relationships between cloud parameters and the AI for the three cloud types and Table 2.3 shows the strength of the linear relationships between the parameters and $\log_{10}(\text{AI})$. The focus of this section is on the transitional and precipitating clouds, however non-precipitating clouds are included to emphasize the dramatically different responses of the cloud water budgets of the three cloud types.

Figure 2.6a demonstrates that a decrease in effective radius with increasing AI is observable in all stages of cloud lifetime, even clouds that are certainly precipitating. Interpretation of the remotely sensed r_e in the transitional and precipitating clouds that have bimodal size distributions is difficult, however the radiative implications of this result are more straightforward, as can be seen in Figure 2.6b, which shows that cloud optical depth increases commensurate with the decreasing r_e for all cloud regimes. These results suggest that clouds in all stages of their life are susceptible to albedo enhancement of the first indirect type.

As in the non-precipitating case, it is critical to examine aerosol effects on precipitating clouds in the context of the cloud water budget. Figure 2.6c shows the average LWP as a function of AI for the three cloud regimes. This estimate of LWP is derived from AMSR-E, and is the cloud component of the water path only. The non-precipitating clouds show a moderate decrease in water path whereas the transitional and precipitating clouds show fairly dramatic increases in water path. The linear slopes highlighted in Table 2.3 suggest that this slope is of the order of several dozen g/m^2 for an order of magnitude increase in AI for transitional and precipitating clouds. The inferred explanation for this result would be an inhibited coalescence process in the presence of enhanced aerosol resulting in greater amounts of cloud water. Note also the similarity between the trends of τ and LWP, highlighting the important dependence of the cloud radiative properties on the liquid water path. The similarity between these trends is indicative of the dominance of the water path effect over the

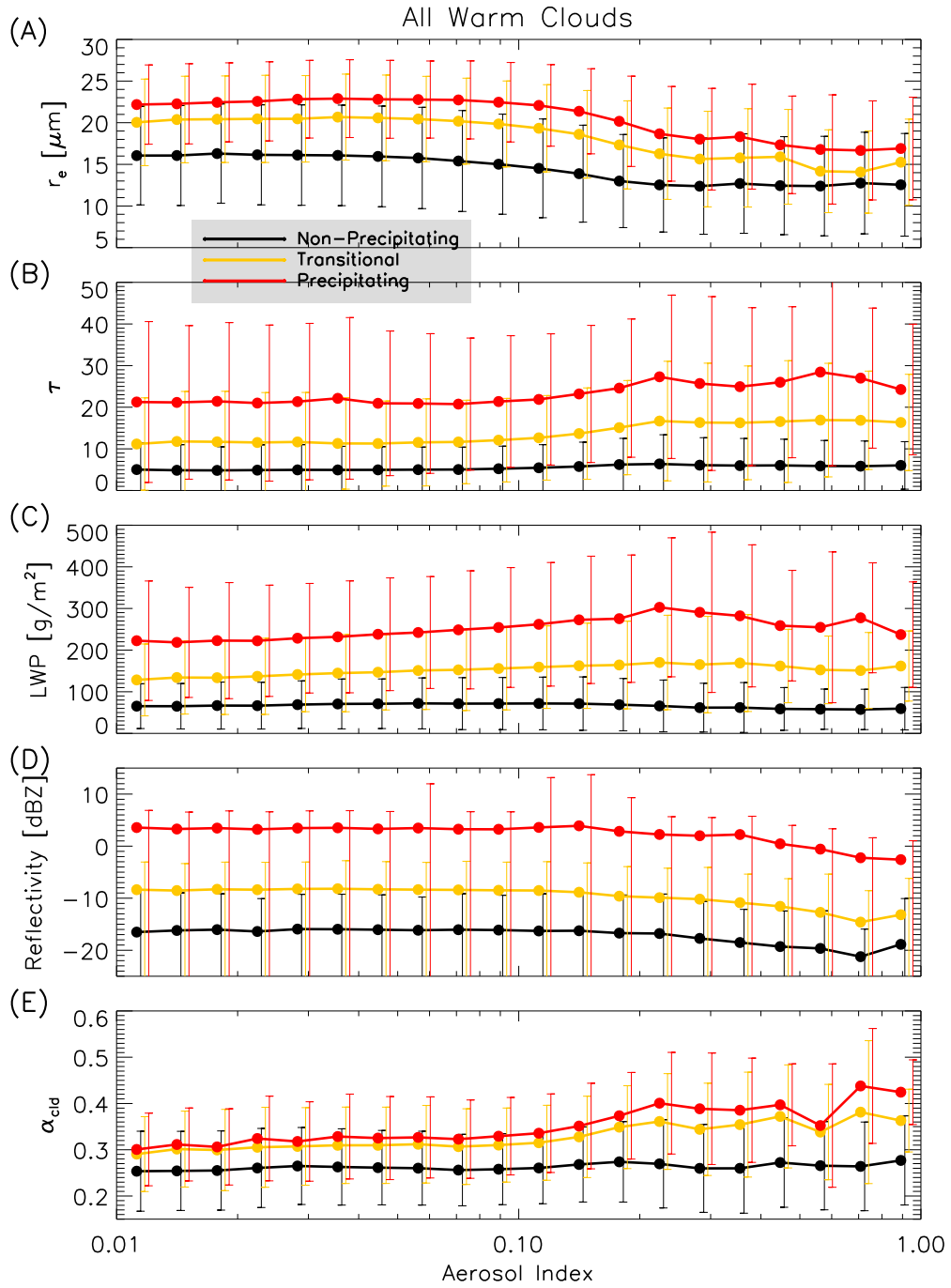


Figure 2.6: Global relationships between AI and non-precipitating, transitional, and precipitating cloud parameters. Circles represent the mean values and Error bars show the standard deviation. The LWP estimate is for the cloud component only from AMSR-E. The reflectivity is the CPR vertical cloud mean reflectivity factor.

Table 2.3: Slope of linear fits between cloud parameters and $\log_{10}(\text{AI})$. Comparison of non-precipitating, transitional and precipitating clouds.

Parameter	Units	Non-Precipitating	Transitional	Precipitating	All Clouds
r_e	micron	-2.25	-2.04	-1.37	-2.32
τ	none	0.90	2.37	2.01	0.67
LWP (AMSR-E)	g/m ²	0.29	21.32	41.73	0.30
Cloudy Sky Albedo	none	0.007	0.027	0.040	0.008
Reflectivity	dBZ	-0.57	-1.14	-0.69	-0.37

r_e effect in precipitating and transitional clouds.

It should be noted that the microwave estimate of the cloud water in transitional and precipitating clouds path suffers from uncertainty due to algorithm assumptions that are not required in non-precipitating clouds. It is of primary concern that a single precipitation drop size distribution (DSD) is used in the retrieval. For non-precipitating clouds the Rayleigh approximation may be used to model the cloud emission as a function of the LWP alone in the 37 GHz channel used for the cloud water retrieval, however this approximation breaks down and the Mie theory must be invoked to model the emission properties of precipitation-size drops. For example, in the Mie regime larger drops emit more efficiently than smaller drops for a fixed precipitation water content. Therefore, if the retrieval algorithm incorrectly partitions the water between cloud and rain or simply distributes the precipitation water over an incorrect DSD, the emission characteristics of the cloud will be modeled incorrectly, resulting in an error in the water path estimate. Despite this and other difficulties, interpretation of the trends of water path with AI are less troublesome. As an example, consider errors that derive from the DSD assumption. One would expect smaller drops in the high AI environments. These smaller drops would be less efficient emitters than large drops resulting in a potential underestimation of total water in the high AI regime. However, the opposite trend is seen in LWP, suggesting that the trends seen in Figure 2.6c are real as opposed to an artifact of retrieval

assumptions, and may in fact be underestimated.

While Figure 2.6c demonstrates that aerosol enhances LWP in precipitating and transitional clouds, additional evidence is required to indicate that a suppressed coalescence process is the responsible mechanism. To this end Figure 6d shows the relationship between AI and the mean cloud reflectivity. This quantity has been shown to be proportional to the coalescence rate [*Stephens and Haynes, 2007*], and due to its dependence on the sixth moment of the drop size distribution, is most sensitive to large drops. Although this result is qualitative in nature it is indicative of inhibited coalescence rates and smaller cloud droplets and precipitation drops for all cloud regimes with increasing AI. Figure 2.7 shows that along with an inhibited coalescence process, the probability of precipitation is suppressed in high AI environments. This result is stratified by AMSR-E CWV, which is well correlated with the probability of precipitation. The consistency of the trend in all water vapor regimes suggests that precipitation suppression could be widespread in nature. Finally, Figure 2.8 demonstrates that for any given LWP the probability of precipitation is reduced in the high AI regime by approximately 5% in all LWP bins above 80 g/m^2 , indicating that more water must condense in dirty clouds before the onset of precipitation. This result is qualitatively consistent with in situ observations of stratocumulus [*van Zanten et al., 2005*], [*Pawlowska and Brenguier, 2003*] that indicate that clouds must grow deeper as droplet number concentration increases before precipitation begins.

The enhanced LWP of transitional and precipitating clouds implies an enhanced albedo response of these clouds relative to non-precipitating clouds. This is confirmed in Figure 2.6e and Table 2.3, which demonstrate that the albedo effect is substantially enhanced for transitional and precipitating clouds. Analyses of albedo effects resulting from aerosol suppression of precipitation are generally focused on the cloud lifetime or the cloud fraction. The effect identified here is different because the cloud fraction effects have been removed from the cloudy sky albedo estimate. The dramatic albedo

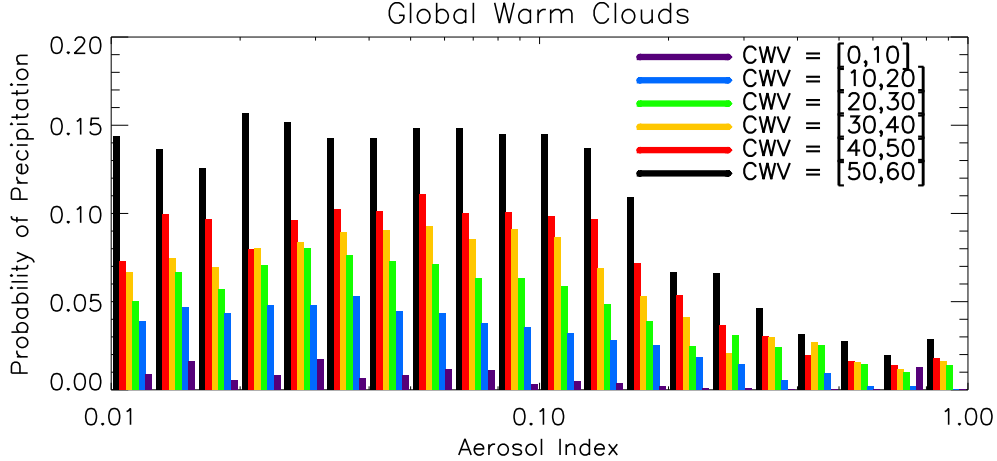


Figure 2.7: The global conditional probability of warm cloud precipitation as a function of AI for various column water vapor regimes. The units for CWV are kg/m^2 .

enhancement identified here results from LWP enhancement alone.

2.4 Conclusions

Aerosol indirect effects are analyzed in the context of the liquid water budget of clouds. Additionally, to control for thermodynamic effects, results are stratified by the lower tropospheric static stability or the column water vapor. The results broadly identify the importance of accounting for aerosol effects on both the cloud effective radius and the cloud liquid water path simultaneously due to the substantial dependence of the cloud albedo on the LWP. Aerosol effects on non-precipitating clouds are shown to be dominated by r_e , however a non-negligible decrease in LWP is identified. In contrast, aerosol effects on precipitating clouds are dominated by an increasing LWP effect. Two general regimes are identified. The first is a regime in which aerosol enhances entrainment and droplet evaporation thereby reducing LWP and the second is a regime in which aerosol suppresses coalescence thereby inhibiting precipitation and increasing LWP. Independent estimates of the cloudy sky albedo derived from the CERES sensor confirm that the albedo responds to the identified LWP perturbations.

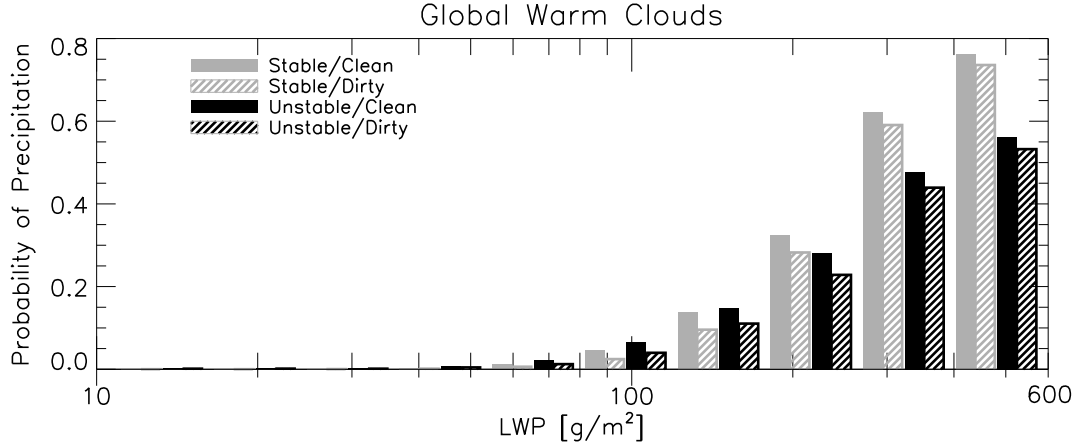


Figure 2.8: Trends of the conditional probability of warm cloud precipitation with LWP. The delineation between clean and dirty is given by $AI = 0.1$. The stable regime represents all LTSS between 18 and 21 K. The unstable regime represents all LTSS between 12 and 15 K.

It is shown that the constant liquid water path assumption, commonly invoked in analysis of the first indirect effect, is invalid on the global scale. The LWP of non-precipitating clouds decreases regardless of the LTSS. The reduction in LWP acts to counter the radiative effects of the corresponding decrease in r_e . The magnitude of the LWP reduction is found to be dependent on the LTSS. Unstable low LTSS environments are observed to suffer greater decreases in LWP and corresponding reduction in cloudy sky albedo than their counterparts in stable high LTSS environments. This result could be indicative of greater entrainment of sub-saturated air leading to greater evaporation in cumulus clouds than in stratiform clouds. Results further indicate that the sensitivity of r_e and cloud albedo increase with increasing liquid water path.

Unlike non-precipitating clouds that suffer modest decreases in LWP, precipitating and transitional clouds undergo dramatic increases in LWP with increasing AI. As a result the albedo enhancement of the precipitating and transitional clouds is greater than that of non-precipitating clouds. These results appear to be indicative of an inhibited coalescence process. For example, evidence is presented that greater amounts of water must condense in dirty environments than in clean environments before the

onset of precipitation. This assertion is further supported by results that indicate lower cloud reflectivity in high AI environments. Additionally, the occurrence of warm precipitation is reduced by as much as 10%, depending on the thermodynamic environment, in the high AI regime.

The majority of results presented in this chapter are based on global analysis and are primarily correlative in nature. While great effort was made to control for the effects of the large scale thermodynamics by binning results by either LTSS or CWV, any correlations between AI and the thermodynamic variables could potentially lead to false conclusions. Likewise, while thermodynamic forcings were considered, dynamic forcing were not addressed. Therefore, it is cautioned that these results, particularly those dealing with the water path response of clouds, warrant substantial further exploration and confirmation on regional and seasonal scales. In particular, both modeling and observational studies are needed to confirm the suggestion that cumulus clouds are more susceptible to entrainment effects than stratiform clouds. Furthermore, model parameterization of indirect effects used in global climate simulations should include the various LWP responses of clouds identified here.

Chapter 3

Estimating the Global Oceanic Aerosol Indirect Albedo Sensitivity

Abstract

The magnitude of the aerosol indirect albedo sensitivity (IAS) is calculated as the sum of distinct cloud regimes over the global oceans. Selection of the cloud regimes is guided by the observation that both thermodynamic stability and the presence of precipitation affect the sensitivity of cloud albedo to aerosol concentrations. The calculation accounts for the both the regional and seasonal distribution of these cloud regimes as well as the seasonal distribution of solar insolation. The IAS, defined as the change in warm cloud albedo for a fractional change in aerosol burden, is found to be $-0.42 \pm 0.38 \text{ Wm}^{-2}$ over the global oceans. Twenty five percent of the effect is due to precipitating clouds despite the fact that only eight percent of clouds are identified as precipitating. The disproportionate effects of precipitating clouds result from commensurate increases in cloud depth and water path with aerosol observed in these clouds. The non-precipitating cloud effects are confined to areas of frequent low level stratiform cloud cover, whereas the precipitating cloud effects appear to be more widespread in nature. An additional assumption of the anthropogenic aerosol fraction

provides an estimate of the indirect albedo forcing (IAF) of $-0.13 \pm 0.14 \text{ Wm}^{-2}$, which is significantly lower than the range provided by climate model estimates.

3.1 Introduction

Aerosol-cloud-precipitation interactions are a complex and poorly understood set of phenomena. These interactions are premised on the observation [*Pruppacher and Klett, 1997*] that cloud droplet number concentrations are related to ambient cloud concentration nuclei (CCN) concentrations. From this observation and a theoretical relationship relating cloud droplet size to cloud albedo, *Twomey [1977]* hypothesized that for a fixed liquid water path (LWP) polluted clouds will be brighter than unpolluted clouds. This effect has commonly come to be known as the first indirect effect. Furthermore, from knowledge of the collection kernels of cloud droplets, which have a strong dependence on droplet size [*Long, 1974*], it may be inferred that changes in ambient aerosol concentrations will modify the cloud droplet size distribution, thus changing the coalescence efficiency and delaying the onset of or suppressing precipitation. *Albrecht [1989]* proposed that a suppression of precipitation processes could increase cloud lifetime and subsequently the cloud fractional coverage, thus modifying the planetary albedo. A related hypothesis was proposed by *Pincus and Baker [1994]*, who argued that precipitation suppression would increase cloud depth and the lofted liquid water content, resulting in deeper, wetter, more reflective clouds. Modest evidence for this effect has been presented by *Koren [2005]*. The combination of these potential aerosol effects are commonly referred to as the aerosol second indirect effect. In addition to the first and second indirect effects, cloud dynamical feedbacks have been identified in modeling results that may affect both cloud microphysical properties as well as cloud water content and cloud coverage, as was outlined in Chapter 2.

Because of the complicated manner in which aerosol may interact with cloud microphysical properties and macrophysical structure, a simple empirical definition of indirect radiative effects is adopted here. The division is based upon the two most important parameters of the clouds in terms of shortwave radiation: the cloud albedo (α_{cloud}) and the cloud fractional coverage (CF). The indirect albedo sensitivity (IAS) represents the total sensitivity of the conditional cloud albedo to aerosol regardless of the responsible physical process. The indirect coverage sensitivity (ICS) is defined as the total sensitivity of the cloud fraction to aerosol regardless of physical process. The IAS is closely related to the first indirect radiative effect, whereas the ICS is generally identified with the second indirect radiative effect. The division of indirect effects amongst these two parameters offers a more readily observable metric for identifying indirect radiative effects than the complicated and poorly understood chain of microphysical events that comprise the various physical processes associated with aerosol-cloud-precipitation interactions.

Observation of the ICS is notoriously difficult due to potential biases in the relationships between remotely sensed aerosol and cloud properties due to three-dimensional radiative transfer effects [Wen *et al.*, 2007] and aerosol humidification effects near cloud boundaries [Haywood *et al.*, 1997; Charlson *et al.*, 2007; Koren *et al.*, 2007] that could result in artificially large aerosol burden associated with larger cloud fraction. Due to these probable regime dependent biases in the observed ICS, this work focuses solely on the IAS.

Quantification of aerosol indirect radiative forcing remains the largest source of uncertainty in estimation of the total anthropogenic component of radiative forcing [Forester *et al.*, 2007]. At the time of the fourth assessment report, model based estimates of the first indirect effect ranged from -0.22 to -1.85 Wm^{-2} . These models differ in their treatment of aerosol indirect effects. Most estimates use a parameterization relating cloud droplet number concentrations to aerosol concentrations. Some

provide estimates of the second indirect effect whereas others do not. Likewise, some models have relaxed the assumption of a constant liquid water path. A variety of different anthropogenic aerosol species are considered in the calculation.

Recently, several observational estimates of the aerosol indirect forcing have been made. *Nakajima et al.* [2001] use one season of global oceanic AVHRR data to estimate the first indirect effect as -1.3 Wm^{-2} . *Sekiguchi et al.* [2004] extend these results to a full year of data and estimate the first indirect effect as $-0.37 \pm 0.09 \text{ Wm}^{-2}$ using AVHRR, and $-0.64 \pm 0.16 \text{ Wm}^{-2}$ using POLDER. *Quaas et al.* [2008] make a major improvement in methodology by utilizing the observed TOA albedo from CERES to estimate the first indirect effect as $-0.9 \pm 0.4 \text{ Wm}^{-2}$. The aforementioned observational estimates of the first indirect effect employ varying datasets and methodology, contributing to the large spread in the range of estimates. One common feature of all studies is that they neglect to control for variations with meteorological variables other than aerosol.

In light of the large spread in both model and observational estimates of the cloud albedo effect, this chapter expands upon the results of the previous chapter to make a new estimate of the magnitude of the aerosol indirect effect over the global oceans, while highlighting the differing sensitivities of the various cloud regimes. It was highlighted in the previous chapter that clouds in different meteorological regimes (defined by different values of LTSS) exhibit different sensitivities of albedo to aerosol burden. These variations in sensitivity are explicitly considered here in calculating the first aerosol indirect effect over the global oceans. To perform this calculation, a new methodology is introduced in which the aerosol indirect effect is calculated as the sum of individual regimes weighted by their respective frequency of occurrence.

3.2 Data and Methodology

3.2.1 Data

The datasets and data reduction methodology employed in this analysis are nearly identical to those used in Chapter 2, however the time period is extended to a full two years (July 2006 - June 2008). One additional step is included in this work to filter out CloudSat pixels where the surrounding 3x5 pixel swath of MODIS pixels contain clear sky. This has the effect of filtering out heterogeneous scenes within the larger AMSR-E and CERES footprints. Due to the extensive filtering described in the previous chapter, including both the MODIS radiance data and the CloudSat vertical profiles, these data may be considered representative of global oceanic warm clouds with little contamination from ice or mixed phase clouds.

The representation of precipitation occurrence is modified slightly from the previous study by eliminating the transitional designation. Here a cloud is defined as precipitating if the path integrated attenuation exceeds 20 dB or if the path integrated attenuation exceeds 2 dB and the reflectivity in the lowest vertical bin exceeds 7.5 dBZ. These thresholds correspond to precipitation flags 2 and 3 in the Cloudsat 2C-Precip-Column product (*Haynes et al.*, 2009). All other clouds, including those missed by CloudSat but observed by MODIS, are identified as non-precipitating.

3.2.2 Calculating the indirect albedo sensitivity

To account for regional variations in the calculation of the IAS, the global oceanic region from 60N to 60S is subdivided into 1x1 degree latitude-longitude regions. Within each region the indirect effect is calculated as the weighted average of individual regimes given by various values of LTSS and precipitation occurrence. Two precipitation regimes are defined as precipitating and non-precipitating. Likewise, three stability regimes are defined as ($LTSS < 15$ K, $LTSS = [15-18$ K], $LTSS > 18$

K. The combination of two precipitation and three stability regimes results in six total cloud regimes as follows:

- 1 Precipitating, $LTSS < 15$ K
- 2 Precipitating, $LTSS = [15-18$ K]
- 3 Precipitating, $LTSS > 18$ K
- 4 Non-Precipitating, $LTSS < 15$ K
- 5 Non-Precipitating, $LTSS = [15-18$ K]
- 6 Non-Precipitating, $LTSS > 18$ K

The regional annual mean distribution of the various stability and precipitation regimes are shown in Figures 3.1 and 3.2, and the global probability distribution of LTSS is shown in Figure 3.3. Stable conditions are observed primarily in the subtropical stratocumulus regions and the extra-tropical storm track regions whereas unstable conditions dominate well known convective regions of the inter-tropical convergence zone, the South-Pacific convergence zone, the Indian Ocean and the Carribean. The intermediate stability regime is found in regions generally associated with shallow trade cumulus in a gradual transition from the stable to unstable regions. Similar distributions are found in the probability of warm precipitation with warm clouds in unstable tropical environments that are much more likely to grow to depths great enough to initiate precipitation processes.

The relative frequency of occurrence of each of the cloud regimes, the total low cloud fraction, and the diurnally averaged insolation varies significantly throughout the year within each one degree box. To grossly account for this temporal variation the annual cycle is divided into four seasons given by:

- 1 December-January-February (DJF)
- 2 March-April-May (MAM)

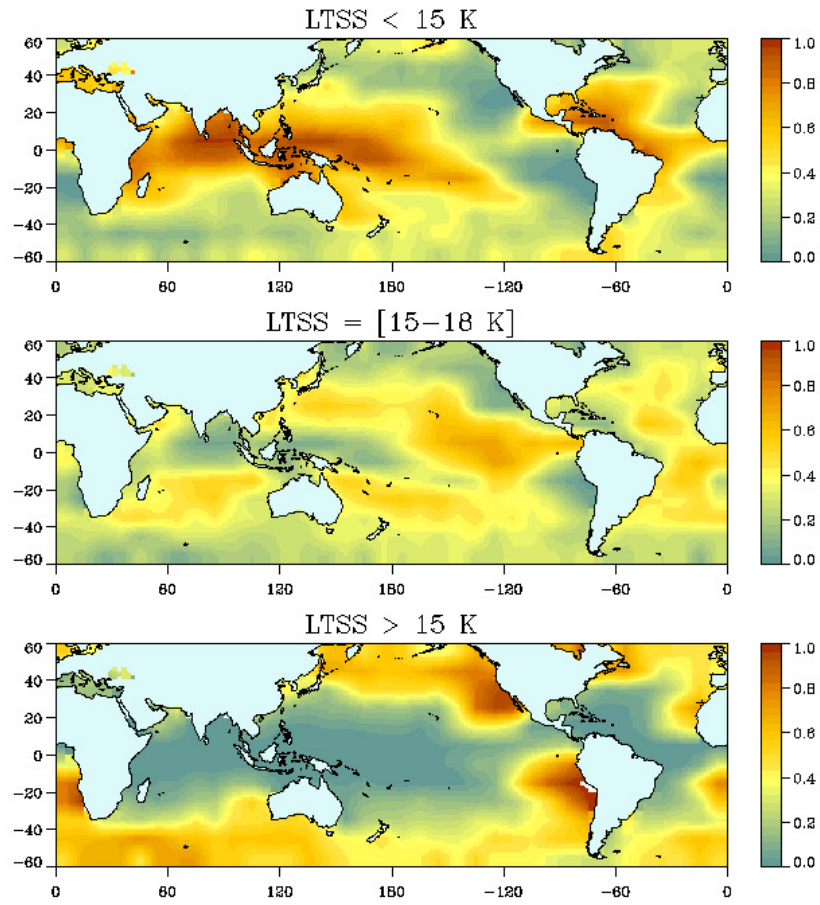


Figure 3.1: The annual mean spatial distributions of the three stability regimes

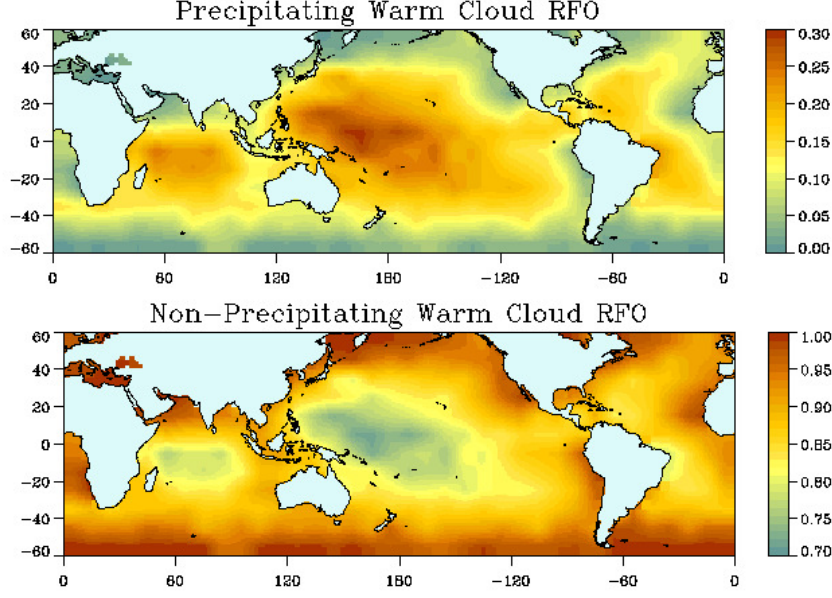


Figure 3.2: The annual mean spatial distribution of the probability of precipitation of warm clouds

3 June-July-August (JJA)

4 September-October-November (SON)

Figure 3.4 shows the seasonal mean insolation calculated from well known Fourier expansions of the Earth's orbital parameters [Liou, 2002] and Figure 3.5 shows the low cloud fraction derived from MODIS observations. Insolation is of course heavily weighted toward the summer hemisphere. Interestingly, the warm cloud fraction is also weighted toward the summer hemisphere, implying a coupling between the latitudinal distribution of the liquid cloud fraction and the solar insolation.

Within each 1x1 degree region, the seasonal IAS is calculated for each cloud regime as,

$$IAS_{i,j} = S_i f_j r_{i,j} F_{o,j}, \quad (3.1)$$

where i represents the cloud regime, j represents the season, S is the albedo sensitivity, f is the low cloud fraction, r is the relative frequency of occurrence of each regime, and F_o is the incoming solar radiation. Within each region the annual mean may

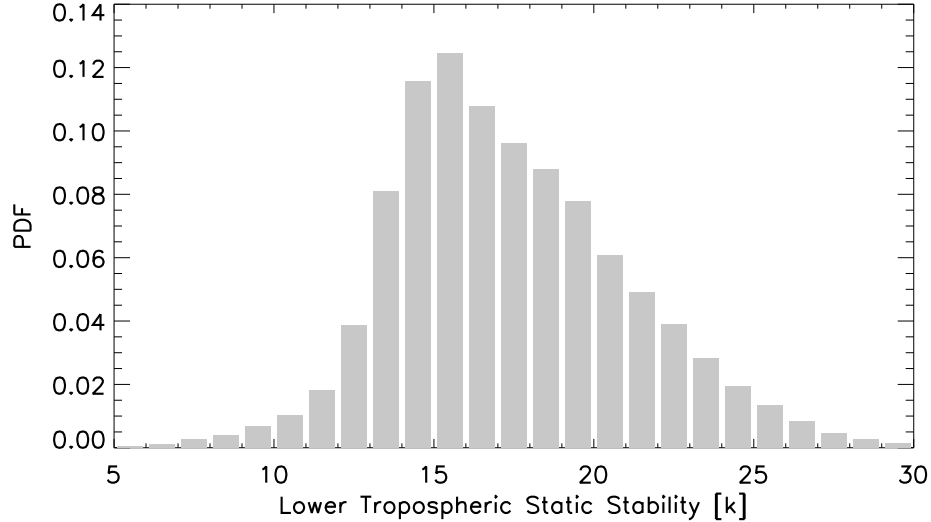


Figure 3.3: Probability distribution function (PDF) of the global distribution of the ECMWF derived lower tropospheric static stability (LTSS).

then be calculated as the sum over all seasons and all cloud regimes,

$$\text{IAS} = \sum_i^6 \sum_j^4 \text{IAS}_{i,j}. \quad (3.2)$$

Likewise any combination of regimes and or seasons may be combined by summing over only those regimes and seasons. Specifically, the calculation will be divided into precipitating and non-precipitating components in the sections that follow to highlight the drastically different albedo sensitivities of these two types of clouds. Finally, the total oceanic IAS may be calculated by taking an area weighted average of the oceanic IAS distribution.

3.2.3 Calculating the cloud parameter sensitivities

The previous section outlined a methodology to calculate the global IAS given an albedo sensitivity (S) for each cloud regime. The precise nature of S however has yet to be defined. In this section a method is described to calculate the sensitivity of each cloud parameter to $\ln(\text{AI})$ along with an associated uncertainty.

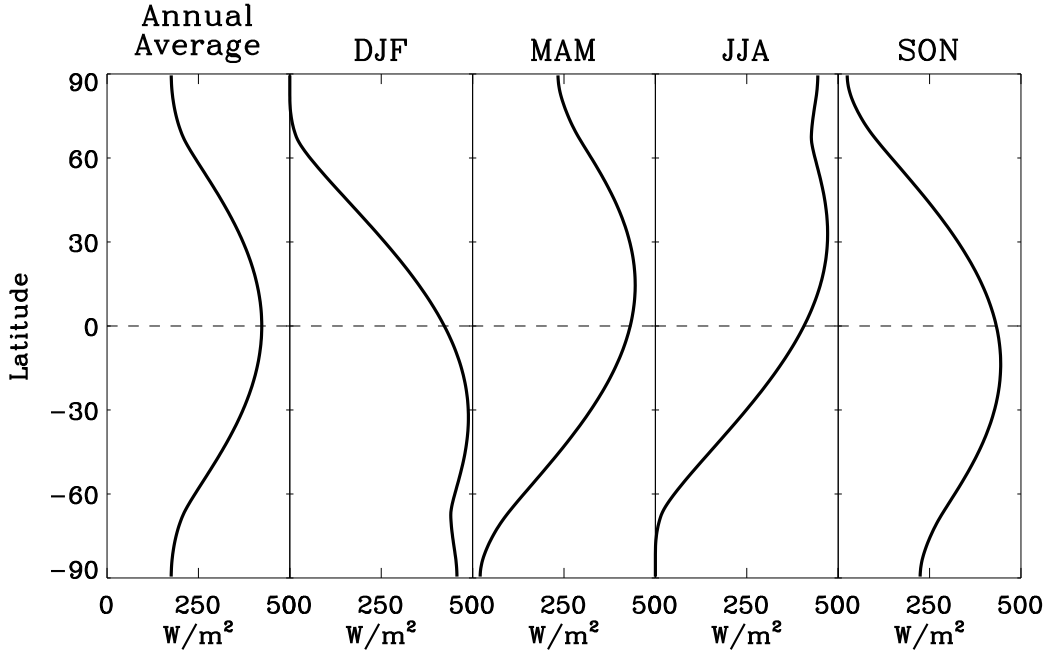


Figure 3.4: The annual average and the seasonal mean distribution of the top of the atmosphere solar insolation as a function of latitude.

First, the data is divided into 10 equidistant $\ln(\text{AI})$ bins between 0.001 and 1.0. Within each bin the mean and standard deviation of each cloud parameter is calculated. The global sensitivity is then calculated as the slope of the best fit line between the $\ln(\text{AI})$ bin centers and the mean bin values with error weighting given by the standard deviation within each bin. This procedure implicitly assumes that clouds have been adequately sampled within each AI bin to account for both the natural variability of the cloud properties and the observational uncertainty. Figure 3.6 shows the binned data for the particular case of the cloudy sky albedo for each of the six cloud regimes. Similar plots are produced for each cloud parameter (r_e , LWP, H) where H is the cloud height. Given the large data volume used in this study (average bin density is 4094), it is reasonable to interpret the resultant uncertainty in the global sensitivity parameter as a measure of the large natural variability of the cloud properties, particularly the LWP.

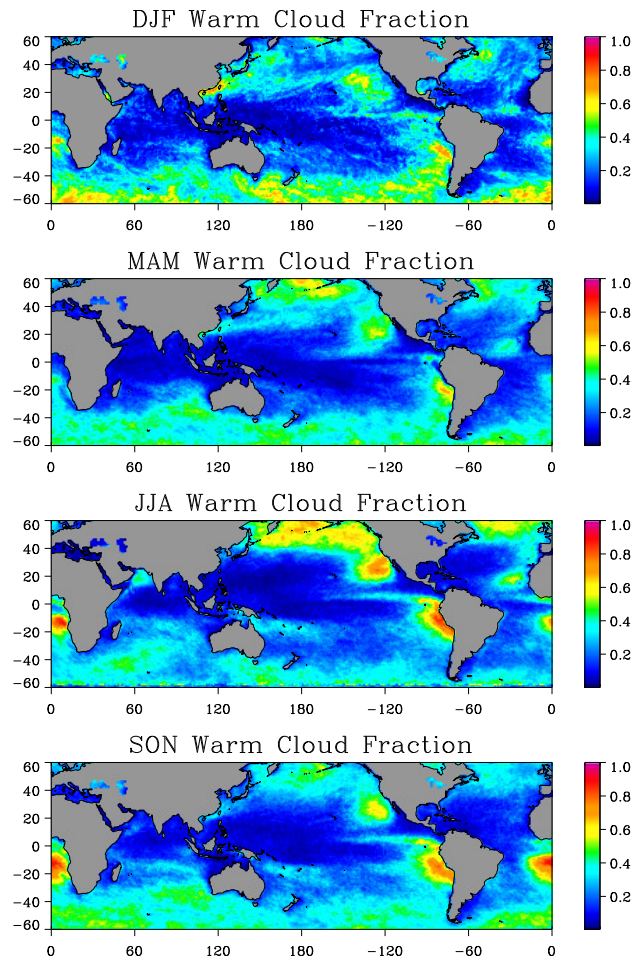


Figure 3.5: The seasonal mean spatial distribution of the warm cloud fraction as observed by MODIS

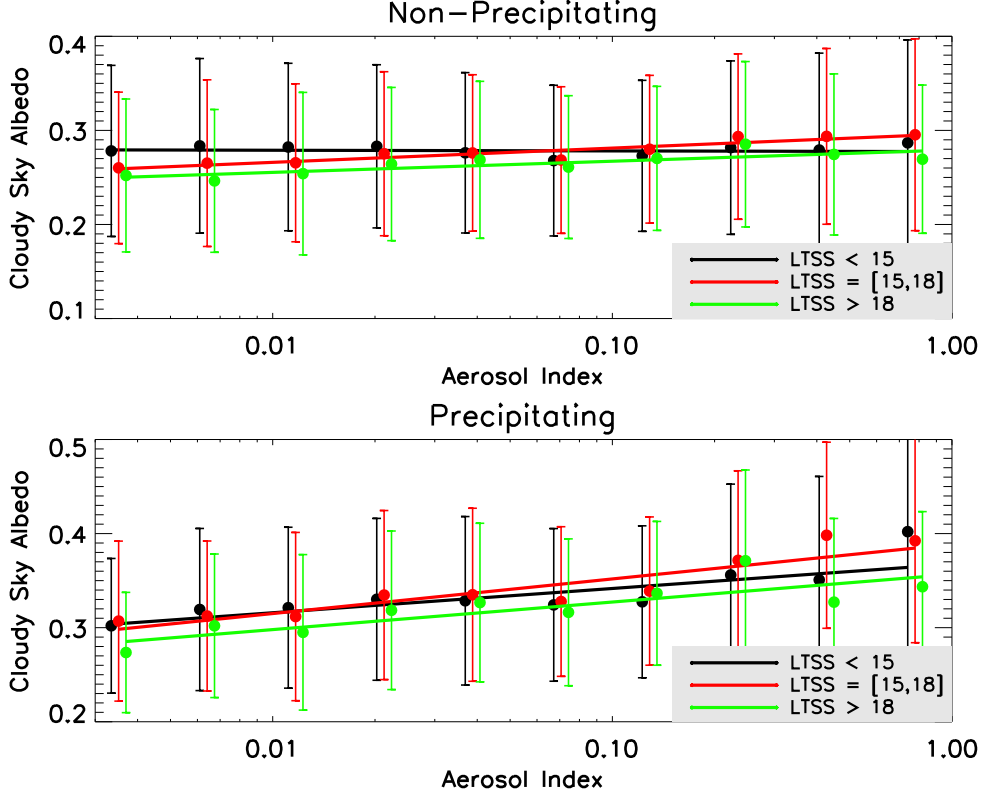


Figure 3.6: The CERES cloudy sky albedo as a function of the aerosol index for each of the six cloud regimes. Error bars show the standard deviation of the albedo within each AI bin.

Defining the cloud parameter sensitivities in terms of the logarithm of AI has two advantages. The first advantage is that the global distribution is lognormal (See Figure 3.7) so a logarithmic adjustment to the data is preferred for statistical applications. Second, the sensitivity of a cloud parameter (y) of the form $\frac{\Delta y}{\Delta(\ln(\text{AI}))}$ may be approximately rewritten as,

$$\frac{\Delta y}{\Delta(\ln(\text{AI}))} \approx \frac{\text{AI}\Delta y}{\Delta \text{AI}}. \quad (3.3)$$

Therefore, these sensitivities represent the approximate change in a cloud parameter (y) given a fractional change in AI. It follows that multiplication of the sensitivity by the estimated fractional increase in AI due to anthropogenic sources provides an esti-

mate of the anthropogenically induced change in any of the given cloud parameters.

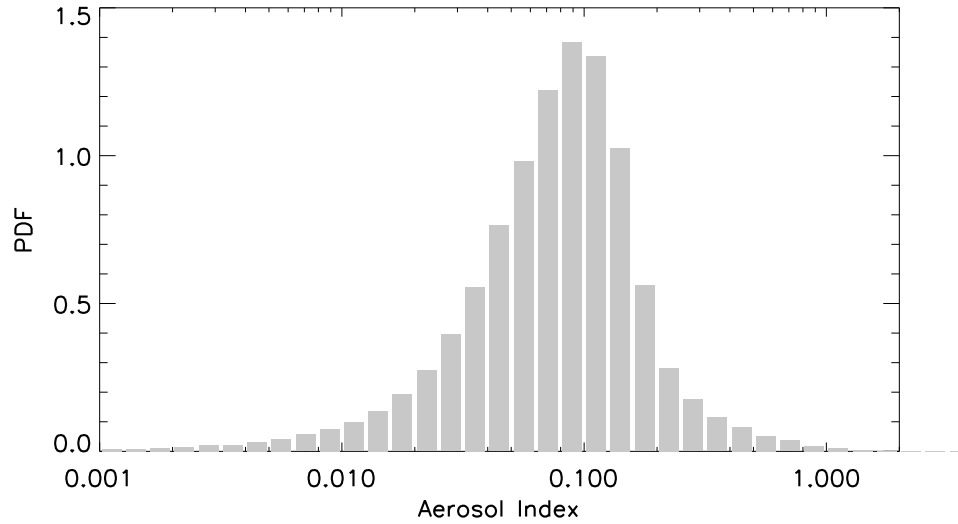


Figure 3.7: Probability distribution function (PDF) of the global distribution of the MODIS derived aerosol index (AI).

3.3 Results

3.3.1 Cloud parameter sensitivities

Global statistics of the cloud parameter sensitivities, similar to those derived in Chapter 2 are derived for each of the six cloud regimes following the methodology outlined in section 3.2.3. These statistics are highlighted in Figure 3.8 along with the relative frequency of occurrence of each of the regimes. The results shown in this figure reinforce the findings of the previous chapter and demonstrate that similar sensitivities are found in the extended data set employed here. Of particular interest are the six derived sensitivities of the cloud albedo to $\ln(\text{AI})$ along with their associated uncertainty estimates, which are used in the subsequent calculations of the IAS.

For the case of non-precipitating clouds, all regimes show a reduction in cloud effective radius with increasing aerosol burden on the order of 1 micron for a unit fractional change in AI. This direct microphysical effect of aerosol appears to be a

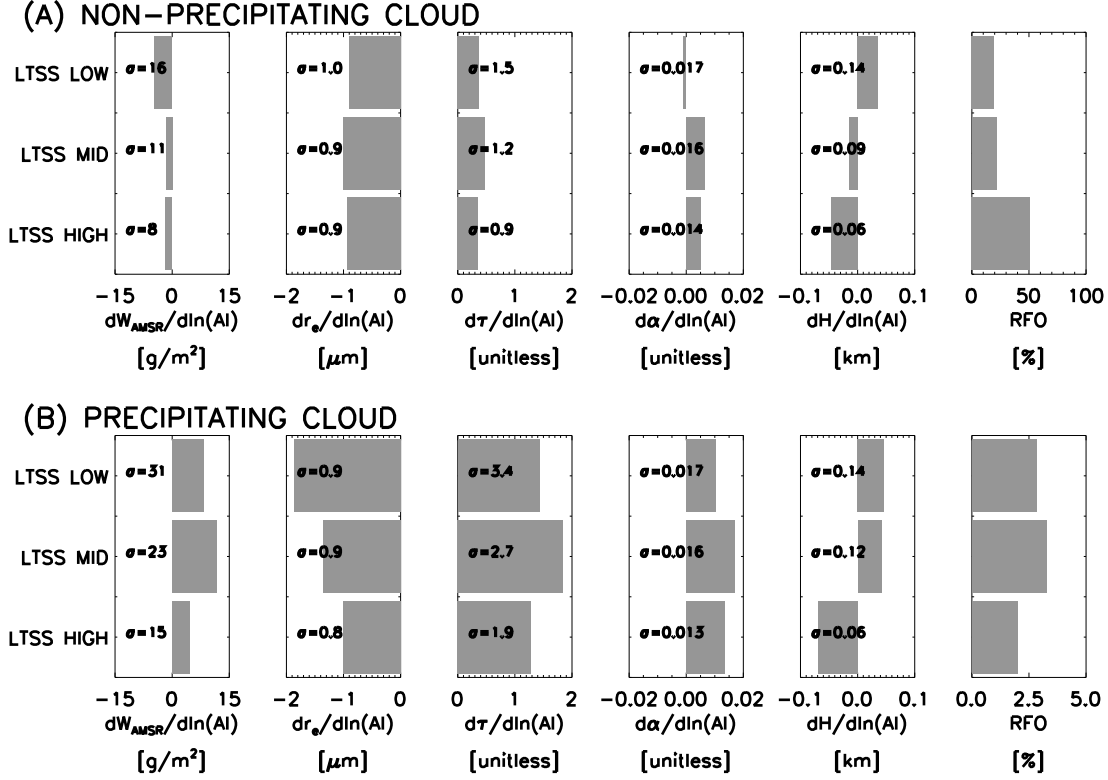


Figure 3.8: The sensitivities of the cloud parameters for each of the six cloud regimes. (A) shows the non-precipitating cloud sensitivities and (B) shows the Precipitating clouds. The σ values are the associated uncertainties that are described in Section 3.2.3

ubiquitous result evident in clouds regardless of regime. Importantly, the consistent reduction in cloud radius does not manifest itself as a consistent reduction in the cloudy sky albedo in all regimes. In fact the most unstable regime shows almost no sensitivity in albedo whereas the middle and high stability regimes show modest increases in albedo. This result is consistent with the observation that the low stability regime suffers a noticeable reduction in LWP whereas the middle and high stability regimes suffer only minor reductions in LWP. As was suggested in Chapter 2, the discrepancies between the various LTSS sensitivities may result from an enhancement of entrainment drying effects in shallow cumulus clouds relative to stratiform clouds.

Interesting results are shown in the case of non-precipitating cloud height sensi-

tivities (Figure 3.8a). A transition is seen in the sensitivities from low to high LTSS regimes with clouds in the low stability regimes tending to increase in height with increasing aerosol and clouds in the high stability regime showing a decrease in height. A simple mixed layer model [Wood, 2006] indeed predicts such a reduction in cloud height for typical boundary layer stratiform clouds with increasing aerosol number concentration due to entrainment effects. Unlike their stratiform counterparts, clouds in unstable environments tend to increase in cloud height. These environments would be indicative of a weak temperature inversion. This behavior is consistent with the idea that these clouds would have to grow to greater heights before the onset of precipitation [Pinkus and Baker, 1994], providing the first support for this effect on the global scale.

Precipitating clouds (Figure 3.8b) show decreases in cloud radius on the order of those observed in the case of non-precipitating clouds further demonstrating the robust nature of this result. Unlike non-precipitating clouds, however, all stability regimes show increased LWP and a commensurate increased cloud optical depth with increasing AI. The resulting albedo sensitivities for precipitating clouds are substantially greater than those for non-precipitating clouds. Taken together, these results are supportive of the second aerosol indirect effect whereby aerosol decreases coalescence efficiency resulting in an increase in cloud condensate. Precipitating cloud height sensitivities are qualitatively similar to those of non-precipitating clouds. Both the middle and low stability regimes show increases in cloud height with increasing aerosol, which is again supportive of the second indirect effect resulting in decreased coalescence rate and delayed onset of precipitation. Note that increases in cloud height in the highest stability regime should not be expected due to the strength of the capping inversion in these environments.

3.3.2 Magnitude of the indirect albedo sensitivity

Figure 3.9 shows the regional distribution of the IAS as described in Section 3.2.2. The calculation has been divided into a precipitating and non-precipitating component. The total (cloud+rain) IAS is largest in the subtropical stratus region and to a lesser extent in the extratropical storm tracks both of which are regions of extensive stratiform cloudiness. This result is to a large extent merely a reflection of the distribution of oceanic warm cloud cover. When broken down into precipitating and non-precipitating cloud regimes, the non-precipitating cloud effect is isolated specifically to the stratiform cloud regions whereas the precipitating cloud effect is observed to be more widespread extending into the West Pacific and Indian Oceans. Again, this is primarily a reflection of the relative distribution of precipitating versus non-precipitating clouds. The importance of these results is that they show a distribution of the regions that will be most susceptible to the first indirect effect as well as the various second indirect effects and further provide a rough estimation of the relative importance of each to the global cloud albedo sensitivity. The strongly capped stratiform marine boundary layer clouds are much more susceptible to the first indirect effect due to their large areal extent as well as their relative insensitivity to entrainment drying dynamical feedback effects. Shallow cumulus clouds on the other hand are much more susceptible to the assortment of second indirect effects than their stratiform counterparts because they are much more likely to grow deep enough to initiate a vigorous coalescence process that will result in the initiation of rainfall.

The ocean-wide averages of the IAS with respective uncertainties are summarized in Figure 3.10. The area weighted global mean IAS is $-0.42 \text{ Wm}^{-2} \pm 0.38 \text{ Wm}^{-2}$ over oceans. The IAS of the precipitating clouds that arises from both decreased droplet radius as well as from deeper clouds with enhanced water paths is approximately 25% of this total despite the fact that only 8% of the clouds in the analysis were found to

be precipitating, highlighting the importance of the poorly understood relationships between LWP and aerosol in quantifying indirect albedo effects.

To convert the global IAS to a radiative forcing requires an additional assumption of the fractional increase in atmospheric aerosol number from pre-industrial to modern times. This number is highly uncertain with estimates ranging from 10% to 40% [Nakajima *et al.*, 2001]. Here, it is assumed that the anthropogenic fraction is 30% \pm 20% covering the aforementioned range. If it is further assumed that the increase in aerosol due to anthropogenic activity is globally uniform then the indirect albedo forcing (IAF) follows as $-0.13 \text{ Wm}^{-2} \pm 0.14 \text{ Wm}^{-2}$. The assumption of a uniform increase in aerosol burden is certainly not correct, however it is useful because it provides a rough estimate of the global magnitude of the IAF. The result provided here is substantially lower than previous estimates of the first indirect radiative forcing. In particular, the range of model derived estimates from the IPCC FAR is -0.22 to -1.85 Wm^{-2} and observational estimates range from -0.37 to -1.3 Wm^{-2} . The relatively low value for the IAF reported here follows from the near zero sensitivity of the non-precipitating cloud albedo in the low stability regime, which comprises about 20% of the observed warm clouds. The near zero value for S is found despite a clear reduction in particle radius in this regime further highlighting the importance of the water path response of clouds to aerosol. It follows that estimates of aerosol indirect effects that neglect the complex relationships between aerosol burden and LWP may tend to be biased high in their IAF estimates.

3.4 Summary

The indirect albedo sensitivity of warm clouds over the global ocean is calculated as a combination of unique cloud regimes, including various values of lower tropospheric static stability and precipitation occurrence. The global value of the IAS is found

to be $-0.42 \text{ Wm}^{-2} \pm 0.38 \text{ Wm}^{-2}$ of which 25% is found to result from precipitating clouds despite the fact that only 8% of the warm clouds in the study were identified as precipitating. Conversion of the IAS into a radiative forcing gives a value of $-0.13 \text{ Wm}^{-2} \pm 0.14 \text{ Wm}^{-2}$, which is significantly lower than most previous model and observational estimates of the IAF.

The results highlight the important role of the LWP response of clouds to aerosol in estimating the IAF. Specifically, 20% of the clouds in the study fall into the non-precipitating, low LTSS regime in which the albedo sensitivity is found to be approximately zero despite a clear reduction in cloud effective radius. This occurs due to a simultaneous reduction in LWP that offsets the radius effect. The LWP of non-precipitating clouds found in high stability regimes associated with stratiform cloudiness have relatively constant water path, which is more consistent of the assumptions of Twomey's first indirect effect. An additional key result of the study is that precipitating clouds in all stability regimes tend to have increased LWP with increased aerosol, which tends to amplify the IAS for these clouds relative to the fixed water path assumption.

Results are shown that also suggest a complex relationship between aerosol and cloud depth. In environments with high stability clouds tend to decrease in height with aerosol whereas in unstable environments clouds tend to increase in height, which could be indicative of a decreased coalescence efficiency resulting in delayed onset of precipitation and longer cloud lifetime. The datasets used are insufficient to determine if there is a commensurate increase in cloud fractional coverage. Instead the focus is on the LWP and the conditional cloud albedo as postulated by *Pincus and Baker* [1994].

A final note must be made of possible sources of uncertainty in the parameter sensitivities described in this work. The interpretation of the cloud parameter sensitivities described here assumes that the relationships are causal in nature. One

requirement for the assertion of causality is a physical model describing the phenomena in question. In the case of the ubiquitous reduction of cloud droplet size with increasing AI a simple, easily interpreted microphysical model does explain the observed behavior. Additionally, the observed relationships between AI and the cloud water path as well as the cloud height can be explained by modeling results. However, the expected effects of aerosol on LWP act through a complex and poorly understood chain of events involving the coalescence process and cloud dynamical feedbacks that make interpretation difficult. Furthermore, aerosol cloud interactions are known to occur in both directions with aerosol effecting cloud through their action as CCN and cloud affecting aerosol through aerosol processing and as a catalyst for chemical reactions. Additionally, cloud properties derive primarily from the thermodynamic and dynamic state of the atmosphere leaving the effects of aerosol microphysics as a third order phenomena. An attempt has been made here to control for these effects by binning results into thermodynamic regimes. nonetheless, there is certainly a possibility that residual correlations exist between AI and other meteorological parameters. This possibility causes an additional level of uncertainty in assigning causality to these relationships. The identifications of these possible sources of bias brings to light the need for substantial future work in examining the global relationships found here in more detail. In particular, future research should expand upon the regime methodology introduced here, perhaps applying it on smaller spatial and shorter temporal scales and adding additional meteorological information to refine the definition of the regimes.

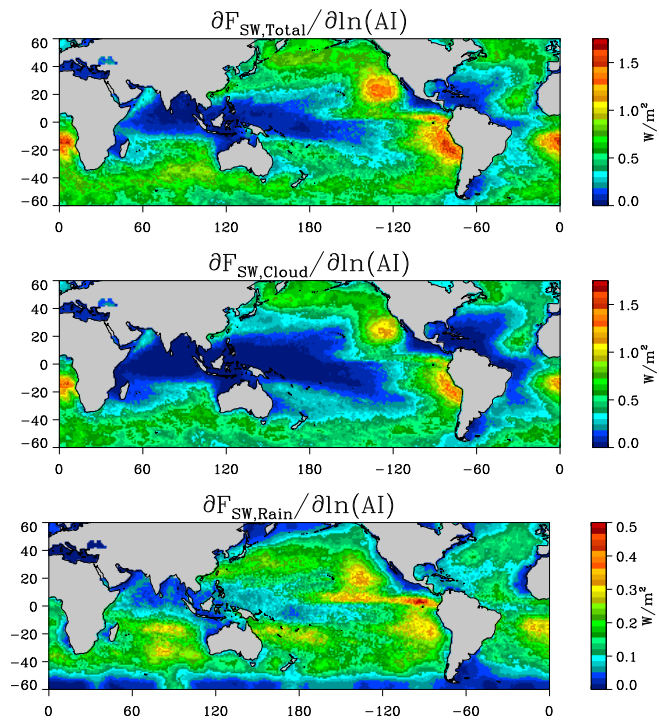


Figure 3.9: Regional distribution of the IAS as described in Section 3.2.2. Results are divided into precipitating and non-precipitating clouds.

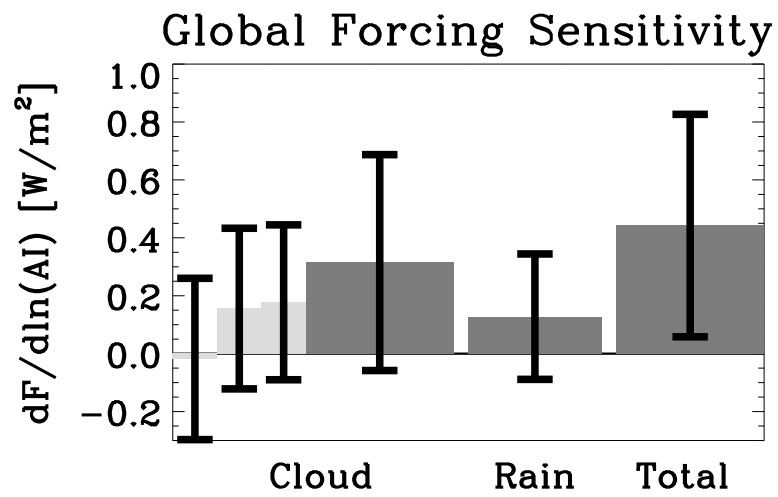


Figure 3.10: The global IAS as described in Section 3.2.2. Results are divided into precipitating and non-precipitating clouds. The cloud component is additionally broken down into the three stability regimes.

Chapter 4

An Observed Tropical Oceanic Radiative-Convective Cloud Feedback

Abstract

Anomalies of precipitation, cloud, thermodynamic, and radiation variables are analyzed on the tropics-wide mean spatial scale. In particular, relationships between the mean tropical oceanic precipitation anomaly and radiative anomalies are examined. It is found that tropical mean precipitation is well correlated with cloud properties and radiative fields. In particular, the tropical mean precipitation anomaly is positively correlated with the top of the atmosphere reflected shortwave anomaly and anti-correlated with the emitted longwave anomaly. The tropical mean relationships are found to primarily result from a coherent oscillation of precipitation and the area of high-level cloudiness. The correlations manifest themselves radiatively as a modest cooling at the top of the atmosphere, and a redistribution of energy from the surface to the atmosphere through reduced solar radiation to the surface and decreased longwave emission to space. The anomalous atmospheric column radiative heating is found to be about 10% of the magnitude of the anomalous latent heating. The tem-

poral signature of the radiative heating is observed in the column mean temperature that indicates a coherent phase-lagged oscillation between atmospheric stability and convection. These relationships are identified as a radiative-convective cloud feedback that is observed on intra-seasonal timescales associated with the Madden-Julian oscillation in the tropical atmosphere. A composite analysis showing the spatial patterns of the anomalies provides evidence that the feedback mechanism works through a modulation of the strength of the large-scale tropical overturning circulations.

4.1 Introduction

The tropical atmosphere is composed of large-scale meridional and zonal overturning circulations that dynamically link regions of moist ascending motion with regions of dry descent. Understanding this dynamically connected system requires simultaneous observation of both the ascending and descending branches of the circulations. For example, *Pierrehumbert* [1995] emphasizes the importance of the tropical circulation, suggesting that the relative areas of moist ascending motion and dry descending motion play a key role in regulating tropical climate. *Wallace* [1992] also highlights the crucial role that must be played by dynamics in regulating tropical climate, arguing for the importance of the fractional area of the tropics covered by reflective high cloud. *Hartmann and Michaelson* [1993] further demonstrate that the strong local correlations observed between sea surface temperature (SST) and radiation parameters become extremely weak when the averaging area is extended over the entire tropical pacific from 30S-30N. Therefore, to address the problem of tropical climate, it is necessary to consider an averaging area comparable to the spatial extent of the large-scale circulations. For the tropics this area would correspond to the meridional Hadley and zonal Walker circulations.

Many studies have examined the top of the atmosphere (TOA) Earth radiation

budget [*Vonder Haar and Suomi*, 1969; *Harrison et al.*, 1990; *Cess et al.*, 2001]. While this approach has contributed greatly to our understanding of the climate system, examining only the TOA budget can be misleading because the near cancellation of cloud shortwave (SW) and longwave (LW) forcing at the TOA in the tropics [*Kiehl and Ramanathan*, 1990; *Kiehl* [1994] obscures important differences in the manner in which the shortwave and longwave components of the radiation budget interact with the surface (SFC) and the atmospheric column (ATM). For example, in the particular case of high clouds, *Stephens and Webster* [1981] point out that all but the thinnest high clouds tend to cause a cooling of the Earth surface and a warming of the atmospheric column. Also, relatively few studies have examined the radiation budget on time scales relevant to moist atmospheric processes. Notable exceptions are the studies of *Collins et al.* [1996], *Lin and Mapes* [2004], and *Stephens et al.* [2004]. All of these studies demonstrate that the cloud fields associated deep convection are associated with radiative heating of the atmosphere and cooling at the surface. These results are applicable locally to areas of deep convection. There remains some question to what extent they apply to the tropics as a whole, which motivates the exploration of the relationships between precipitation and radiation fields on a tropics-wide basis.

An important element of the atmospheric column radiation budget is its coupling to the global hydrologic cycle. This relationship is commonly understood through the paradigm of radiative-convective equilibrium [*Manabe and Wetherald*, 1967] whereby atmospheric radiative cooling is balanced energetically by the transfer of latent heat from the surface to the atmosphere through the action of moist convection. This concept may also be understood through a statement of the atmospheric column energy balance,

$$-R_{atm} = LP + S + F, \quad (4.1)$$

where R_{atm} is the atmospheric radiative heating rate, L is the latent heat of vaporization, P is the precipitation rate, the product LP is the column latent heating, S

is the surface sensible heat flux, and F is the horizontal transport of sensible energy. This statement of energy balance must also be true of the anomalies (represented by primes),

$$-R'_{atm} = LP' + S' + F', \quad (4.2)$$

Over the tropical oceans S is much smaller than P and assuming that the anomalous energy transport is small as well gives the approximate expression,

$$-R'_{atm} \approx LP', \quad (4.3)$$

which states that atmospheric radiative heating anomalies are approximately balanced by latent heating anomalies through a modified precipitation rate.

The theoretical formulation provided in Equation 4.3 ignores sensible heating and transport effects but includes cloud feedbacks that could potentially dampen or amplify the hydrologic cycle response. Therefore, a critical aspect of this approximation is quantifying the sign and magnitude of these potential feedbacks. To this end, this study attempts to quantify one aspect of the cloud feedback in the present climate. Specifically, evidence is presented for a radiative-convective cloud feedback that acts to dampen the hydrological response to increased radiative cooling by roughly 10%. Commensurate negative feedbacks are implied at the TOA and the surface. To identify this feedback, relationships are quantified between precipitation and the tropical radiation budget. Furthermore, time-lagged relationships are analyzed that demonstrate the existence of the feedback mechanism on intra-seasonal time scales in the current tropical atmosphere. Evidence is presented that the feedback acts through variability in the MJO and in the strength of the large-scale tropical overturning circulations. Finally, the applicability of this feedback to future climate scenarios is discussed.

4.2 Data

Five years (2003-2007) of tropical oceanic (30S-30N) one-degree gridded daily daytime data from NASA’s Aqua satellite are analyzed. Estimates of oceanic precipitation rate are offered from the advanced microwave scanning radiometer-E (AMSR-E) using the Goddard profiling algorithm (GPROF) [Kummerow *et al.*, 2001]. Cloud properties from the moderate resolution imaging spectro-radiometer (MODIS) level 3 one-degree daily average cloud products [Platnick *et al.*, 2003] are employed from collection five. MODIS variables used include the total cloud optical depth (τ), cloud fraction (CF), cloud top temperature (CTT), cloud top pressure (CTP), and the τ -CTP joint histograms. Additionally, atmospheric infrared sounder (AIRS) temperature profiles [Aumann *et al.*, 2003] are used to diagnose the structure of atmospheric heating. AIRS provides infrared and a microwave based temperature and water vapor profiles that are available from the surface to 200 hPa under substantially overcast conditions [Susskind *et al.*, 2003]. In this work pressure weighted column mean temperatures are calculated. Only pixels in which all pressure levels contain valid data values are considered so as not to bias the results in instances where lower atmosphere data may be missing due to cloud and precipitation contamination.

The clouds and Earth’s radiant energy system (CERES) instrument [Wielicki *et al.*, 1996] offers estimates of the TOA and surface broadband longwave and shortwave fluxes. In this work the single scattering footprint (CERES-SSF FM3 Edition2B and Edition2C) products are aggregated to daily one-degree averages. A time dependent user applied correction factor that has been approved by the CERES science team is applied to the CERES shortwave data to account for spectral darkening of the shortwave channel (see data quality summary available at <http://eosweb.larc.nasa.gov>). To account for the variation of the solar flux with solar zenith angle, the daily mean (represented by an overbar) shortwave flux is approximated from the instantaneous estimate as $\overline{F_{SW}} = F_{SW}(\overline{F_o}/F_o)$, where F_{SW} is the observed reflected component and

F_o is the incident component of the TOA solar flux. The surface radiative fluxes are estimated using the surface model-B that provides estimates in both clear and cloudy conditions. The shortwave component of the surface flux is normalized to the daily mean in a manner analogous the TOA flux. After this normalization, the atmospheric column radiative fluxes are derived as the difference of the reported TOA flux from the surface flux. The sign convention for the fluxes are positive upward at the TOA, positive downward at the surface, and positive in for the atmospheric column. Finally, the net flux at the TOA, SFC, and ATM is derived as the sum of the shortwave and the longwave fluxes.

It is important to emphasize that the normalization of the shortwave fluxes is an approximation that does not take into account variations in albedo with solar zenith angle. This introduces a low bias in the estimated daily mean reflected shortwave flux. An additional bias that affects all of the observed parameters results from the sun-synchronous orbit of the A-train that precludes sampling of the diurnal cycle of any of the satellite based observables. Nonetheless, the majority of this paper deals with relationships between anomalies from the mean and timescales longer than the diurnal cycle. The results should therefore be largely insensitive to these sources of bias.

4.3 Methodology

4.3.1 Cluster analysis

A K-Means clustering analysis [*Anderberg, 1973*] is employed on the MODIS level 3 International Satellite Cloud Climatology Project [*Schiffer and Rossow, 1983*] (ISCCP)-like τ -CTP histograms following the methodology of *Jakob et al.* [2003]. Recent research using ISCCP data demonstrates that this clustering approach is able to identify cloud clusters that are associated with unique radiative, thermodynamic and dynamic

atmospheric conditions [Jakob *et al.*, 2005] as well as differentiable precipitation and latent heating characteristics [Jakob *et al.*, 2008]. These traits make a cloud clustering approach a useful construct within which to examine the relationships between tropical precipitation and radiation fields.

The ISCCP-like joint histograms contain counts of the co-occurrence of various combinations of cloud optical depth and cloud top pressure within each one-degree region. These histograms are normalized by the cloud fraction so that the sum of the histogram values varies between 0 (completely clear) and 1 (completely overcast). For the purposes of this study, the tropical oceanic region (30N-30S) is isolated for the clustering analysis. Six cloud clusters are selected that satisfy the objective criterion of Rossow *et al.* [2005].

Figure 4.1 shows the six cloud clusters identified by the algorithm while Figure 4.2 provides the spatial distribution of the relative frequency of occurrence of the clusters. These six clusters largely correspond to those found by Rossow *et al.* (2005) using ISCCP data for a similar region. From a radiation budget point of view it is useful to further group these six clusters into three broad categories: (1) Shallow overcast clouds, (2) Convectively suppressed and clear, and (3) Deep convection and cirrus. Three of the clusters are identified with mostly cloudy skies and a lack of penetrating deep convection. These clusters are labeled as stratocumulus, shallow cumulus, and mid-level convective. Taken together these three clusters dominate the eastern tropical ocean basins with a relative frequency of occurrence of 20.3%. The overcast deep convection and cirrus clusters dominate the west pacific warm pool as well as the inter-tropical convergence zone (ITCZ), together occupying 24.2% of the tropical oceanic area. Importantly, the mostly clear sky regime dominates the majority of the tropical oceans with a frequency of occurrence of 55.5%. The spatial distribution of these regimes is broadly consistent with a tropical circulation composed of a meridional Hadley circulation and a zonal Walker circulation.

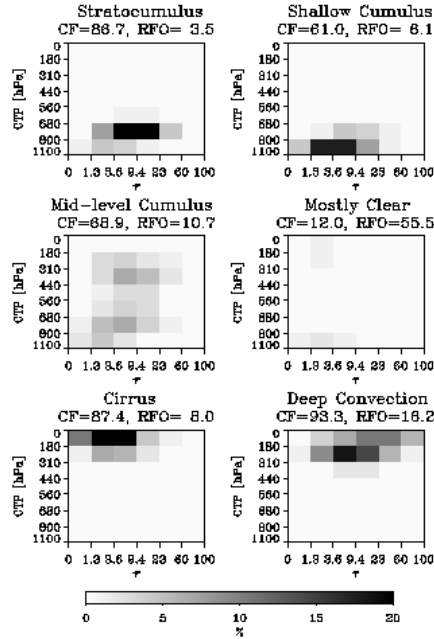


Figure 4.1: The six tropical oceanic cloud clusters. The cloud fraction (CF) and the relative frequency of occurrence (RFO) are provided in percent.

4.3.2 Constructing the tropical mean anomaly time series:

In this work, averages over the entire tropical oceanic region are examined following the example of *Hartmann and Michaelson* [1993]. This region can be said to include the ascending and descending branches of the Hadley and Walker circulations and thus provides a better indications of tropics-wide relationships than those derived locally. This approach further allows examination of the relationships between precipitation and radiation within each cluster as well as how the clusters interplay with each other. To this end anomaly time series of the daily tropical oceanic mean values of several parameters are examined. The anomaly time series of each parameter is constructed as follows:

- 1 All valid daily oceanic data from 30S-30N are area weighted and averaged to construct a five-year (2003-2007) time series. Time series of each variable are constructed for the area occupied by each of the six cloud clusters as well as

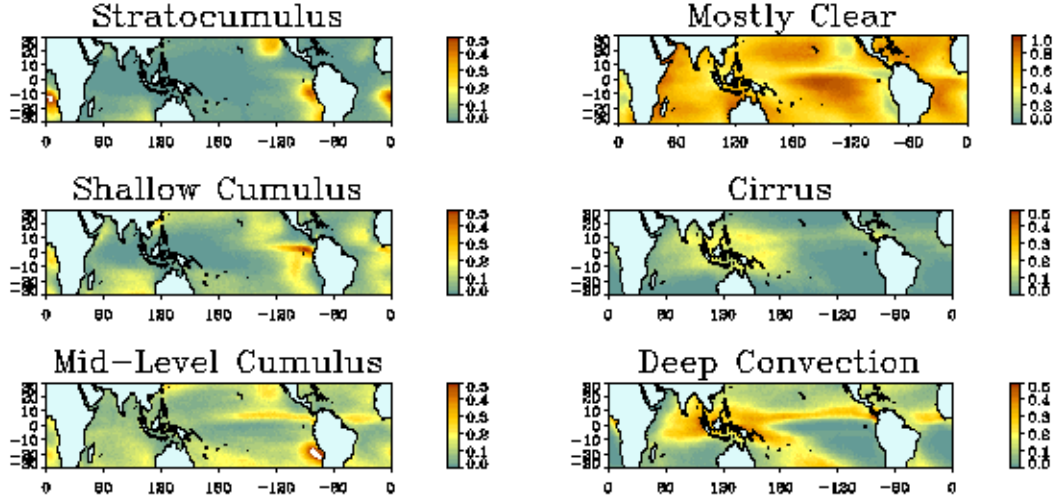


Figure 4.2: Mean geographical distribution of the frequency of occurrence of each of the six tropical oceanic cloud clusters. Note that the color scale differs for the mostly clear regime.

the entire tropical oceanic region.

- 2 Missing days are interpolated using linear relationships derived from the surrounding 21 days.
- 3 The seasonal cycle is removed by differencing the daily values from the monthly mean value.
- 4 The effects of the El Nino Southern Oscillation (ENSO) are removed by regressing the time series against the Multivariate ENSO Index (MEI), [Wolter and Timlin, 1993] and then subtracting the linear regression from the time series.
- 5 Any additional low frequency variability is removed by subtracting the 120 day running mean from the time series.

An example of the filtering process (Steps 3-5) is illustrated in Figure 4.3 for the case of the integrated atmospheric mean column temperature. For each variable the residual time series resulting from this process is a highpass filtered anomaly time series. Such a time series is useful for examining relationships on daily to intra-seasonal timescales.

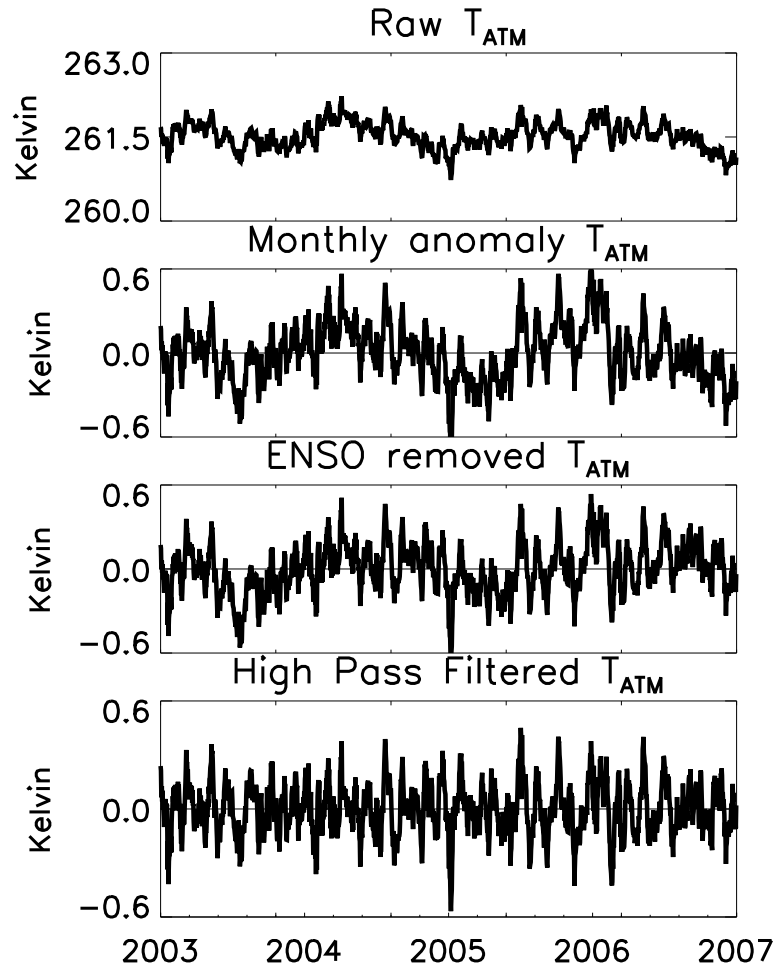


Figure 4.3: An example of the filtering process for the specific case of the tropical oceanic column mean temperature (T_{ATM}). The filtering process is described in the text.

4.4 Results and Discussion

4.4.1 Radiation budget

The mean radiation budget and latent heating of the six clusters is provided for reference in Table 4.1. It is important to note that this radiation budget is subject to the sampling biases inherent in A-train observations that are described in Section 4.2. The tropical region, as defined here, receives 401 Wm^{-2} of solar radiation at the TOA. This solar input is largely but not entirely balanced by 71 Wm^{-2} of reflected

Table 4.1: The daily mean tropical oceanic energy budget [Wm^{-2}] for the various cloud clusters. The top of the atmosphere (TOA) is defined positive up, the surface (SFC) is defined positive down, and the atmospheric column (ATM) is defined positive in. F_o is the incoming solar flux. Latent heating (LH) is derived from the AMSR-E precipitation rates.

	TOA				SFC			ATM			
	F_o	SW	LW	NET	SW	LW	NET	SW	LW	NET	LH
Stratocumulus	-395 ± 32	111 ± 7	271 ± 3	-12 ± 28	202 ± 21	-29 ± 4	174 ± 21	81 ± 7	-242 ± 5	-161 ± 9	17 ± 10
Shallow Convection	-398 ± 26	79 ± 4	276 ± 2	-43 ± 23	238 ± 18	-41 ± 3	197 ± 17	82 ± 5	-235 ± 3	-153 ± 7	15 ± 4
Mid-Level Convection	-395 ± 24	103 ± 7	246 ± 3	-47 ± 20	208 ± 15	-39 ± 2	169 ± 15	84 ± 5	-207 ± 4	-123 ± 7	121 ± 25
Mostly Clear	-399 ± 19	43 ± 2	280 ± 2	-76 ± 18	273 ± 14	-67 ± 2	206 ± 14	83 ± 4	-214 ± 2	-131 ± 4	11 ± 3
Deep Convective	-412 ± 15	156 ± 8	175 ± 4	-80 ± 12	162 ± 10	-35 ± 2	127 ± 9	94 ± 4	-140 ± 4	-47 ± 6	374 ± 60
Cirrus	-419 ± 13	87 ± 4	201 ± 4	-131 ± 12	241 ± 10	-44 ± 3	197 ± 11	91 ± 3	-156 ± 4	-66 ± 5	35 ± 11
Total Tropics	-401 ± 19	71 ± 4	259 ± 2	-70 ± 17	245 ± 13	-55 ± 2	190 ± 12	84 ± 4	-240 ± 2	-120 ± 5	69 ± 9

shortwave radiation and 259 Wm^{-2} of emitted longwave radiation making the tropical oceans a region of net heating of the Earth-atmosphere system. Most importantly, the inter-cluster differences demonstrate that the amount of reflected shortwave is largely determined by the cloud fraction whereas the temperature of the emitting cloud largely governs the emitted longwave radiation. Recall that the cloud clusters have different spatial distributions (Figure 4.2) thus explaining the different values of F_o for each cluster.

The TOA energy budget implies a heating of 70 Wm^{-2} to the ocean-atmosphere system, however, the partitioning of this heating between the atmosphere and the surface is far from uniform. The surface receives 245 Wm^{-2} of shortwave and loses only 55 Wm^{-2} in the longwave giving a large net radiative flux into the ocean of 190 Wm^{-2} . The inter-cluster differences in these quantities are small and primarily associated with cloud fraction and rather independent of cloud top height consistent

with the dominance of the shortwave term. The atmospheric column receives 84 Wm^{-2} of shortwave heating while cooling in the longwave at a rate of 204 Wm^{-2} giving a net cooling of the column of 120 Wm^{-2} . The inter-cluster differences in the atmospheric column heating are dominated by the longwave effect of varying emission temperatures of clouds.

Also shown in Table 4.1 are the statistics for atmospheric column latent heating. There is large variability in the column latent heating both between the various clusters and within each cluster. The tropical oceanic net column latent heating is 69 Wm^{-2} (equivalent to $P = 2.64 \text{ mm/day}$), which is dominated by mid-level and deep convection, implying that variability in tropical mean precipitation will be dominated by variability in these clusters.

Note that the sum of the radiative and latent heating terms implies a net deficit of 51 Wm^{-2} in the atmospheric column that must be balanced by surface sensible heating and atmospheric transport. The sensible heating is on the order of 10 Wm^{-2} [*Hartmann and Michaelson, 1993*] for this region. The remaining energy deficit must be balanced by warm air advection from land areas. The atmospheric column radiative-convective energy budget derived here no doubt has a substantial uncertainty. Note however that an estimate of the tropical oceanic energy budget for the same region provided by the Hydrologic and Earth's Radiation Budget (HERB) algorithm [*L'Ecuyer, 2009*] derived from entirely independent Tropical Rainfall Measurement Mission (TRMM) observations [*Kummerow, 1998*] suggests that the column radiative cooling estimated to be 120 Wm^{-2} in the present study may in fact be as large as 136 Wm^{-2} .

4.4.2 Relationship of tropical mean radiation budget to precipitation

Given the variability of the radiative fluxes shown in Table 4.1 within each cluster it is of some utility to identify variables that may be used to explain this variability. To this end, the sensitivity of the radiative fluxes to changes in precipitation for each of the six cloud clusters are examined. To establish causal links between precipitation and radiation, cloud macrophysical properties are examined as well. These relationships are highlighted in Table 4.2, which shows the linear fit of the radiation and cloud property anomalies with the precipitation anomaly. It may generally be stated that an increase in precipitation rate is associated with increased cloudiness as shown through increased cloud fraction, larger cloud optical depths, and colder cloud top temperatures. Furthermore, these changes in cloud macrophysical structure result in increased reflectance of shortwave energy and decreased emission of longwave energy at the top of the atmosphere. The longwave effect dominates for the stratocumulus and shallow convection clusters whereas the shortwave effect dominates for all other clusters. In the tropical average the shortwave effect wins over the longwave effect providing a modest cooling effect on the Earth-atmosphere system.

An important result demonstrated in Table 4.2 is that the sensitivity of the tropical mean radiation anomalies is larger than that of any of the individual clusters. One may infer from this result that the tropical average relationships derive in part from variability in the relative frequency of occurrence of the various cloud clusters. Furthermore, the implied variability in the cluster frequency of occurrence manifests itself in an evident manner as sensitivity of the tropics wide bulk cloud macrophysical properties, defined by the cloud fraction, cloud optical depth, and cloud top temperature. In particular, it will be shown in the following sections that the tropical mean radiation anomalies are associated with the relative area of deep convective activity.

To examine the response of the atmospheric column and surface radiation, Figure

Table 4.2: The daily mean top of the atmosphere (TOA) radiative sensitivity to precipitation. Also shown is the sensitivity of cloud fraction (CF), cloud optical depth (τ_{cloud}), and cloud top temperature (CTT). The sensitivity is defined as the linear fit between the radiative anomaly with the precipitation anomaly. The anomaly time series have been created by removing the seasonal cycle, removing the linear effects of the El Niño Southern Oscillation (ENSO), and high pass filtering the data. Trends that are insignificant at the 99% level are italicized.

	$\frac{SW_{TOA}}{(\text{mm d}^{-1})}$ (W m^{-2})	$\frac{LW_{TOA}}{(\text{mm d}^{-1})}$ (W m^{-2})	$\frac{CF}{(\text{mm d}^{-1})}$	$\frac{\tau_{cloud}}{(\text{mm d}^{-1})}$	$\frac{CTT}{(\text{mm d}^{-1})}$ (K)
Stratocumulus	<i>-0.002±0.34</i>	-1.69±0.18	-0.44±0.15	0.84±0.05	-0.68±0.08
Shallow Convection	1.91±0.46	-2.46±0.27	<i>0.10±0.31</i>	0.43±0.06	-1.12±0.16
Mid-Level Convection	2.30±0.10	-1.30±0.07	0.64±0.05	0.61±0.02	-0.51±0.04
Mostly Clear	3.17±0.15	-2.94±0.26	1.26±0.11	0.78±0.02	-0.93±0.19
Deep Convective	3.85±0.47	-2.98±0.21	0.24±0.01	0.58±0.03	-0.46±0.02
Cirrus	2.14±0.05	-1.15±0.03	0.71±0.12	0.54±0.01	-1.11±0.16
Total Tropics	5.15±0.13	-3.67±0.12	2.77±0.12	0.86±0.01	-2.01±0.08

4.4 shows the mean tropical oceanic radiative anomalies plotted as a function of the mean tropical oceanic precipitation anomaly. As has already been shown, a modest net radiative cooling effect is observed at the TOA due to the tendency of the shortwave and longwave effects to cancel. A stronger cooling dominated by the shortwave effect is seen at the surface and a warming dominated by the longwave effect is seen in the atmosphere.

Most importantly, because these results apply to the entire tropical oceanic region including the ascending and descending branches of the large-scale circulations, they demonstrate a radiative-convective cloud feedback that applies tropics-wide. Increasing tropical oceanic mean precipitation rate results in increasing tropical cloudiness that acts to decrease shortwave heating at the Earth’s surface and decrease longwave cooling of the atmospheric column. In conjunction these two effects act to stabilize the atmosphere against further precipitation and provide a modest cooling of the combined Earth-atmosphere system.

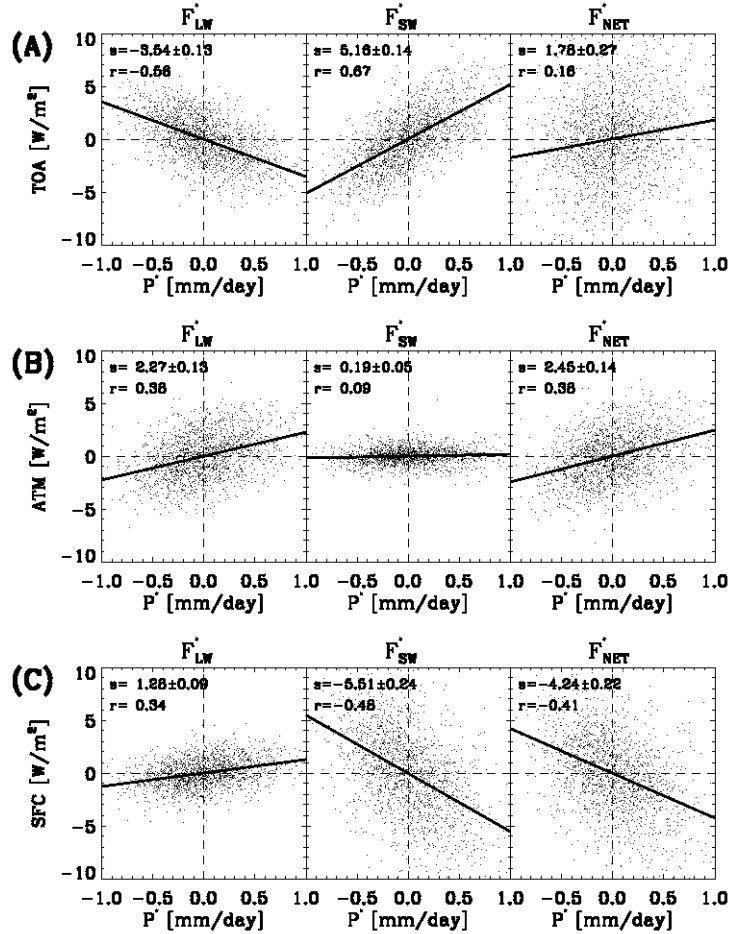


Figure 4.4: Relationships between tropical ocean mean precipitation (P') and radiative (F') anomalies. Results are broken down into shortwave (SW) and longwave (LW) components. The summary statistic (s) is the slope of the linear fit while (r) is the correlation coefficient.

It is well known that precipitation acts to stabilize the tropical atmosphere through the transfer of latent energy from the surface to the atmosphere in a manner associated with radiative-convective equilibrium. Here it has further been demonstrated that in addition to the latent heating effect, increases in tropical precipitation rate acts to establish cloud fields that result in a redistribution of radiative energy from the surface to the atmosphere causing a cooling at the surface and warming in the atmospheric column. This radiative heating is roughly 10% of the magnitude of the latent heating. Although small relative to the latent heating of precipitation, this effect

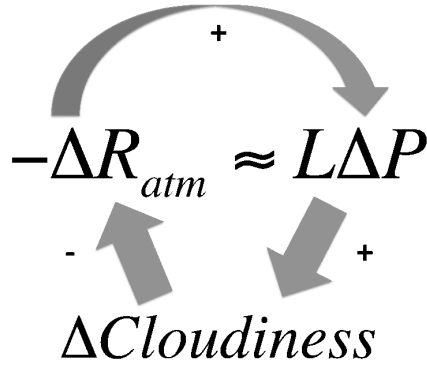


Figure 4.5: Graphical depiction of the radiative-convective cloud feedback. Perturbations to the atmospheric column radiative heating rate are approximately balanced by perturbations of the atmospheric latent heat release through precipitation. The precipitation perturbation is associated with cloudiness perturbations that act to counter the atmospheric cooling rate perturbation thus establishing the negative feedback loop.

is not insignificant as it demonstrates that precipitation acts to establish a radiation field that damps the need for further precipitation to balance the atmospheric column energy budget. Tropical precipitation therefore has a negative feedback against itself that we call the radiative-convective cloud feedback. Figure 4.5 offers a graphical depiction of this feedback. Observations [Stephens *et al.*, 2004] and cloud resolving model experiments [Fu *et al.*, 1995; Stephens *et al.*, 2008] have demonstrated that the mechanisms hypothesized here acts on local scales through the radiative effects of high level cirrus clouds. Here, it is further identified that the feedback is relevant to the large scale tropical mean. Furthermore, the specific results shown in Table 4.2 indicate that the magnitude of the feedback on the tropic-wide spatial scale is larger than the effect observed on the local scale defined by any of the individual cloud clusters.

4.4.3 Time dependent behavior (A demonstration of the feedback)

Results to this point have established a precipitating-cloud radiative feedback that acts in the large-scale tropical mean sense on the daily mean time scale. In what follows, the time evolution of these relationships are explored in an effort to demonstrate the existence of this feedback on intra-seasonal times scales. A 7-day running mean has been applied to the time series shown in this section. This has the effect of filtering out high frequency variability that to a large extent may be attributed to sampling noise. Application of this low-pass filter has the further effect of clarifying the results without fundamentally changing the conclusions that are reached. Figures 4.6-4.11 show lag-sensitivities of anomalous radiative, cloud, and thermodynamic parameters with the precipitation anomaly. For reference, the auto-correlation of the precipitation anomaly time series is also shown on each plot.

The lag-sensitivity of the shortwave and longwave TOA radiative anomalies with respect to the precipitation anomaly is shown in Figure 4.6. Because the time series has had a 7-day running mean applied, the region within 6 days of lag zero cannot be considered independent. In fact the strong positive auto-correlation of precipitation on weekly time scales primarily result from the application of the running mean. The e-folding time scale of this time series is in fact on the order of 1-2 days. More interestingly are the statistically significant ($p < 0.05$) auto-correlations in precipitation seen at lags of 10-25 days showing an indication of an oscillatory behavior in mean tropical precipitation on a 30-50 day time scale.

As has been shown in the previous section, the lag-sensitivities of the radiative anomalies demonstrate that the TOA shortwave anomaly is strongly correlated with the precipitation anomaly and the TOA longwave anomaly is anti-correlated with the precipitation anomaly. The lag-sensitivities further bring to light subtle yet important differences in the time evolution of these quantities. The shortwave anomaly

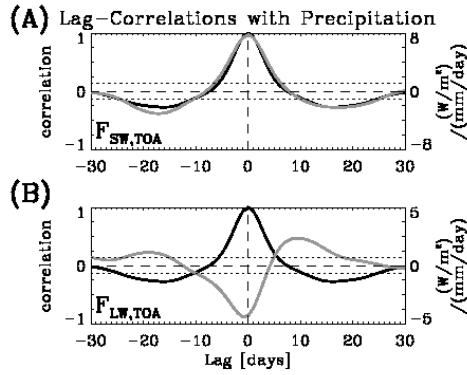


Figure 4.6: Lag-sensitivities of the tropical oceanic mean shortwave (SW) and longwave (LW) top of the atmosphere (TOA) radiative anomalies with the precipitation anomalies (gray lines). Also shown for reference is the auto-correlation of the precipitation anomaly time series (black lines). The dotted lines represent the thresholds for statistically significant autocorrelations at the 95% level. A seven-day running mean has been applied to the anomaly time series.

demonstrates a high degree of symmetry about the precipitation anomaly whereas the longwave anomaly shows some degree of asymmetry. These subtle differences are amplified in the net radiative anomalies, which are provided in Figure 4.7. The net TOA radiative anomaly, which depends on both the shortwave and longwave effects, lags the precipitation anomaly by 3 days. Furthermore, the net atmospheric anomaly, which results primarily from a longwave effect, lags the precipitation anomaly by 7 days whereas the net surface radiative anomaly, which results primarily from the shortwave effect, lags precipitation by only one day.

The above lag-sensitivities of radiation may be understood through the corresponding lag-sensitivities of the relative frequency of occurrence of the various cloud clusters shown in Figure 4.8. Tropical mean precipitation anomalies are associated with a pulsing of the deep convective and cirrus modes compensated primarily with the expansion and contraction of the clear sky mode with an amplitude near 15%. Statistically significant ($p < 0.05$) lag-sensitivities are also observed between precipitation and the three low cloud clusters that are roughly 90 degrees out of phase. Recalling

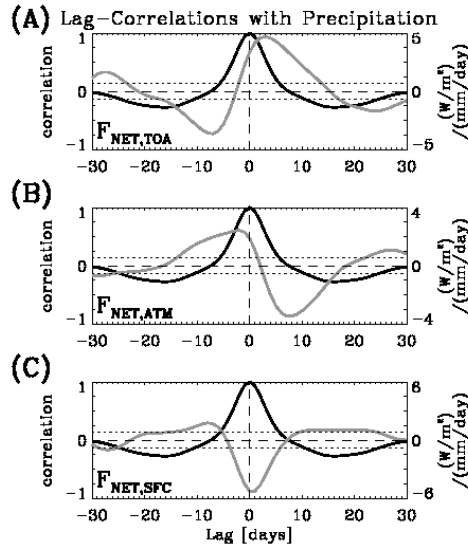


Figure 4.7: As in Figure 4.6 but for lag-sensitivities of the tropical oceanic mean net top of the atmosphere (TOA) atmospheric column (ATM) and surface (SFC) radiative anomalies with the precipitation anomalies (gray lines).

that the shortwave anomaly is primarily associated with cloud fraction whereas the longwave anomaly is associated with cloud temperature the lag-sensitivities of the cloud clusters are generally consistent with those of radiation. To highlight this point Figure 4.9 shows lag-sensitivities of CF, τ_{cloud} , and CTT. Owing to the lagged response of shallow cloud the total CF is in phase with precipitation whereas the build up of high cold clouds precedes precipitation resulting in the asymmetrical longwave sensitivity.

If the net atmospheric column radiative heating shown in Figure 4.4 is relevant to the tropical climate, its effects on the column mean temperature should be evident. To test these relationship the AIRS temperature retrievals are employed. Temperature profiles are not available from AIRS at all locations, however data coverage is remarkably complete. Furthermore, because temperature gradients above the boundary layer are weak in the tropics the available samples should provide a reasonable estimate of the atmospheric column mean temperature. From the time series of daily

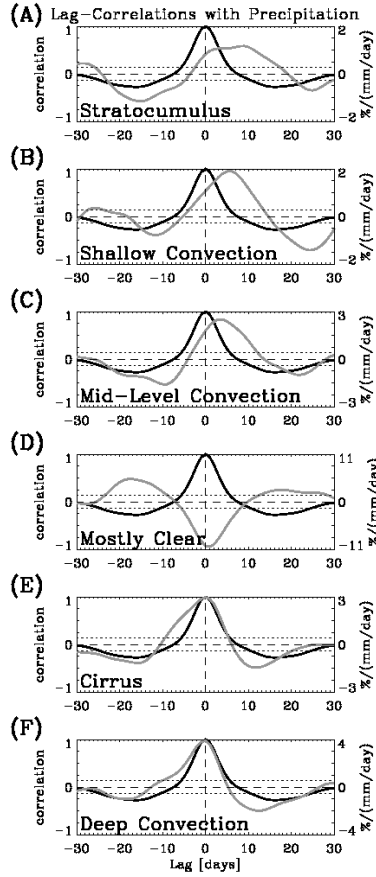


Figure 4.8: As in Figure 4.6 but for lag-sensitivities of the anomalous cluster frequency of occurrence with the precipitation anomalies (gray lines).

column mean temperature, an observed heating rate time series is derived. The latent heating anomaly time series correlates with the observed heating rate anomaly at $r = 0.39$ whereas the latent heating plus the radiative heating anomaly time series correlates with the observed heating rate anomaly at $r = 0.46$. Therefore, inclusion of the radiative heating term increases the explained variance in the observed heating anomaly by 6% over latent heating alone. The importance of the radiation anomaly to the temperature anomaly is further illustrated in Figure 4.10 which shows the lag-sensitivities of the derived atmospheric column heating rate as observed by both the microwave and the infrared AIRS algorithms. The heating rate lag-sensitivities show a similar temporal evolution to that of the atmospheric radiative heating anomalies

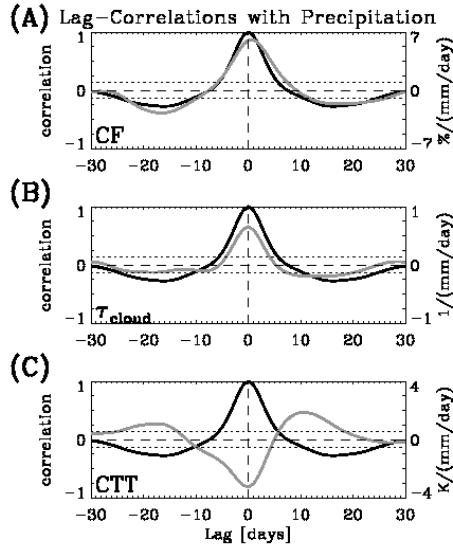


Figure 4.9: As in Figure 4.6 but for lag-sensitivities of the cloud fraction (CF), cloud optical depth (τ_{cloud}), and cloud top temperature (CTT) anomalies (gray lines).

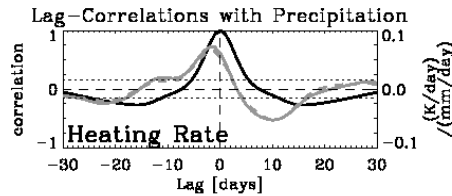


Figure 4.10: As in Figure 4.7 but for lag-sensitivities of the tropical oceanic mean net atmospheric column mean heating rate with the precipitation anomalies (gray lines). The solid/dashed gray lines represent the microwave/infrared AIRS algorithms.

shown in Figure 4.7b. The pattern of lag-sensitivities of AIRS heating rate (Figure 4.10) and CERES atmospheric radiative heating (Figure 4.7b) anomalies correlate at $r = 0.73$. Therefore, radiation alone explains 53% of the variability in the time lag of the heating anomaly time series relative to precipitation.

Figure 4.11 demonstrates that the observed heating anomalies occur primarily in the middle and upper levels. The temperature in the low levels of the atmosphere that is largely determined by surface fluxes, on the other hand, do not demonstrate significant lag-correlations with precipitation. Additionally, this figure demonstrates

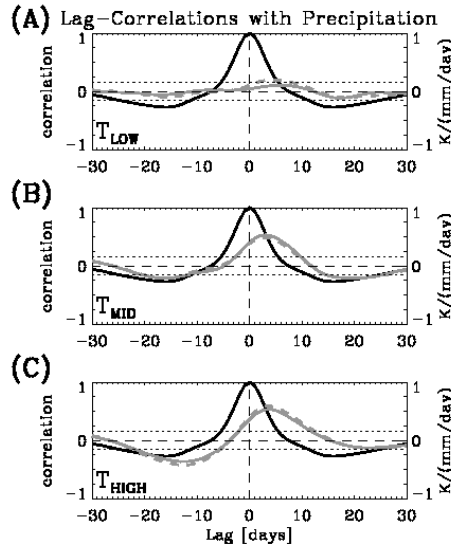


Figure 4.11: As in Figure 4.7 but for lag-sensitivities of the tropical oceanic mean net temperature anomaly with the precipitation anomalies (gray lines). The solid/dashed gray lines represent the microwave/infrared AIRS algorithms. Low is defined as the surface to 650 hPa, middle is defined as 650 hPa to 350 hPa, and high is defined as higher than 350 hPa.

that upper-level temperatures are approximately 90 degrees out of phase with precipitation consistent with anomalously unstable atmospheres preceding precipitation with anomalously stable atmospheres following precipitation.

Taken together, Figures 4.6-4.11 paint a picture of an oscillating system in which anomalies in tropical mean precipitation are dominated by oscillations in the frequency of occurrence of deep convection that in turn are associated with variability in tropical mean cloudiness, radiation and stability. Positive precipitation anomalies appear to be preceded by colder than normal middle and upper level temperatures and followed by anomalously warm temperatures consistent with the observed radiative and latent heating. Moreover, the coherent relationships between precipitation, cloud, radiation, and temperature fields on intra-seasonal timescales demonstrate the action of the radiative-convective cloud feedback implied in the previous section on these timescales within the tropical atmosphere. The feedback acts through a coupling of

tropical mean precipitation with the column radiative heating that is primarily associated with an expansion and contraction of the relative area of deep convective activity.

4.4.4 Relationship to the Madden-Julian oscillation

The lag-correlations shown in the previous section suggest coherent oscillatory behavior in precipitation, cloud, radiation, and thermodynamic variables. The precipitation auto-correlation indicates that this oscillation occurs on 30-50 day time scales. This timescale is suggestive of the Madden-Julian oscillation (MJO) [*Madden and Julian, 1971; Madden and Julian, 1972*], which is the dominant mode of intra-seasonal variability in the tropical atmosphere [*Weickman et al., 1985; Zhang, 2005*]. Coherent relationships, similar to those presented in this work, have been observed between precipitation, radiative, and thermodynamic properties of the atmosphere on local scales for MJO events [*Lin and Mapes, 2004; Stephens et al., 2004*]. However, the MJO describes propagating convective features composed of both active and suppressed regions so it is not immediately apparent that the temporal signature of this oscillation should be visible on the larger scale of the tropical mean.

The Real-time Multivariate MJO (RMM) indices of *Wheeler and Hendon [2004]* are used to explore the relationships between the MJO and tropical mean precipitation anomaly. The two RMM indices, RMM1 and RMM2, are derived from an empirical orthogonal functions (EOF) analysis of near equatorially averaged 850 and 200 hPa zonal wind and the outgoing longwave radiation (OLR) fields. Together RMM1 and RMM2 have been shown to capture the complex spatio-temporal signal of the MJO in a concise form, therefore providing a useful metric with which to examine relationships between variability in the MJO and other atmospheric phenomena.

A cross-spectral analysis is employed [*Madden and Julian, 1971; Madden and Julian, 1972*] to test the hypothesis that tropical precipitation and radiation anomalies

oscillate in a coherent fashion with the MJO. Figure 4.12 shows that the power spectra of the precipitation anomalies (P'), radiation anomalies ($F'_{SW,TOA}$, $F'_{LW,TOA}$), RMM1, and RMM2 demonstrate significant variability between 30 and 50 day time scales. The precipitation and radiation anomalies also have variability on shorter time scales unassociated with MJO activity. While all of these variables demonstrate variability on intra-seasonal time scales it is necessary to calculate the co-spectra of precipitation and radiation with RMM1 and RMM2 to demonstrate that the oscillations are related to each other. This analysis is highlighted in Figure 4.13. This figure further demonstrates that much of the significant variability in precipitation and radiation on 30-50 day time scales is coherent with variability in both RMM1 and RMM2. Precipitation and shortwave radiation oscillate in phase with RMM1 whereas longwave radiation is 180 degrees out of phase on the 30-50 day time scales broadly corroborating the results of the previous section.

4.4.5 Spatial patterns of the anomalies

A composite analysis is employed to show the spatial patterns of precipitation, cloud, and radiative parameters associated with positive and negative precipitation anomalies. The data are composited into positive/negative anomalous days that exceed $+/-$ one standard deviation of the mean precipitation anomaly. Days with precipitation anomalies within one standard deviation are not considered in the composite analysis. After screening out days in which precipitation has been interpolated, 266 positive anomaly days and 264 negative anomaly days remain for analysis.

Figure 4.14 shows the composite precipitation, TOA radiative, and cloud property anomalies associated with the positive anomaly days. Negative anomaly days are not shown as they lead to identical conclusions. The precipitation anomaly map shows a similar spatial pattern to the climatological precipitation map emphasizing the inter-tropical convergence zone and West Pacific warm pool. This pattern suggests that

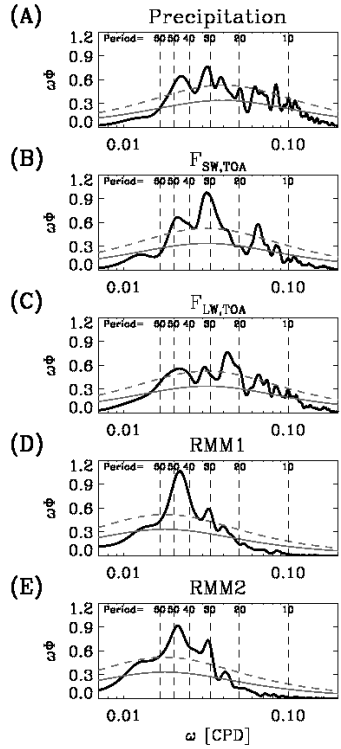


Figure 4.12: The power spectra (Φ) of (A) Precipitation (B) TOA shortwave (C) TOA longwave (D) RMM1 and (E) RMM2. Φ is plotted as a function of frequency (ω) in cycles per day (CPD). The area under the curve has been normalized to unity. A 21 point tapered running mean has been applied to all spectra to increase the number of degrees of freedom for significance testing. The solid gray line is the red-noise spectrum computed from the e-folding auto-correlation timescale of each time series while the dashed gray line represents the level of spectral power that is needed to reach the 95% confidence level for significance. The vertical dashed lines show periods from 10-60 days.

anomalous tropical precipitation results from modulation of the deep convection and thus the large-scale tropical circulations. Furthermore, the composite TOA radiative anomaly and cloud property maps are spatially well correlated with the precipitation anomalies demonstrating that the areas of locally enhanced convection are associated with the expected local cloud and radiative anomalies.

The results of this section show general consistency with the results of previous sections. Taken together the composite maps demonstrate a pulsation of the tropical area associated with deep convective activity that manifests itself in a pulsation of

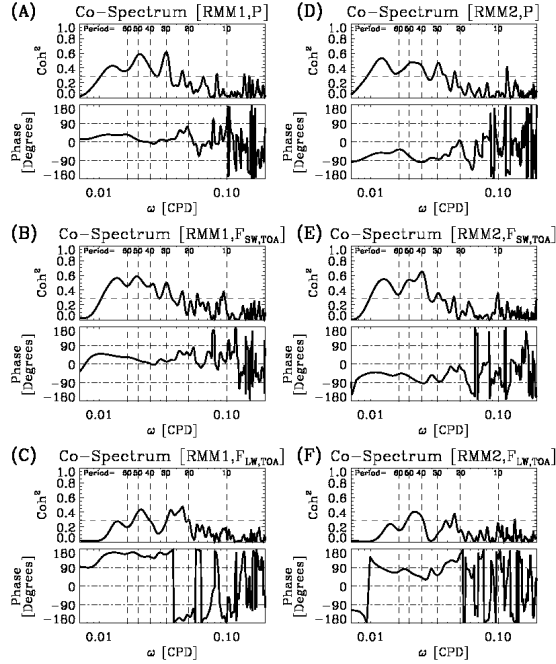


Figure 4.13: The Co-Spectra of RMM1 (A-C) and RMM2 (D-F) with the anomalous precipitation (P) TOA shortwave ($F_{SW,TOA}$), and TOA longwave ($F_{LW,TOA}$). As in Figure 4.12, a 21 point tapered running mean has been applied to the spectra. Coherence squared (Coh^2) values that exceed the threshold drawn by the horizontal dashed (0.283) line exceed the 95% confidence level for significance. The vertical dashed lines show periods from 10-60 days. Note that only frequencies bands in which both the power spectra (Φ) (shown in Figure 4.12) and the Coh^2 are statistically significant should be considered significant. This occurs for all parameters near 30 and 50 day periods.

the tropical cloud fraction, cloud optical depth and cloud top temperature. The expansion and contraction of the tropical deep convective area is largely balanced by variability in the tropical clear sky area. This variability in tropical cloudiness in turn causes commensurate variability in the TOA radiative properties. Finally, it is noted that the spatial patterns found in Figure 4.14 suggest that the variability in tropical precipitation and radiation is related to variations in the strength of the large-scale tropical circulations.

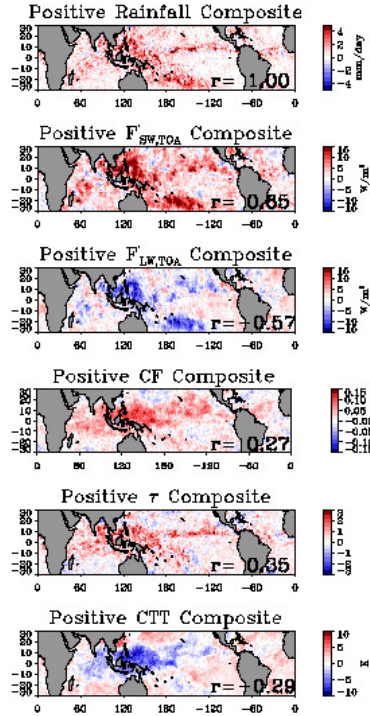


Figure 4.14: Geographical distribution of the precipitation, radiation, and cloud parameters for the positive rainfall composite days (defined as days when anomalous rainfall exceeds one standard deviation of the mean). The spatial correlation coefficient (r) of each composite map with the precipitation composite is provided.

4.4.6 Extension of the feedback to a perturbed climate

The feedback presented here may potentially have important ramifications on predictions of the global hydrologic cycle in a global warming scenario. Global climate models predict an enhancement of the radiative cooling rate of the atmosphere that is largely balanced by an increase in the global precipitation rate resulting in an enhancement of the global water cycle on the order of 2-3 %/K [Allen and Ingram, 2002; Held and Soden, 2006; Stephens and Ellis, 2008]. The results presented here suggest that the tropical atmosphere tends to respond to increased precipitation by establishing cloud fields that act to reduce the rate of atmospheric radiative cooling. Assuming that the linear relationships derived here (Figure 4.4) for the present climate are applicable to a perturbed climate, this negative feedback would act to counter an

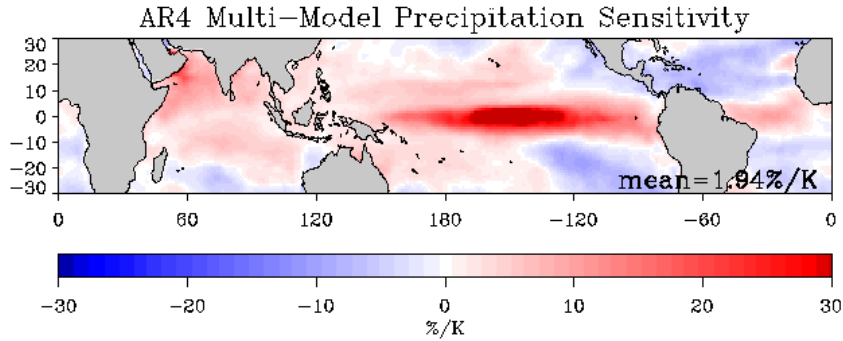


Figure 4.15: The multi-model mean precipitation sensitivity of the IPCC AR4 models for the 1% to 2xCO₂ runs. This sensitivity is defined as the percentage change in precipitation rate for a 1 Kelvin change in global mean surface temperature. The mean over the tropical (30S-30N) oceans is 1.94 %/K.

enhancement of the global hydrologic cycle by 10%. In fact, such radiative-convective cloud feedbacks have been observed in global climate model experiments [Fowler and Randall, 1994]. In what follows an estimate of the strength of this potential feedback is provided using the observed relationships found in this work.

As in the *Stephens and Ellis* [2008] work, the IPCC AR4 (Inter-governmental Panel on Climate Change, Fourth Assessment Report) 1% to 2xCO₂ climate model runs are used to estimate the magnitude of the sensitivity of the hydrologic cycle to global mean surface temperature. Again following the aforementioned work, the sensitivity is calculated as the difference of years 1-10 from years 61-70 in order to mitigate the effects of year-to-year variability. See that work for further details on the model runs considered here. Figure 4.15 shows the spatial pattern of the sensitivity for the tropical oceanic domain considered in this research. The area weighted domain average sensitivity is 1.94 %/K.

To demonstrate the rough order of magnitude of this negative feedback the linear relationships shown in Figure 4.4 are used in conjunction with Equation 4.3 to estimate the strength of this radiative-convective cloud feedback on the hydrologic cycle. An increase of 1.9 %/K of the hydrologic cycle implies that the tropical oceanic mean

precipitation rate of 2.64 mm/day increases by $P' = 0.051 \text{ mmd}^{-1}\text{K}^{-1}$. According to Equation 4.3, this increase in precipitation implies a commensurate increase in the atmospheric heating rate of $R' = 1.34 \text{ Wm}^{-2}\text{K}^{-1}$. The sensitivities shown in Figure 4.4, however indicate that increased precipitation rate is related to increased atmospheric heating through increased cloudiness. These sensitivities give the strength of the feedback as $0.13 \text{ Wm}^{-2}\text{K}^{-1}$. Comparing these two numbers gives the strength of the feedback as roughly 10% of the forcing. In addition, a modest negative feedback at the TOA and a stronger surface feedback should be observed. Using an analogous methodology to that presented above, the feedback strength is estimated as $0.09 \text{ Wm}^{-2}\text{K}^{-1}$ at the top of the atmosphere and $0.22 \text{ Wm}^{-2}\text{K}^{-1}$ at the surface. Here, it is again emphasized that these estimates are premised on the assumption that the linearity of the relationships derived for the current climate are applicable to a future perturbed climate and therefore must be considered somewhat speculative in nature. Furthermore, the mechanisms presented here represent only one potential cloud feedback and ignore sensible feedbacks that tend to be non-zero in climate models [*Stephens and Ellis, 2008*].

4.4.7 Model comparison

Climate models have been shown to have a cloud feedback analogous to the one demonstrated here. It is therefore of interest to compare the relationships between precipitation and radiation anomalies in models with those observed in this work. This comparison is performed using daily output from the AR4 climate of the twentieth century (20C3M) runs for the model years 1991-2000. Unfortunately, model data output is not archived for several key parameters on daily times scales. These parameters include the shortwave component of the TOA radiation and cloud fields. Nonetheless a useful comparison can be made between a subset of the observed trends shown in Figure 4.4 and the model output.

Table 4.3: Trends of the tropical average radiation anomalies with the tropical average precipitation rate $[(\text{Wm}^{-2})/(\text{mmd}^{-1})]$ from the CERES/AMSR-E observations and several selected climate models from the climate of the twentieth century model runs. Note that the TOA shortwave radiation parameters are not archived on the daily timescale for these model runs.

Model Name	LW _{TOA}	LW _{ATM}	LW _{SFC}	SW _{SFC}	NET _{SFC}
CERES/AMSR-E Observations	-3.54 ± 0.13	2.27 ± 0.13	1.28 ± 0.09	-5.51 ± 0.24	-4.24 ± 0.22
BCCR-BCM2.0, Norway	-2.28	1.07	1.21	-7.14	-5.93
CGCM3.1(T47), Canada	-2.61	2.45	0.15	-7.02	-6.87
CGCM3.1(T63), Canada	-2.84	2.69	0.15	-6.76	-6.61
CNRM-CM3, France	-1.70	1.21	0.48	-5.51	-5.03
CSIRO-Mk3.0, Australia	-0.45	-0.02	0.47	-6.33	-5.86
ECHAM5/MPI-OM, Germany	-2.96	2.18	0.78	-5.05	-4.27
GFDL-CM2.0, USA	-2.97	2.29	0.68	-6.97	-6.29
GFDL-CM2.1, USA	-3.36	2.44	0.91	-6.52	-5.60
GISS-AOM, USA	-3.40	1.21	2.20	-12.32	-10.13
MIROC3.2(hires), Japan	-3.83	2.48	1.35	-7.30	-5.94
MIROC3.2(medres), Japan	-4.41	3.35	1.06	-6.44	-5.38
MRI-CGCM2.3.2, Japan	-2.74	2.39	0.35	-7.31	-6.96
Inter-Model Mean	-2.80 ± 1.02	1.98 ± 0.92	0.81 ± 0.58	-7.06 ± 1.80	-6.24 ± 1.45

Results of this comparison are shown in Figure 4.16 and Table 4.3. The models generally show similar relationships to the observations. The only model trend that differs in sign from the observation is the extremely weak negative trend of longwave atmospheric flux in the CSIRO model. Likewise, all the observational relationships except that of the net surface flux are within the one standard deviation uncertainty estimates of the inter-model means.

Despite the generally good agreement, notable biases do exist between the models and the observations. In the longwave, the trends at the TOA and the surface are weaker in the model than in the observations leading to a cancellation of bias terms in the atmospheric column longwave heating anomaly. This fortuitous cancellation of errors results in the atmospheric column longwave anomaly trends demonstrating the least bias relative to the observations. Only the surface component of the shortwave

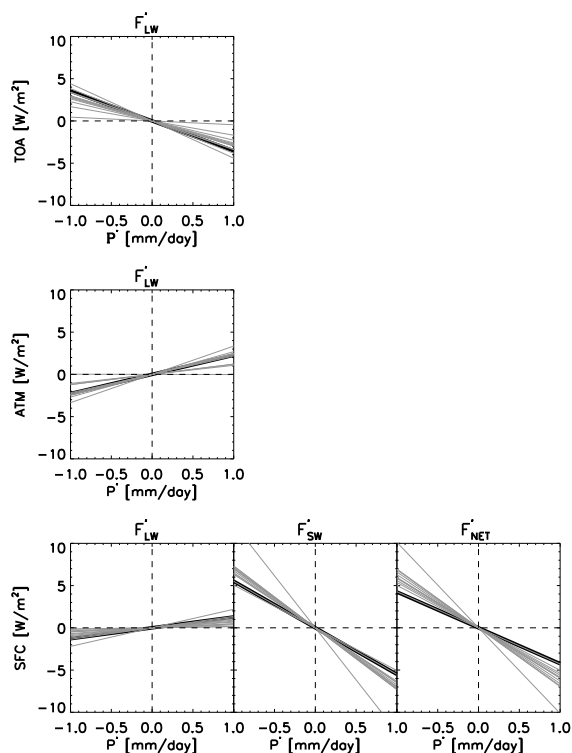


Figure 4.16: Comparison of the IPCC 20C3M daily model output with the observed relationships. Note that the TOA shortwave output is not available from the models on the daily time scale.

anomaly is available from the models. The models overestimate the observations of this relationship by $1.55 \text{ (Wm}^{-2}\text{)/(mmd}^{-1}\text{)}$. Because the surface component of the net anomaly is dominated by the shortwave component, this bias carries through to the net surface anomaly as well.

Due to the lack of cloud parameters in the climate model output it is difficult to determine the exact source of the biases between the models and the observations, however some speculative explanations may be offered. As was mentioned in Section 4.2 the lack of diurnal sampling of the observations may bias the shortwave component of the radiation anomalies towards low values of reflection (high values of transmission) as large zenith angles that have higher values of albedo are not sam-

pled. This would cause a low bias in the magnitudes of the observed relationships between the shortwave radiation and the precipitation. Both precipitation and outgoing longwave radiation have diurnal signals so it is possible that the diurnal bias in the observations affects these trends as well although it is less clear than in the case of the shortwave. An alternative explanation for these discrepancies would be that the models underestimate the magnitude of the relationships between cloud cover and precipitation or possibly cloud height and precipitation. Both of these parameters would be affected by the convective parameterizations in these models that govern the quantity of detrained high level cirrus clouds. Without additional model output it is impossible to say which combination of the above factors leads to the biases observed here.

4.5 Summary

Five years of remote observations from several sensors onboard NASA's A-train constellation of satellites are examined to identify relationships between the tropical oceanic mean precipitation anomaly and radiation anomalies. Tropics-wide averages are employed to examine these relationships on a spatial scale including both the ascending and descending branches of the Hadley and Walker circulations. The tropical oceanic precipitation anomaly is well correlated with the radiative anomaly at the top of the atmosphere, the surface, and within the atmospheric column. At the top of the atmosphere the shortwave and longwave component tend to cancel each other leaving a modest cooling effect. At the surface a stronger shortwave cooling effect is observed and in the atmosphere a longwave heating effect is evident. It is identified that these relationships derive from an increase in the relative area of tropical high cold clouds with increasing precipitation. Commensurate with the expansion of deep-convective area is a contraction of the clear sky area. Evidence is presented that

these relationships are related to a modulation in the strength of the large-scale tropical overturning circulations. The mechanism is identified as a radiative-convective cloud feedback wherein tropical convection tends to produce cloud fields that cause a reduction of the atmospheric cooling rate and a commensurate warming of the atmospheric column. The radiative warming anomaly is roughly 10% of the latent heating anomaly. The feedback is demonstrated to act in the tropical atmosphere on 30 to 50 day timescales that are related to activity of the Madden-Julian oscillation.

The shortwave component of the feedback is suggestive of the thermostat hypothesis [*Ramanathan and Collins, 1991*] that is associated with changes in cloud macrophysical properties. Within the atmospheric column the feedback is reminiscent of the global radiative-convective feedback described by *Fowler and Randall [1994]* that acts to stabilize the atmosphere through increased high cloudiness associated with convection resulting in decreased atmospheric cooling rates. Thus it is shown that the weak relationships between precipitation and net radiation at the TOA due to the near cancellation of the shortwave and longwave effects is manifest as a radiative redistribution of energy from the surface to the atmosphere which would act to stabilize the tropical atmosphere against further precipitation. This mechanism is supportive of the radiative-convective elements of the humidistat feedback hypothesized by *Stephens et al., [2004]* which was demonstrated to act on local spatial scales relevant to the Madden-Julian oscillation. Importantly, the present study demonstrates that these mechanisms are applicable on the tropical mean spatial scale through a modulation of the area of tropical high cloudiness, demonstrating that the feedback is applicable on a tropics-wide scale more directly applicable to global climate.

An argument is presented that this radiative-convective cloud feedback may act to limit the enhancement of the hydrological cycle predicted in climate model simulations by reducing the rate of tropical atmospheric cooling thus reducing the need for increased latent heating of the atmosphere. This argument is premised on the

assumption that the linearity of the relationships quantified in this work is applicable to a perturbed climate. It is estimated that this feedback would act under a global warming scenario to reduce the expected increase in precipitation by 10% while constituting a potential feedback of $0.09 \text{ Wm}^{-2}\text{K}^{-1}$ at the top of the atmosphere and $0.22 \text{ Wm}^{-2}\text{K}^{-1}$ at the surface within the tropical oceanic region.

Chapter 5

Summary of Dissertation

Observations from five instruments flying in NASA's A-train constellation of satellites are employed to explore relationships between aerosol, clouds and precipitation with a focus on the Earth's radiation budget. The particular instruments used included MODIS, AMSR-E, AIRS, CERES, and CloudSat. Together this suite of instrumentation offers a unique view of the radiative, hydrological, and thermodynamic structure of the atmosphere. The observations are applied to two focused research questions. The first focused study examines the global relationships between aerosol burden and the liquid water budget of clouds and the second area of study explores relationships between precipitation and radiation in the tropical atmosphere with an emphasis on the concept of radiative-convective equilibrium.

5.1 Aerosol indirect effects

The A-train observations are used to analyze aerosol indirect effects in warm clouds over the global oceans. The focus of the study is on the liquid water budget of clouds. Specifically, this section of the dissertation addresses the question as to whether aerosol is associated with increased or decreased liquid water path. A key element of the study is the discrimination between precipitating and non-precipitating clouds using observations from the CloudSat CPR. The ability to sort the data into precipitating and non-precipitating clouds permitted the identification of two contrasting

regimes depending on the relative dominance of dry air entrainment effects or coalescence suppression effects. The data suggests that the former effect dominates the water path response of non-precipitating clouds while the latter effect dominates for precipitating clouds. These data therefore provide some observational support of the non-monotonic responses of LWP seen in the modeling results of *Jiang and Feingold* [2006] and *Wood* [2007]. The addition of the independent observations from CERES furthermore confirm that the LWP response is evident in the behavior of the cloud albedo with aerosol.

The result indicate that non-precipitating clouds tend to suffer decreases in cloud water path with increasing aerosol. The magnitude of this relationship increases with decreasing static stability suggesting that shallow cumulus clouds are more susceptible to this effect than are stratocumulus clouds. These results may invalidate the constant LWP assumption commonly invoked in explanation of the first indirect effect. In addition to the LWP relationships, non-precipitating clouds in all thermodynamic regimes show decreases of similar magnitude in cloud effective radius with aerosol. The combination of consistent decreases in cloud radius and variable decreases in LWP are evident in the trends of cloud albedo with aerosol.

In sharp contrast with non-precipitating clouds, the transitional and precipitating clouds show strong increases in LWP with increasing aerosol. A decrease in cloud effective radius with aerosol of a similar magnitude to that observed in non-precipitating cloud is also evident in these clouds. The trends of albedo with aerosol of these clouds highlights the dominance of the water path response over the microphysical response in determining the albedo. These results are suggestive of an inhibited coalescence process resulting in greater amounts of cloud condensate and a delay in precipitation onset. Further evidence for these mechanisms are presented in the decreasing trend in cloud radar reflectivity factor and the probability of precipitation occurrence that were gleaned from the CPR. A specific analysis of the probability of precipita-

tion shows that the precipitation occurrence is decreased by as much as 10% in high aerosol regimes relative to low aerosol.

The observation that the albedo response of clouds depends markedly on the LTSS as well as the presence of precipitation guided the calculation of the global indirect albedo sensitivity (IAS) as a function of regimes that were defined by these parameters. Based on the seasonal distributions of the regimes, liquid cloud cover, and insolation the IAS was calculated to be $-0.42 \text{ Wm}^{-2} \pm 0.38 \text{ Wm}^{-2}$. Twenty five percent of this value is found to result from precipitating clouds despite the fact that only 8% of the warm clouds in the study were identified as precipitating. The analysis identifies that areas of substantial stratiform cloudiness on the eastern edges of the subtropical ocean basins and the mid-latitude storm tracks are primarily susceptible to first indirect effects whereas tropical regions associated with shallow cumulus are more susceptible to precipitation suppression effects. An assumption of the anthropogenic aerosol fraction is made that provides an estimate of the indirect albedo forcing (IAF) of $-0.13 \text{ Wm}^{-2} \pm 0.14 \text{ Wm}^{-2}$, which is significantly lower than previous estimates offered by climate models or observations that do not control for meteorological conditions. This suggests that understanding the complicated response of liquid water path to aerosol represents a critical task in refining estimates of the IAF.

The global aerosol indirect analysis presented in this dissertation presents a number of intriguing results related to the LWP response of clouds to aerosol perturbations. A gross attempt is made to control for meteorological conditions by sorting results by LTSS and precipitation occurrence. Nonetheless, it is important to bear in mind that these results are correlative in nature and while they are supported by a limited number of theoretical modeling studies, substantial additional work is necessary to confirm that the relationships presented herein are causal in nature. This is especially true of the LWP relationships that involve a complex set of dynamical

and microphysical mechanisms. In particular, future work should focus on refining the definition of the regimes used in this work. For example a recent study by *Wood and Bretherton* [2006] suggest that the use of LTSS in extratropical regions is inappropriate and further suggest a related parameter (the estimated inversion strength) that provides a better correlation with global cloud properties. A more objective approach to defining regimes may be to apply a clustering algorithm to vertical profiles of temperature and humidity similar to the one suggested by *Jakob et al.* [2003]. Furthermore, both the temporal and spatial scale of the analysis should be reduced in an effort to limit the potential of false correlations between cloud properties and uncontrolled meteorological parameters to manifest themselves in the global scale results.

Despite the potential limitations of the work presented here and the substantial work necessary to confirm the results presented herein, these results provide some of the first observational evidence of an extremely complicated relationship between cloud LWP and ambient aerosol concentrations that has been suggested in cloud modeling studies and has been as of yet unaccounted for in climate modeling efforts to quantify aerosol indirect effects. They are therefore, highly relevant to that particular community as aerosol indirect effects represent the largest single uncertainty in the scientific understanding of the current anthropogenic radiative forcing according to the IPCC.

5.2 Tropical precipitation and radiation

The A-train data are used to examine relationships between anomalies in tropical mean (30N-30S) precipitation to cloud, radiative and thermodynamic anomalies. The use of tropic wide averages is a key aspect of the study as it demonstrates that the relationships identified have large scale climatic relevance. The results identify that

the tropical mean precipitation anomaly is well correlated with the top of the atmosphere shortwave and longwave anomalies. Furthermore the shortwave and longwave effect tend to cancel resulting a near-zero TOA radiative anomaly. This effect has been consistently demonstrated in previous studies to occur on small spatial scales, however this is the first work to identify from observations that it is relevant to the tropical mean. The near cancellation at the top of the atmosphere has led to some confusion in understanding the importance of these relationships in previous studies because the atmospheric and surface components of the radiative response has frequently been neglected. In fact, the near cancellation at the TOA of the shortwave and longwave components of the radiative anomaly is manifest as a redistribution of energy from the surface to the atmosphere resulting in a an anomalous surface cooling and an atmospheric heating. In particular it is found that the atmospheric radiative heating anomaly is nearly 10% of the latent heating anomaly.

Cloud data from MODIS are used to identify that the radiative anomalies are related to the expansion and contraction of the relative area of tropical deep convection the modulates the area of high level cloudiness. Commensurate with the expansion of the area of high clouds is a contraction of the area of clear sky. Analysis of the temporal characteristics of the data identify coherent oscillations in the various precipitation, cloud, radiative, and thermodynamic variables that are consistent with a radiative-convective cloud feedback whereby variations in precipitation acts to establish cloud fields that act to modify the tropical stability through variations in radiative cooling. The time scale of these oscillations is found to be consistent with the Madden-Julian intraseasonal oscillation. Finally, the spatial patterns of the anomalies are highly suggestive that the mechanisms presented here act to modulate the strength of the Hadley and Walker circulations.

No assertion of causality is made regarding the clear relationships between the MJO and the radiative anomalies found here. Does the MJO cause the radiative

anomalies or do the radiative fields associated with precipitation set the timescale of the MJO? The issues of the initiation and propagation speed of the MJO are currently open questions [*Benedict and Randall, 2007*], however some recent work has suggested that radiation could play a non-negligible role in the diabatic heating associated with the oscillation [*Raymond, 2001; Lee et al., 2001; Sobel and Gildor, 2003*]. One compelling response to the above question is that neither statement is entirely true. Instead radiation and convection may act as components of a complex mutually coupled oscillatory system in the tropics. Future work is necessary in developing a more complete understanding of the relationships between radiation and the MJO as well as the impacts of these relationships on the global scale circulation and climate.

The aforementioned results are identified as a radiative-convective feedback that operates in the current climate. A questionable assumption of linearity is necessary to extend these results to a perturbed climate. This assertion is certainly not true for large perturbations as increasing precipitation would eventually lead to an unrealistically cloudy tropical atmosphere. For small perturbations however the assumption of linearity may be valid and the cloud feedback would manifest itself as a reduction in the rate of increase in tropical precipitation predicted from the perturbation of the clear sky component of radiative cooling alone on the order of 10%. In light of this result, future study should be undertaken to evaluate the occurrence of the relationships identified in this work in the daily time scale output of climate models. If found to accurately depict these relationships, this would lend credence to the ability of the climate models to accurately predict the coupling between radiation, clouds and convection in a perturbed system.

References

- Ackerman, A.S., O.B. Toon, J.P. Taylor, D.W. Johnson, P.V. Hobbs, and R.J. Ferek (2000), Effects of Aerosols on Cloud Albedo: Evaluation of Twomey's Parameterization of Cloud Susceptibility Using Measurements of Ship Tracks, *J. Atmos. Sci.*, **57**, 2684-2695.
- Ackerman A.S., M.P. Kirkpatrick, D.E. Stevens, and O.B. Toon (2004), The Impact of Humidity Above Stratiform Clouds on Indirect Aerosol Climate Forcing, *Nature*, **432**, 1014-1017.
- Albrecht, B. (1999), Aerosols, Cloud Microphysics, and Fractional Cloudiness, *Science*, **245**, 1227-1230.
- Allen M. R. and W. J. Ingram, (2002), Constraints on future changes in climate and the hydrologic cycle), *Nature*, **419**, 224-231.
- Anderberg M. R. (1973), *Cluster Analysis for Applications*, Academic Press, 359 pp.
- Aumann H. H., M. T. Chahine, C. Gautier, M. D. Goldberg, E. Kalnay, L. M. McMillin, H. Revercomb, P. W. Rosenkranz, W. L. Smithand, D. H. Staelin, L. L. Strow and J. Susskind, (2003), AIRS/AMSU/HSB on the Aqua mission: Design, science objectives, data products, and processing systems, *IEEE Trans. Geosci. Remote Sens.*, **41**, 253-264.
- Benedict, J. J. and D. A. Randall (2007), Observed Characteristics of the MJO Relative to Maximum Rainfall, *J. Atmos. Sci.*, **64**, 2332-2354, doi: 10.1175/JAS3968.1.
- Bony, S., R. Colman, V. M. Kattsov, R. P. Allan, C. S. Bretherton, J.-L. Dufresne, A. Hall, S. Hallegatte, M. M. Holland, W. Ingram, D. A. Randall, B. J. Soden, G. Tselioudis, and M. J. Webb (2006), How Well Do We Understand and Evaluate Climate Change Feedback Processes?, *J. Climate*, **19**, 3445-3482. doi: 10.1175/JCLI3819.1.
- Brenguier, J.-L., H. Pawlowska, L. Schüller, R. Preusker, J. Fischer, and Y. Fouquart (2000), Radiative Properties of Boundary Layer Clouds: Droplet Effective Radius versus Number Concentration, *J. Atmos. Sci.*, **57**, 803-821.

- Bréon, F.M. D., Tanré, S. Generoso (2002), Aerosol Effect on Cloud Droplet Size Monitored from Satellite, *Science*, **295**, 834-838.
- Carissimo, B.C., A.H. Oort, and T.H. Vonder Haar (1985), Estimating the Meridional Energy Transports in the Atmosphere and Ocean, *J. Phys. Ocean.*, **15**, 82-91, doi: 10.1175/1520-0485.
- Cess, R. D. and Coauthors (1990), Intercomparison and interpretation of climate feedback processes in 19 atmospheric general circulation models, *J. Geophys. Res.*, **95**, 16601-16615.
- Cess R. D., M. Zhang, B. A. Wielicki, D. F. Young, X.-L. Zhou and Y. Nikitenko, (2001), The influence of the 1998 El Niño upon cloud-radiative forcing over the Pacific warm pool, *J. Climate*, **14**, 2129-2137.
- Charlson, R. J., A. S. Ackerman, F. A.-M. Bender, T. L. Anderson, and Z. Liu (2007), On the climate forcing consequences of the albedo continuum between cloudy and clear air, *Tellus*, **59**(4), 715-727.
- Coakley, J.A Jr., P.A. Durkee, K. Nielsen, J.P. Taylor, S. Platnick, B.A. Albrecht, D. Babb, F.-L. Chang, W.R. Tahnk, C.S. Bretherton, and P.V. Hobbs (2000), The Appearance and Disappearance of Ship Tracks on Large Spatial Scales, *J. Atmos. Sci.*, **57**, 2707-2728.
- Coakley J.A. Jr. and C.D. Walsh (2002) Limits to the Aerosol Indirect Radiative Effect Derived from Observations of Ship Tracks, *J. Atmos. Sci.*, **59**, 668-680.
- Collins W. D., F. P. J. Valero, P. J. Flatau, D. Lubin, H. Grassl and P. Pilewskie, (1996), Radiative effects of convection in the tropical Pacific, *J. Geophys. Res.*, **101**, 14999-15012.
- Ferek, R.J., T. Garrett, P.V. Hobbs, S. Strader, D. Johnson, J.P. Taylor, K. Nielsen, A.S. Ackerman, Y. Kogan, Q. Liu, B.A. Albrecht, and D. Babb (2000), Drizzle Suppression in Ship Tracks, *J. Atmos. Sci.*, **57**, 2765-2778.
- Forster, P., V. Ramaswamy, P. Artaxo, T. Berntsen, R. Betts, D.W. Fahey, J. Haywood, J. Lean, D.C. Lowe, G. Myhre, J. Nganga, R. Prinn, G. Raga, M. Schulz and R. Van Dorland, 2007: Changes in Atmospheric Constituents and in Radiative Forcing. In: *Climate Change 2007: The Physical Science Basis. Contribution of Working Group I to the Fourth Assessment Report of the Intergovernmental Panel on Climate Change* [Solomon, S., D. Qin, M. Manning, Z. Chen, M. Marquis, K.B. Averyt, M. Tignor and H.L. Miller (eds.)]. Cambridge University Press, Cambridge, United Kingdom and New York, NY, USA.
- Fowler L. and D. A. Randall, (1994), A global radiative-convective feedback, *Geophys. Res. Lett.*, **21**, 2035-2041.
- Han, Q., W.B. Rossow, J. Zeng, and R. Welch (2002) Three Different Behaviors of

- Liquid Water Path of Water Clouds in Aerosol-Cloud Interactions, **59**, 726-735.
- Harrison E. F., P. Minnis, B. R. Barkstrom, V. Ramanathan, R. D. Cess and G. G. Gibson, (1990), Seasonal variation of cloud radiative forcing derived from the Earth Radiation Budget Experiment, *J. Geophys. Res.*, **95**, 18687-18703
- Hartmann D. L. and M. L. Michaelson, (1993), Large-Scale Effects on the Regulation of Tropical Sea Surface Temperature, *J. Climate*, **6**, 2049-2062.
- Haynes J. M., T. S. L'Ecuyer, G. L. Stephens, S. D. Miller, C. Mitrescu, N. B. Wood, S. Tanelli (2009), Rainfall retrieval over the ocean with spaceborne W-band radar, *J. Geophys. Res.*, **114**, D00A22, doi: 10.1029/2008JD009973.
- Haywood, J. M., V. Ramaswamy, and L. J. Donner (1997), A limited-area model case study of the effects of sub-grid scale variations in relative humidity and cloud upon the direct radiative forcing of sulfate aerosol, *Geophys. Res. Lett.*, **24**, 143-146.
- Held I. M. and B. J. Soden, (2006), Robust Responses of the Hydrological Cycle to Global Warming, *J. Climate*, **19**, 5686-5699.
- Jakob C. and G. Tselioudis, (2003), Objective identification of cloud regimes in the Tropical Western Pacific, *Geophys. Res. Lett.*, **30**, 2082, doi: 10.1029/2003GL018367.
- Jakob C., G. Tselioudis and T. Hume, (2005), The radiative, cloud, and thermodynamic properties of the major tropical western Pacific cloud regimes, *J. Climate*, **18**, 1203-1215.
- Jakob C. and C. Schumacher, (2008), Precipitation and Latent Heating Characteristics of the Major Tropical Western Pacific Cloud Regimes, *J. Climate*, **21**, 4348-4364.
- Jiang H., H. Xue, A. Teller, G. Feingold, Z. Levin (2006), Aerosol effects on the lifetime of shallow cumulus, *Geophys. Res. Lett.*, **33**, L14806, doi: 10.1029/2006GL026024.
- Jiang, H., and G. Feingold, (2006), The effect of aerosol on warm convective clouds: Aerosol-cloud-surface flux feedbacks in a new coupled large eddy model, *J. Geophys. Res.*, **111**, D01202, doi: 10.1029/2005JD006138.
- Kaufman, Y.J., I. Koren, L.A. Remer, D. Rosenfeld, and Y. Rudich (2005), The effect of smoke, dust and pollution aerosol on shallow cloud development over the Atlantic Ocean, *Proceedings of the National Academy of Sciences*, **102**, 11207-11212.
- Kiehl J. T. and V. Ramanathan, (1990) Comparison of cloud forcing derived from the earth radiation budget experiment with that simulated by the NCAR community climate model, *J. of Geophys. Res.*, **95**, 11679-11698.
- Kiehl, J. T., (1994), On the Observed Near Cancellation between Longwave and Shortwave Cloud Forcing in Tropical Regions, *J. Climate*, **7**, 559-565.

- Kiehl J. T. and K. E. Trenberth (1997), Earth's Annual Global Mean Energy Budget, *Bull. Am. Meteor. Soc.*, **78**, 197-208.
- Klein, S.A. and D.L. Hartmann (1993), The Seasonal Cycle of Low Stratiform Clouds, *J. Atmos. Sci.*, **6**, 1587-1606.
- Koren I., Y. J. Kaufman, D. Rosenfeld, L. A. Remer, Y. Rudich (2005), Aerosol invigoration and restructuring of Atlantic convective clouds, *Geophys. Res. Lett.*, **32**, doi: 10.1029/2005GL023187.
- Koren, I., L. A. Remer, Y. J. Kaufman, Y. Rudich, and J. V. Martins (2007), On the twilight zone between clouds and aerosols, *Geophys. Res. Lett.*, **34**, (L08805), doi: 10.1029/2007GL029253.
- Kummerow C., W. Barnes, T. Kozu, J. Shiue and J. Simpson, (1998), The tropical rainfall measuring mission (TRMM) sensor package, *J. Atmos. and Ocean Tech.*, **15**, 808-816.
- Kummerow C. D., Y. Honga, W. S. Olson, S. Yang, R. F. Adler, J. McCollum, R. Ferraro, G. Petty, D.-B. Shin and T. T. Wilheit, (2001), The evolution of the Goddard profiling algorithm (GPROF) for rainfall estimation from passive microwave sensors, *J. Appl. Meteor.*, **40**, 1801-1820.
- L'Ecuyer, T. S. and G. McGarragh, (submitted), A Ten Year Climatology of Tropical Radiative Heating and its Vertical Structure from TRMM Observations, *J. Climate*.
- Lee, M.-I., I.-S. Kang, J.-K. Kim, and B. Mapes (2001), Influence of cloud-radiation interaction on simulating tropical intraseasonal oscillation with an atmospheric general circulation model, *J. Geophys. Res.*, **106**(D13), 14219-14233.
- Lin J. and B. E. Mapes, (2004), Radiation Budget of the Tropical Intraseasonal Oscillation, *J. Atmos. Sci.*, **61**, 2050-2062.
- Liou, K. N., *An Introduction to Atmospheric Radiation*, 583 pp., Academic Press, New York, 2002.
- Long, A. B. (1974), Solutions to the Droplet Collection Equation for Polynomial Kernels *J. Atmos. Sci.* **31**, 1040-1052, doi: 10.1175/1520-0469.
- Madden R. A. and P. R. Julian, (1971), Detection of a 40-50 day oscillation in the zonal wind in the tropical Pacific, *J. Atmos. Sci.*, **28**, 702-708.
- Madden R. A. and P. R. Julian, (1972), Description of global scale circulation cells in the tropics with a 50 day period, *J. Atmos. Sci.*, **29**, 1109-1123.
- Manabe S. and R. T. Wetherald, (1967), Thermal equilibrium of the atmosphere with a given distribution of relative humidity, *J. Atmos. Sci.*, **24**, 241-259.

- Martin, G.M., D.W. Johnson, and A. Spice (1994), The Measurement and Parameterization of Effective Radius of Droplets in Warm Stratocumulus Clouds, *J. Atmos. Sci.*, **51**, 1823-1842.
- Matsui T., H. Masunaga, R.A. Pielke Sr., W.-K. Tao (2004), Impact of aerosols and atmospheric thermodynamics on cloud properties within the climate system, *Geophys. Res. Lett.*, **31**, L06109, doi: 10.1029/2003GL019287.
- Matsui T., H. Masunaga, S.M. Kreidenweis, R.A. Pielke Sr., W.-K. Tao, M. Chin, Y.J. Kaufman (2006), Satellite-based assessment of marine low cloud variability associated with aerosol, atmospheric stability, and the diurnal cycle, *J. Geophys. Res.*, **111**, D17204, doi: 10.1029/2005JD006097.
- Nakajima, T., A. Higurashi, K. Kawamoto, J.E. Penner (2001), A possible correlation between satellite-derived cloud and aerosol microphysical parameters, *Geophys. Res. Lett.*, **28** (7), 1171-1174, doi: 10.1029/2000GL012186.
- Pawlowska H., J.-L. Brenguier (2003), An observational study of drizzle formation in stratocumulus clouds for general circulation model (GCM) parameterizations, *J. Geophys. Res.*, **108** (D15), 8630, doi: 10.1029/2002JD002679.
- Pierrehumbert, R., (1995), Thermostats, radiator fins, and the runaway greenhouse, *J. Atmos. Sci.*, **52**, 1784-1806.
- Pincus, R and M. Baker (1994) Effect of precipitation on the albedo susceptibility of clouds in the marine boundary layer, *Nature*, **372**, 250-252.
- Platnick S., M. D. King, S. A. Ackerman, W. P. Menzel, B. A. Baum, J. C. Riédi and R. A. Frey, (2003), The MODIS cloud products: Algorithms and examples from Terra, *IEEE Trans. Geosci. Remote Sens.*, **41**, 459-473.
- Pruppacher, H. R., and J. D. Klett, *Microphysics of Clouds and Precipitation*, 954 pp., Kluwer Acad., Norwell, Mass., 1997.
- Quaas, J., O. Boucher, N. Bellouin, and S. Kinne (2008), Satellite-based estimate of the direct and indirect aerosol climate forcing, *J. Geophys. Res.*, **113**, D05204, doi: 10.1029/2007JD008962.
- Ramanathan V. and W. D. Collins, (1991), Thermodynamic regulation of the ocean warming by cirrus clouds deduced from observations of the 1987 El Niño, *Nature*, **351**, 27-32.
- Raymond, D. J. (2001), A New Model of the Madden-Julian Oscillation, *J. Atmos. Sci.*, **58**, 2807-2819.
- Remer, L.A., Y.J. Kaufman, D. Tanré, S. Mattoo, D.A. Chu, J.V. Martins, R.-R. Li, C. Ichoku, R.C. Levy, R.G. Kleidman, T.F. Eck, E. Vermote, and B.N. Holben (2005,) The MODIS Aerosol Algorithm, Products, and Validation *J. Atmos. Sci.*,

62, 947-973.

- Rosenfeld, D. (2000), Suppression of Rain and Snow by Urban and Industrial Air Pollution, *Science*, **287**, 1793-1796.
- Ramanathan V., R. D. Cess, E. F. Harrison, P. Minnis, B. R. Barkstrom, E. Ahmad, and D. Hartmann (1989), Cloud-radiative forcing and climate: Results from the Earth Radiation Budget Experiment. *Science*, **243**, 57-63.
- Rossow W. B., and Y.-C. Zhang (1995), Calculation of surface and top of the atmosphere radiative fluxes from physical quantities based on ISCCP data sets. 2. Validation and first results, *J. Geophys. Res.*, **100**, 1167-1197.
- Rossow W. B., G. Tselioudis, A. Polak and C. Jakob, (2005), Tropical climate described as a distribution of weather states indicated by distinct mesoscale cloud property mixtures, *Geophys. Res. Lett.*, **32**, L21812, doi: 10.1029/2005GL024584.
- Schiffer R. A. and W. B. Rossow, (1983), The International Satellite Cloud Climatology Project (ISCCP): The first project of the World Climate Research Programme, *Bull. Amer. Meteor. Soc.*, **64**, 779-784.
- Schneider, S. H. (1972), Cloudiness as a Global Climatic Feedback Mechanism: The Effects on the Radiation Balance and Surface Temperature of Variations in Cloudiness, *J. Atmos. Sci.*, **29**, 1413-1422.
- Sekiguchi M., T. Nakajima, K. Suzuki, K. Kawamoto, A. Higurashi, D. Rosenfeld, I. Sano, S. Mukai (2003), A study of the direct and indirect effects of aerosols using global satellite data sets of aerosol and cloud parameters, *J. Geophys. Res.*, **108** (D22), 4699, doi:10.1029/2002JD003359.
- Sobel, A. H., and H. Gildor (2003), A Simple Time-Dependent Model of SST Hot Spots, *J. Climate*, **16**, 3978-3992, doi: 10.1175/1520-0442.
- Soden B. J. and I. M. Held (2006), An Assessment of Climate Feedbacks in Coupled OceanAtmosphere Models *J. Climate*, **19**, 3354-3360. doi: 10.1175/JCLI3799.1.
- Stephens, G.L. (1978) Radiation Profiles in Extended Water Clouds. II: Parameterization Schemes, *J. Atmos. Sci.*, **35**, 2123-2132.
- Stephens G. L. and P. J. Webster, (1981), Clouds and Climate: Sensitivity of Simple Systems, *J. Atmos. Sci.*, **38**, 235-247.
- Stephens, G.L., P.M. Gabriel, and P.T. Partain (2001) Parameterization of Atmospheric Radiative Transfer. Part I: Validity of Simple Models, *J. Atmos. Sci.*, **58**, 3391-3409.
- Stephens, G.L., D.J. Vane, R.J. Boain, G.G. Mace, K. Sassen, Z. Wang, A.J. Illingworth, E.J. O'Connor, W.B. Rossow, S.L. Durden, S.D. Miller, R.T. Austin, A.

- Benedetti, C. Mitrescu, and The CloudSat Science Team (2002), THE CLOUDSAT MISSION AND THE A-TRAIN, *Bull. Amer. Meteor. Soc.*, **83**, 1771-1790.
- Stephens G. L., P. J. Webster, R. H. Johnson, R. Engelen and T. L'Ecuyer, (2004), Observational Evidence for the Mutual Regulation of the Tropical Hydrological Cycle and Tropical Sea Surface Temperatures, *J. Climate*, **17**, 2213-2224.
- Stephens, G. L. (2005), Cloud Feedbacks in the Climate System: A Critical Review, *J. Climate*, **18**, 237-273, doi: 10.1175/JCLI-3243.1.
- Stephens G.L., J.M. Haynes (2007), Near global observations of the warm rain coalescence process, *Geophys. Res. Lett.*, **34**, L20805, doi:10.1029/2007GL030259.
- Stephens G.L., C. Kummerow (2007), The Remote Sensing of Clouds and Precipitation from Space: A Review, *J. Atmos. Sci.*, **64**, 3742-3765.
- Stephens G. L., S. C. van den Heever and L. Pakula, (2008), Radiative-Convective Feedbacks in Idealized States of Radiative-Convective Equilibrium, *J. Atmos. Sci.*, **65**, 3899-3916, doi: 10.1175/2008JAS2524.1.
- Stephens G. L. and T. D. Ellis, (2008), Controls of Global-Mean Precipitation Increases in Global Warming GCM Experiments, *J. Climate*, **21**, 6141-6155, doi: 10.1175/2008JCLI2144.1.
- Susskind J., C. D. Barnet and J. M. Blaisdell, (2003), Retrieval of atmospheric and surface parameters from AIRS/AMSU/HSB data in the presence of clouds, *IEEE Trans. Remote Sens.*, **41**, 390-409.
- Taylor, J.P., M.D. Glew, J.A. Coakley Jr., W.R. Tahnk, S. Platnick, P.V. Hobbs, and R.J. Ferek (2000), Effects of Aerosols on the Radiative Properties of Clouds, *J. Atmos. Sci.*, **57**, 2656-2670.
- Trenberth, K. E., J. T. Fasullo and J. Kiehl (2009), Earth's global energy budget, *Bull. Am. Meteor. Soc.*, doi: 10.1175/2008BAMS2634.1.
- Twomey, S. (1977), The Influence of Pollution on the Shortwave Albedo of Clouds, *J. Atmos. Sci.*, **34**, 1149-1152.
- vanZanten, M.C., B. Stevens, G. Vali, and D.H. Lenschow (2005), Observations of Drizzle in Nocturnal Marine Stratocumulus, *J. Atmos. Sci.*, **62**, 88-106.
- Vonder Haar T.H. and V. E. Suomi, (1969), Satellite observations of the earth's radiation budget, *Science*, **163**, 667-669.
- Vonder Haar, T. H and Verner E. Suomi (1971), Measurements of the Earth's Radiation Budget from Satellites During a Five-Year Period. Part I: Extended Time and Space Means, *J. Atmos. Sci.*, **28**, 305-314, doi: 10.1175/1520-0469.
- Wallace, J. M., (1992), Effect of deep convection on the regulation of tropical SST,

Nature, **377**, 230-231.

Wang, S., Wang, Q., and Feingold G. (2003), Turbulence, Condensation, and Liquid Water Transport in Numerically Simulated Nonprecipitating Stratocumulus Clouds *J. Atmos. Sci.*, **60**, 262-278.

Weickmann K. M., G. R. Lussky and J. E. Kutzbach, (1985), Intraseasonal (30-60 day) fluctuations of outgoing longwave radiation and 250 mb streamfunction during northern winter, *Mon. Wea. Rev.*, **113**, 941-961.

Wen, G., A., Marshak, R. F. Cahalan, L. A. Remer, and R. G. Kleidman (2007), 3-D aerosol-cloud radiative interaction observed in collocated MODIS and ASTER images of cumulus cloud fields, *J. Geophys. Res.*, **112**, (D13204), doi: 10.1029/2006JD008267.

Wentz, F.J., and R.W. Spencer (1998), SSM/I Rain Retrievals within a Unified All-Weather Ocean Algorithm, *J. Atmos. Sci.*, **55**, 1613-1627.

Wheeler M. C. and H. H. Hendon, (2004), An All-Season Real-Time Multivariate MJO Index: Development of an Index for Monitoring and Prediction, *Mon. Wea. Rev.*, **132**, 1917-1932.

Wielicki B. A., B. R. Barkstrom, E. F. Harrison, R. B. Lee III, G. L. Smith and J. E. Cooper, (1996), Clouds and the Earth's Radiant Energy System (CERES): An earth observing system experiment, *Bull. Amer. Meteor. Soc.*, **77**, 853-868.

Wolter, K., and M.S. Timlin, 1993: Monitoring ENSO in COADS with a seasonally adjusted principal component index. *Proc. of the 17th Climate Diagnostics Workshop*, Norman, OK, NOAA/NMC/CAC, NSSL, Oklahoma Clim. Survey, CIMMS and the School of Meteor., Univ. of Oklahoma, 52-57.

Wood, R., and C. S. Bretherton (2006), On the relationship between stratiform low cloud cover and lower tropospheric stability, *J. Clim.* **19**, 6425-6432.

Wood, R. (2007), Cancellation of Aerosol Indirect Effects in Marine Stratocumulus through Cloud Thinning, *J. Atmos. Sci.*, **64**, 2657-2669.

Wyant M. C., C. S. Bretherton, J. T. Bacmeister, J. T. Kiehl, I. M. Held, M. Zhao, S. A. Klein, and B. J. Soden (2006), A comparison of low-latitude cloud properties and their response to climate change in three AGCMs sorted into regimes using mid-tropospheric vertical velocity, *clim. dynam.*, **27**, 261-279, doi: 10.1007/s00382-006-0138-4.

Xue, H. and G. Feingold (2006), Large-Eddy Simulations of Trade Wind Cumuli: Investigation of Aerosol Indirect Effects, *J. Atmos. Sci.*, **63**, 1605-1622.

Zhang Y.-C., W. B. Rossow, and A. A. Lacis (1995), Calculation of surface and top of the atmosphere radiative fluxes from physical quantities based on ISCCP data sets. 1. Method and sensitivity to input data uncertainties. *J. Geophys. Res.*,

100, 1149-1165.

Zhang, C., (2005), Madden-Julian Oscillation, *Rev. of Geophysics*, **43**, RG2003, doi:
10.1029/2004RG000158.